

# A Measurement of the Proton Spin Structure Function $g_2^p$ at Low $Q^2$

by

Min Huang

Department of Physics  
Duke University

Date: \_\_\_\_\_

Approved:

\_\_\_\_\_  
Haiyan Gao, Supervisor

\_\_\_\_\_  
Steffen A. Bass

\_\_\_\_\_  
Calvin R. Howell

\_\_\_\_\_  
Stephen W. Teitsworth

\_\_\_\_\_  
Christopher W. Walter

Dissertation submitted in partial fulfillment of the requirements for the degree of  
Doctor of Philosophy in the Department of Physics  
in the Graduate School of Duke University  
2016

# ABSTRACT

A Measurement of the Proton Spin Structure Function  $g_2^p$  at  
Low  $Q^2$

by

Min Huang

Department of Physics  
Duke University

Date: \_\_\_\_\_

Approved:

\_\_\_\_\_  
Haiyan Gao, Supervisor

\_\_\_\_\_  
Steffen A. Bass

\_\_\_\_\_  
Calvin R. Howell

\_\_\_\_\_  
Stephen W. Teitsworth

\_\_\_\_\_  
Christopher W. Walter

An abstract of a dissertation submitted in partial fulfillment of the requirements for  
the degree of Doctor of Philosophy in the Department of Physics  
in the Graduate School of Duke University  
2016

Copyright © 2016 by Min Huang  
All rights reserved except the rights granted by the  
Creative Commons Attribution-Noncommercial Licence

# Abstract

Experiments at Jefferson Lab have been conducted to extract the nucleon spin-dependent structure functions over a wide kinematic range. Higher moments of these quantities provide tests of QCD sum rules and predictions of chiral perturbation theory ( $\chi$ PT). While precise measurements of  $g_1^n$ ,  $g_2^n$ , and  $g_1^p$  have been extensively performed, the data of  $g_2^p$  remain scarce. Discrepancies were found between existing data related to  $g_2$  and theoretical predictions. Results on the proton at large  $Q^2$  show a significant deviation from the Burkhardt-Cottingham sum rule, while results for the neutron generally follow this sum rule. The next-to-leading order  $\chi$ PT calculations exhibit discrepancy with data on the longitudinal-transverse polarizability  $\delta_{LT}^n$ . Further measurements of the proton spin structure function  $g_2^p$  are desired to understand these discrepancies.

Experiment E08-027 (g2p) was conducted at Jefferson Lab in experimental Hall A in 2012. Inclusive measurements were performed with polarized electron beam and a polarized ammonia target to obtain the proton spin-dependent structure function  $g_2^p$  at low  $Q^2$  region ( $0.02 < Q^2 < 0.2 \text{ GeV}^2$ ) for the first time. The results can be used to test the Burkhardt-Cottingham sum rule, and also allow us to extract the longitudinal-transverse spin polarizability of the proton, which will provide a benchmark test of  $\chi$ PT calculations. This thesis presents and discusses the very preliminary results of the transverse asymmetry and the spin-dependent structure functions  $g_1^p$  and  $g_2^p$  from the data analysis of the g2p experiment.

# Contents

<b>Abstract</b>	<b>iv</b>
<b>List of Tables</b>	<b>x</b>
<b>List of Figures</b>	<b>xi</b>
<b>List of Abbreviations and Symbols</b>	<b>xv</b>
<b>Acknowledgements</b>	<b>xvii</b>
<b>1 Introduction and Physics Motivation</b>	<b>1</b>
1.1 Electron scattering . . . . .	3
1.1.1 Kinematic Variables . . . . .	4
1.1.2 Elastic Scattering . . . . .	4
1.1.3 Inelastic Scattering . . . . .	6
1.2 Differential Cross Section Formalism . . . . .	8
1.3 Polarized Structure Functions . . . . .	10
1.4 Structure Functions in the Quark-Parton Model . . . . .	11
1.5 Operator Product Expansion . . . . .	13
1.6 Chiral Perturbation Theory . . . . .	14
<b>2 Structure Function <math>g_2</math></b>	<b>16</b>
2.1 Spin-dependent Structure Function $g_2$ . . . . .	16
2.2 Sum Rule and Moments . . . . .	18
2.2.1 Virtual Photoabsorption Cross Sections . . . . .	18

2.2.2	Generalized Forward Spin polarizability $\gamma_0$ and Longitudinal-Transverse Polarizability $\delta_{LT}$ . . . . .	20
2.2.3	The Burkhardt-Cottingham Sum Rule . . . . .	21
2.3	Existing Measurements . . . . .	22
2.3.1	$g_2$ . . . . .	22
2.3.2	BC Sum Rule . . . . .	24
2.3.3	Spin polarizabilities $\gamma_0$ and $\delta_{LT}$ . . . . .	28
<b>3</b>	<b>The Experiment</b>	<b>30</b>
3.1	Overview . . . . .	30
3.2	Author Contributions . . . . .	31
3.3	The Electron Accelerator . . . . .	32
3.3.1	Beam Energy . . . . .	33
3.4	Hall A Beamline . . . . .	34
3.4.1	Beam Current Monitors . . . . .	35
3.4.2	Beam Position Monitors and Rasters . . . . .	37
3.4.3	Beam Helicity . . . . .	37
3.4.4	Beam Polarization . . . . .	38
3.4.5	Chicane Magnets . . . . .	39
3.4.6	Local Beam Dump . . . . .	40
3.5	The Polarized $\text{NH}_3$ Target . . . . .	40
3.6	Hall A Spectrometer . . . . .	44
3.7	Septum Magnets . . . . .	46
3.8	Detector Package . . . . .	48
3.8.1	Vertical Drift Chamber . . . . .	49
3.8.2	Scintillators and Trigger Electronics . . . . .	50
3.8.3	Cherenkov Detectors . . . . .	52

3.8.4	Lead Glass Calorimeter . . . . .	53
3.9	Data Acquisition System . . . . .	54
<b>4</b>	<b>Optics and Simulation</b>	<b>56</b>
4.1	Overview . . . . .	56
4.2	Coordinate Systems . . . . .	57
4.3	Experimental Setup and Techniques . . . . .	60
4.3.1	Introduction . . . . .	60
4.3.2	Data Acquired . . . . .	61
4.4	Optics without Target Field . . . . .	65
4.4.1	Calibration Procedure . . . . .	66
4.4.2	Results and Performances . . . . .	68
4.5	Optics with Target Field . . . . .	69
4.5.1	Calibration Approach . . . . .	69
4.5.2	Calibration Results . . . . .	71
4.6	Central Scattering Angle Measurements . . . . .	71
4.6.1	Survey . . . . .	71
4.6.2	Pointing Measurement . . . . .	73
4.6.3	Conclusion . . . . .	76
4.7	Simulation . . . . .	77
4.7.1	Snake Simulation . . . . .	77
4.7.2	g2p Simulation . . . . .	80
<b>5</b>	<b>Data Analysis</b>	<b>81</b>
5.1	Physics Analysis Overview . . . . .	81
5.2	Detector Calibrations and Efficiencies . . . . .	82
5.2.1	VDC Multi-track Efficiency . . . . .	82

5.2.2	Trigger Efficiency . . . . .	83
5.2.3	PID Efficiency . . . . .	85
5.3	False Asymmetry . . . . .	86
5.4	Dilution Factor . . . . .	87
5.4.1	Packing Fraction . . . . .	92
5.5	Acceptance Cuts . . . . .	93
<b>6</b>	<b>Results</b>	<b>96</b>
6.1	Asymmetry Measurements . . . . .	96
6.2	Statistical Uncertainty . . . . .	98
6.3	Model Predictions . . . . .	100
6.3.1	MAID . . . . .	100
6.3.2	Peter Bosted Model . . . . .	101
6.4	Radiative Correction . . . . .	102
6.5	Systematic Uncertainty . . . . .	105
6.6	Results for $g_2^p$ . . . . .	107
6.7	Discussion . . . . .	108
6.8	Summary and Outlook . . . . .	111
<b>A</b>	<b>Statistical Uncertainty of Prescaled Events</b>	<b>113</b>
<b>B</b>	<b>Experimental Records</b>	<b>115</b>
B.1	Sieve Slit . . . . .	115
B.2	Survey Report . . . . .	115
<b>C</b>	<b>Summary of non-thesis work</b>	<b>119</b>
C.1	Introduction . . . . .	119
C.2	Theoretical Background . . . . .	121
C.3	Motivation . . . . .	125



C.4	SIDIS at EIC . . . . .	127
C.4.1	Phase Space Coverage . . . . .	127
C.4.2	Transverse SSA measurements from SIDIS at EIC . . . . .	130
C.5	Conclusion . . . . .	134
	<b>Bibliography</b>	<b>135</b>
	<b>Biography</b>	<b>142</b>

# List of Tables

3.1	Summary of the Møller measurements for g2p experiment . . . . .	39
3.2	HRS characteristics. . . . .	46
3.3	Production data corresponding to different septa configurations. . . .	48
4.1	Optics Performance without Target Field. . . . .	69
4.2	Uncertainties of survey measurements and target position determination	71
4.3	Survey results of central scattering angle . . . . .	73
5.1	Parameters used in dilution calculation [79]. . . . .	92
6.1	Systematic uncertainties. . . . .	107
C.1	Integrated luminosities, and the effective polarizations. . . . .	131

# List of Figures

1.1	Electron scattering through one-photon exchange . . . . .	3
2.1	Virtual photon-nucleon scattering . . . . .	20
2.2	SLAC E143, E155, E155x g2 results . . . . .	23
2.3	JLab E97-103 g2 results . . . . .	24
2.4	E97-103 g2 results . . . . .	25
2.5	RSS g2 results . . . . .	26
2.6	BC sum rule results . . . . .	27
2.7	Generalized spin polarizabilities results . . . . .	28
3.1	g2p Kinematics . . . . .	33
3.2	JLab Accelerator and Halls . . . . .	34
3.3	Arc Energy Measurement . . . . .	35
3.4	Picture of Hall A. . . . .	36
3.5	g2p Beamline . . . . .	36
3.6	Rastered Beam . . . . .	38
3.7	Chicane dipole magnets. . . . .	40
3.8	The local beam dump. . . . .	41
3.9	NH <sub>3</sub> Target . . . . .	42
3.10	Target DNP Spin Flip Transitions . . . . .	43
3.11	Target Polarization . . . . .	44
3.12	HRS layout . . . . .	45

3.13	Schematic of how septum magnet deflects electrons into HRS. . . . .	46
3.14	Septum Magnets . . . . .	47
3.15	HRS detector packages. . . . .	49
3.16	VDCs. . . . .	50
3.17	Scintillators. . . . .	51
3.18	Trigger Design. . . . .	52
3.19	Lead glass calorimeter. . . . .	54
3.20	Hall A DAQ system. . . . .	55
4.1	Hall Coordinate System . . . . .	57
4.2	Target Coordinate System . . . . .	58
4.3	Detector Coordinate System . . . . .	59
4.4	Transport Coordinate System . . . . .	60
4.5	Focal Plane Coordinate System . . . . .	61
4.6	Hall A Optics Setup . . . . .	62
4.7	Optics Data Taken with Sieve . . . . .	62
4.8	Sieve slit design. . . . .	63
4.9	Optics beam scan. . . . .	64
4.10	Optics reconstruction results for angles. . . . .	68
4.11	Optics reconstruction results for momentum. . . . .	69
4.12	Optics with Target Field . . . . .	70
4.13	Reconstruct the scattering Angle . . . . .	70
4.14	Optics Calibration of Angles . . . . .	72
4.15	Optics momentum reconstruction results for 1.7 GeV, 2.5 T configuration. . . . .	73
4.16	Double elastic peaks from carbon and helium. . . . .	75
4.17	Schematic of the pointing measurement. . . . .	76

4.18	Uncertainty of $\theta - \theta_0$ (left) and $\theta/\theta_0$ (right) from MC simulation . . .	76
4.19	Central angle measurement results. . . . .	77
4.20	First online optics run result. . . . .	79
5.1	VDC Efficiency. . . . .	83
5.2	Trigger Efficiency. . . . .	84
5.3	Cherenkov Efficiency. . . . .	86
5.4	pion rejector Efficiency. . . . .	87
5.5	Pion Suppression. . . . .	88
5.6	False Asymmetries. . . . .	89
5.7	Target Stick . . . . .	90
5.8	Illustration of Target Nose . . . . .	91
5.9	Acceptance Cuts . . . . .	95
6.1	Physics Asymmetries. . . . .	100
6.2	Comparisons of MAID model with data. . . . .	101
6.3	NLO radiative corrections. . . . .	104
6.4	Radiative correction schematics. . . . .	105
6.5	Radiated models. . . . .	106
6.6	Radiative corrected asymmetries. . . . .	106
6.7	Asymmetry results. . . . .	108
6.8	Unpolarized cross section from the Bosted model. . . . .	109
6.9	Transverse cross section difference. . . . .	109
6.10	Longitudinal cross section difference. . . . .	110
6.11	g2 results. . . . .	110
B.1	Sieve slit design report. . . . .	116
B.2	Survey report A1423. . . . .	117

B.3	Survey report A1453. . . . .	118
C.1	Schematic of the EIC at JLab . . . . .	120
C.2	Kinematic variables of the DIS. . . . .	121
C.3	Leading Twist TMDs: . . . . .	123
C.4	Definitions of azimuthal angles $\phi_h$ and $\phi_S$ , and the hadron transverse momentum for SIDIS in the ion-at-rest frame. . . . .	125
C.5	Momentum vs. polar angle. . . . .	127
C.6	SIDIS phase space . . . . .	129
C.7	Momenta vs. $P_T$ and polar angles vs. $P_T$ at $P_T > 1$ GeV/c. . . . .	130
C.8	Projections with proton on $\pi^+$ . . . . .	132
C.9	Projections with proton on $\pi^+$ to show the $P_T$ dependence. . . . .	133

# List of Abbreviations and Symbols

## Symbols

$\vec{k}$	3-vector of $k$ .
$\mathcal{O}$	Math mode of $O$ .
$\mathcal{P}$	Math mode of $P$ .
$\alpha$	E&M interaction coupling constant.
$\alpha_S$	Strong interaction coupling constant.

## Abbreviations

A/D	Analog to digital.
ADC	Analog to digital converter.
BCM	Beam current monitor.
BPM	Beam position monitor.
CEBAF	Continuous electron beam accelerator facility.
DAQ	Data acquisition.
DIS	Deep inelastic scattering.
EPICS	Experimental physics and industrial control system.
FWHM	Full width half maximum.
HRS	High resolution spectrometer.
JLab	Jefferson Lab.
NMR	Nuclear magnetic resonance.

OPE	Operator Product Expansion.
PID	Particle identification.
PMT	Photo-multiplier tube.
QCD	Quantum chromodynamics.
RMS	Root mean square.
TDC	Time to digital converter.
VDC	Vertical drift chamber.
ppm	Part per million.



# Acknowledgements

It has been a long journey being a graduate student at Duke and pursuing the PhD degree. At this moment, I would like to express my sincere appreciation to a lot of people who helped me in these years.

First and foremost, my deepest gratitude goes to my advisor Haiyan Gao for her support and guidance. I appreciate and admire her efforts to communicate with students closely. And after the initial guidance, she always let me independently think and conduct the research work, and of course gave advice when needed. This helped me grow with critical thinking and problem solving abilities, which would always benefit me. I'm also thankful for her help in correcting the draft of this thesis.

I'd like to thank my supervisor Jian-ping Chen at Jefferson Lab. In the third year, I moved to Jefferson Lab and joined the E08-027 collaboration. As one of the spokespeople of E08-027 experiment, he has supervised the research work closely. His knowledge and enthusiasm on nuclear physics are amazing. His rigorous attitude towards the analysis results has been an excellent training to me.

E08-027 collaboration has been a great group to work with. I'd like to thank the spokespeople Alexandre Camsonne, Jian-ping Chen, Don Crabb, and Karl Slifer for their scientific vision and efforts to realize this experiment. I learned a lot from their professional examples. I am grateful to John Leroose for introducing to me the field of spectrometer optics, and guiding me through the preparation of the experiment.

Thanks to Nilanga Liyanage, Jin Huang, Yi Qiang, Kiad Saenboonruang, Huan Yao, and Zhihong Ye for helping me when I started on the analysis. I'd like to thank Jixie Zhang, Chao Gu, and Jie Liu, whom I worked with on the preparation of the experiment and the analysis on a daily basis. They inspired and helped me through countless discussions and conversations. I'd also like to thank all other post-docs and students Kalyan Allada, James Maxwell, Vince Sulkosky, Toby Badman, Melissa Cummings, Pengjia Zhu, Ryan Zielinski. This experiment could not have succeeded without their intense efforts.

I am lucky to be a member of the medium energy group at Duke. When I first entered this field, Xin Qian guided and worked with me on the first project. I am grateful to his help of introducing the physics and analysis skills to me, and answering my questions patiently. I learned a lot from him. I want to thank Zhiwen Zhao for reading my thesis draft and offered valuable comments. I want to acknowledge all the current and past members of the MEP group who had helped and inspired me. I also want to thank all my friends at Duke and Jefferson Lab for the joyous time we shared.

Last but not least, I'd like to thank my parents, whose unconditional love and constant support could never be matched with any word. I also want to thank my husband Yang Zhang for being my best friend and love of my life, and for letting me become a better me.

## Introduction and Physics Motivation

The journey of spin physics began with the Stern-Gerlach experiment in 1922, which showed evidence of quantized angular momentum of the atomic beam. Later, Uhlenbeck and Goudsmit introduced the concept of *spin*, and explained the results of the experiment. Spin was interpreted by Uhlenbeck and Goudsmit as an intrinsic property of the electron. It appears like an angular momentum, but does not relate to the spatial motion of the particle.

From Dirac equation, the magnetic moment of a structureless spin-1/2 particle was predicted as  $\mu = -\frac{e}{2m}$ , where  $e$  is the charge and  $m$  is the mass. This agreed with the experimental result for electron. In 1933, Stern and his group performed measurements of proton magnetic moment, and discovered an considerably larger magnetic moment of the proton comparing with Dirac's prediction [1]. Furthermore, neutron is electronically neutral, and the magnetic moment was expected to be zero, but was found to be nonzero from measurement of deuteron. This deviation in the magnetic moment from the prediction of Dirac equation is called the anomalous magnetic moment. This evidence first indicated that the nucleons were not point-like, and instead had internal structures.

Starting from mid-1950s, electron scattering was used to study the spatial charge and current distribution of the nucleon and the experimental results confirmed that the nucleons indeed have composite structures. Many theories were proposed to describe the nucleon structure. Feynman proposed the parton model in late 1960s [2], and was confirmed by an extensive study using deep inelastic scattering at SLAC [3]. The parton model and measurements revealed the underlying degrees of freedom for the nucleon, which are now associated with quarks and gluons. Quantum chromodynamics (QCD) emerged as a theory to describe the interaction of quarks by exchange of gluons. In the high energy region, predictions from perturbative QCD have been proven to well describe the experimental results. However, in the low energy region, QCD calculations become difficult due to the large coupling constant  $\alpha_S$ . Therefore, low energy effective field theories such as the chiral perturbation theory ( $\chi$ PT) have been utilized to perform calculations.

In the 1980's, the spin degree of freedom of the nucleon was investigated at CERN [4] and SLAC [5]. The experiments aimed to study how the total spin of the nucleon was shared among the constituents and were performed with polarized beams and polarized targets. The results showed that the net spin carried by quarks was very small. This is known as the “spin crisis”. A number of experimental and theoretical activities have been performed on this topic in the following twenty years at CERN, DESY and Jefferson Lab using lepton beams. The current understanding of the nucleon spin [6] is that the net spin is the sum of intrinsic spin and orbital angular momenta of quarks, and total angular momentum of gluons. These studies show that only about 30% of the nucleon's spin is contributed by the spin of the quarks.

The spin contributions can be calculated as the integrals of spin-dependent distribution functions. These distribution functions shed light on how quarks and gluons constitute the nucleon spin and the underlying dynamic mechanism. Continuous

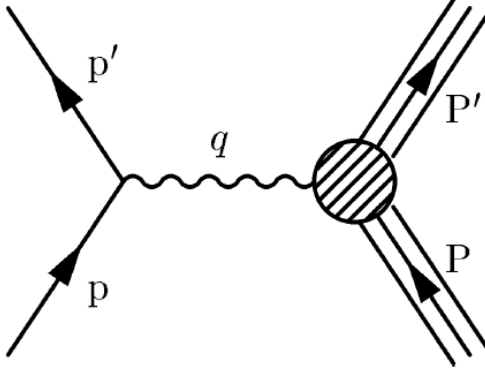


FIGURE 1.1: Diagram of electron scattering through one-photon exchange.

experimental efforts have been made to understand the spin structure of the nucleon. Measurements at Jefferson Lab have been specifically performed at low and intermediate momentum transfer regions to study the non-perturbative regime. Experiment E08-027 (g2p) follows the path of these experiments by measuring precise spin-dependent quantities at low energies to study the quark-gluon interaction, and provide tests of predictions by effective field theory ( $\chi$ PT) in the non-perturbative region.

## 1.1 Electron scattering

Inclusive electron scattering off a nucleon has been used as a powerful tool to explore the nucleon structure. The one-photon exchange Born approximation for electron scattering is shown in Fig. 1.1. In this picture, an electron with four momentum  $p^\mu = (E, \vec{p})$  scatters off a target nucleus (or nucleon) with four momentum  $P^\mu = (E_t, \vec{P})$  via the exchange of a virtual photon with four momentum  $q^\mu = (\nu, \vec{q})$ . For the inclusive measurement, only the scattered electron with four momentum  $p'^\mu = (E', \vec{p}')$  is detected. The final hadronic system is denoted with four momentum  $P'^\mu = (E'_t, \vec{P}')$ .

### 1.1.1 Kinematic Variables

In this process, an energy  $\nu = \frac{P \cdot q}{M}$  and momentum  $\vec{q} = \vec{p} - \vec{p}'$  are transferred to the target. The invariant mass of the undetected residual hadronic system is  $W = \sqrt{(P + q)^2}$ . We also introduce two dimensionless and Lorentz invariant variables  $x = \frac{Q^2}{2P \cdot q}$ , and  $y = \frac{P \cdot q}{P \cdot p}$ .

In the laboratory system, where  $P^\mu = (M, 0)$ , we find the kinematic relations:

$$\nu = E - E' \quad (1.1)$$

$$Q^2 = -q^2 = 4EE' \sin^2 \frac{\theta}{2} \quad (1.2)$$

$$W^2 = M^2 + 2M\nu - Q^2 \quad (1.3)$$

$$x = \frac{Q^2}{2M\nu} \quad (1.4)$$

$$y = \frac{\nu}{E}, \quad (1.5)$$

where we denote the electron scattering angle by  $\theta$ , and neglect the electron mass under relativistic circumstance.

The cross section for electron scattering is a function of  $Q^2$  and  $\nu$ . With increasing  $Q^2$  and  $\nu$ , the electron scattering off a light nucleus includes different types of interaction: elastic, quasi-elastic, resonance and deep inelastic regions. In the situation of electron scattered off a nucleon, no quasi-elastic is present. In the following sections, this situation will be discussed since the g2p experiment aims at exploring the proton structure.

### 1.1.2 Elastic Scattering

The nucleon stays intact in the elastic scattering. In the elastic scattering, the invariant mass  $W$  is equal to the mass of the nucleon. Since the nucleon is a particle with

charge distribution instead of a point particle. The cross section can be expressed as:

$$\frac{d\sigma}{d\Omega} = \left( \frac{d\sigma}{d\Omega} \right)_{Mott} |F(q)|^2, \quad (1.6)$$

where  $q$  is the momentum transfer from the incident electron to the target. The Mott cross section  $\left( \frac{d\sigma}{d\Omega} \right)_{Mott}$  is the cross section of electron scattered off a point particle:

$$\left( \frac{d\sigma}{d\Omega} \right)_{Mott} = \frac{\alpha^2 \cos^2 \frac{\theta}{2}}{4E^2 \sin^4 \frac{\theta}{2}}. \quad (1.7)$$

The proton magnetic moment also interacts with the electron current. In addition, the proton will recoil in the electron scattering. If the proton is still considered as a structureless particle with charge  $e$  and Dirac magnetic moment  $e/2M$ , the Mott cross section becomes:

$$\left( \frac{d\sigma}{d\Omega} \right)_{point} = \frac{\alpha^2}{4E^2 \sin^4 \frac{\theta}{2}} \frac{E'}{E} \left( \cos^2 \frac{\theta}{2} + \frac{Q^2}{2M^2} \sin^2 \frac{\theta}{2} \right). \quad (1.8)$$

The magnetic part contributes more when  $Q^2$  or the scattering angle becomes larger. This makes the cross section drop less strongly than the Mott cross section as a function of  $Q^2$ .

In the case of elastic scattering, the energy and scattering angle of the electron follows this relation:

$$\frac{E'}{E} = \frac{1}{1 + \frac{2E}{M} \sin^2 \frac{\theta}{2}} \quad (1.9)$$

where  $M$  is the target mass, and  $\theta$  is the scattering angle. The invariant mass of elastic scattering follows  $W^2 = M^2 + 2M\nu - Q^2 = M^2$ , which gives  $\nu = Q^2/2M$ .

Since proton has structure, Eq. 1.8 needs to be extended to consider the spatial distribution. Two form factors are used to characterise the electric and magnetic distributions. The cross section of the elastic scattering of an electron off a nucleon then can be expressed as [7]:

$$\frac{d\sigma}{d\Omega} = \left(\frac{d\sigma}{d\Omega}\right)_{Mott} \left( \frac{G_E^2(Q^2) + \tau G_M^2(Q^2)}{1 + \tau} + 2\tau G_M^2(Q^2) \tan^2 \frac{\theta}{2} \right), \quad (1.10)$$

where  $\tau = -q^2/4M^2$ .  $G_E(Q^2)$  and  $G_M(Q^2)$  are the electromagnetic Sachs form factors, and are closely related to the nucleon charge and magnetic moment distributions.

### 1.1.3 Inelastic Scattering

As  $Q^2$  and  $\nu$  increase, electron scattering becomes inelastic. Excited states of the nucleon called nucleon resonances can be observed. The invariant mass follows  $W^2 = M^2 + 2M\nu - Q^2 = M_{N^*}^2$ , with  $M_{N^*}$  the mass of the resonance  $N^*$ . Usually, the resonance region refers to  $1.2 < W < 2.0\text{GeV}$ .

The first resonance state is the  $\Delta(1232)$ . In inclusive electron scattering experiments, this is usually the only unambiguously visible resonance state. For  $W > 1.4\text{GeV}$ , the higher resonances and their tails overlap.

As  $Q^2$  and  $\nu$  continue increasing, the electron scattering enters the deep inelastic scattering (DIS) region. This region is usually defined as  $W > 2\text{GeV}$  and  $Q^2 > 1\text{GeV}^2$ . The energy of virtual photon is large enough to break up the nucleon, and the partons inside the nucleon are resolved.

In the inelastic scattering,  $W > M$ , and  $2M\nu - Q^2 > 0$ , we define a dimensionless variable

$$x = \frac{Q^2}{2M\nu} \quad (1.11)$$



known as the Bjorken variable. In elastic scattering,  $x = 1$ . For all other scattering processes,  $0 < x < 1$ .

The cross section of inelastic electron scattering is:

$$\frac{d\sigma}{d\Omega dE'} = \left( \frac{d\sigma}{d\Omega} \right)_{Mott} \left( W_2(\nu, Q^2) + 2W_1(\nu, Q^2) \tan^2 \frac{\theta}{2} \right) \quad (1.12)$$

where  $W_1$  and  $W_2$  are known as structure functions, and are used to parametrize the internal structure of nucleons. The second term corresponds to the magnetic interaction.  $W_1$  and  $W_2$  are often substituted by two dimensionless structure functions expressed in terms of the Bjorken  $x$  and  $Q^2$ :

$$F_1(x, Q^2) = MW_1(\nu, Q^2), \quad (1.13)$$

$$F_2(x, Q^2) = \nu W_2(\nu, Q^2). \quad (1.14)$$

In the deep inelastic region of large  $Q^2$ , structure functions are observed to have weak dependence on  $Q^2$  for a fixed value of  $x$ . This phenomenon is known as *Bjorken scaling* and was also discovered by the original SLAC data [8]. This shows enormous difference from the behaviour of elastic and resonance scatterings off a finite size target, rather it follows the behaviour of electrons scattered off a point particle, *i.e.* quarks.

The region of Bjorken scaling is defined as [9]

$$Q^2 \rightarrow \infty, \text{ and } \nu \rightarrow \infty \text{ with } x = \frac{Q^2}{2M\nu} \text{ finite,}$$

which is known as the Bjorken limit. The structure functions become functions of only  $x$ :  $F_{1,2}(x)$ . In this limit, the electron nucleon scattering can be viewed as electron scattering off an asymptotically free parton inside the nucleon, and the Bjorken variable  $x$  can be viewed as the fraction of the nucleon's momentum carried by the struck quark in the infinite momentum frame.

The experimental results also showed the following relation:

$$2xF_1(x) = F_2(x)$$

which is known as the Callan-Gross relation [10]. This relation is predicted to hold for Dirac spin-1/2 particles.

Our experiment was carried out in the resonance region and aims to measure the polarized structure function  $g_2$ . We will describe them in details in the following sections.

## 1.2 Differential Cross Section Formalism

For the inclusive inelastic electron nucleon scattering illustrated in Fig. 1.1, the differential cross section for detecting the final electron in the solid angle  $d\Omega$  and in the final energy range  $(E', E' + dE')$  in the laboratory frame can be generalized as [11]:

$$\frac{d^2\sigma}{d\Omega dE'} = \frac{\alpha^2}{q^4} \frac{E'}{E} L_{\mu\nu} W^{\mu\nu}, \quad (1.15)$$

where  $\alpha$  is the electromagnetic coupling constant,  $L_{\mu\nu}$  represents the leptonic tensor, and  $W^{\mu\nu}$  parametrizes the hadronic tensor. The  $L_{\mu\nu}$  is known from quantum electrodynamics (QED) as:

$$L_{\mu\nu} = \sum_{s'} [\bar{u}(k', s') \gamma_\mu u(k, s)]^* [\bar{u}(k', s') \gamma_\nu u(k, s)], \quad (1.16)$$

where  $u(k, s)$  and  $\bar{u}(k', s')$  represent electron spinors,  $\gamma_\mu$  is one of the Dirac matrices. Neglecting the small lepton mass, this tensor can be expressed as:

$$L_{\mu\nu} = 2[p_\mu p'_\nu + p'_\mu p_\nu - g_{\mu\nu} p \cdot p' + i\epsilon_{\mu\nu\alpha\beta} s^\alpha q^\beta], \quad (1.17)$$

where  $s_\mu = \bar{u}\gamma_\mu\gamma_5 u$  is the lepton spin vector,  $g_{\mu\nu}$  is the metric tensor, and the Levi-Cevita follows the convention  $\epsilon_{0123} = +1$ . For an unpolarized beam, the anti-symmetric part of this tensor vanishes when averaging over the initial spin.

The hadronic tensor calculation is unknown yet. This tensor serves to parametrize our ignorance of the form of hadronic current. We express this tensor involving all possible transitions from the nucleon ground state  $|N(P)\rangle$  to any excited state  $|X(P')\rangle$  in the form:

$$W_{\mu\nu} = \frac{1}{2M} \sum_X \langle N_s(P) | J_\mu(0) | X(P') \rangle \langle X(P') | J_\nu(0) | N_s(P) \rangle \cdot (2\pi)^3 \delta^4(q + P - P'), \quad (1.18)$$

where  $J_\mu$  is the electromagnetic current operator and the delta function guarantees the energy and momentum conservations. Using the completeness of the final states  $|X\rangle$ ,  $W_{\mu\nu}$  can be written in a more compact way:

$$W_{\mu\nu} = \frac{1}{4\pi M} \int d^4z \langle N_s(P) | J_\mu(z) J_\nu(0) | N_s(P) \rangle, \quad (1.19)$$

where  $z$  is the spatial four-vector. Furthermore,  $W_{\mu\nu}$  can be split into symmetry and anti-symmetry parts:

$$W_{\mu\nu} = W_{\mu\nu}^{(S)}(q; P) + W_{\mu\nu}^{(A)}(q; P, s), \quad (1.20)$$

The most general form of the tensor  $W_{\mu\nu}$  must be composed of elements that follow Lorentz and gauge invariance and also parity conservation of the electromagnetic interaction. Here we express the symmetry part as:

$$W_{\mu\nu}^{(S)} = (-g_{\mu\nu} + \frac{q_\mu q_\nu}{q^2}) W_1(\nu, Q^2) + [(P_\mu - \frac{P \cdot q}{q^2} q_\mu)(P_\nu - \frac{P \cdot q}{q^2} q_\nu)] \frac{W_2(\nu, Q^2)}{M^2}, \quad (1.21)$$

and the anti-symmetry part as:

$$W_{\mu\nu}^{(A)} = i\epsilon_{\mu\nu\alpha\beta}q^\alpha \left( S^\beta G_1(\nu, Q^2) + [(P \cdot q)S^\beta - (S \cdot q)P^\beta] \frac{G_2(\nu, Q^2)}{M^2} \right). \quad (1.22)$$

where  $S^\mu = \bar{u}(P)\gamma^\mu\gamma_5 u(P)/2M$  represents the nucleon spin vector. For a nucleon at rest,  $S^\mu = (0, \chi_S^\dagger \vec{\sigma} \chi_S)$ , and  $\chi_S$  are the two component Pauli spinors.

This introduces four structure functions  $W_{1,2}(\nu, Q^2)$  and  $G_{1,2}(\nu, Q^2)$ . The first two describes the scattering of unpolarized particles, while the latter two describe the interaction between polarized leptons and polarized nucleons.

Similar to the definitions for unpolarized structure functions (see Eq. 1.13, 1.14),  $G_{1,2}$  are often substituted by two dimensionless structure functions expressed in terms of the Bjorken  $x$  and  $Q^2$ :

$$g_1(x, Q^2) = M\nu G_1(\nu, Q^2) \quad (1.23)$$

$$g_2(x, Q^2) = \nu^2 G_2(\nu, Q^2), \quad (1.24)$$

Averaging over the spin states of the incident electron and target nucleon gives the unpolarized differential cross section in the laboratory frame as shown in Eq. 1.12. Polarized structure functions will be discussed in the next section.

### 1.3 Polarized Structure Functions

In the case of polarized electron and nucleon, the cross section difference between polarized electron with spin  $s$  scattering off polarized nucleon with spin  $S$  and that with spin  $-S$  is [12]

$$\begin{aligned}
\frac{d^2\sigma_{s,S}}{d\Omega dE'} - \frac{d^2\sigma_{s,-S}}{d\Omega dE'} &= \left[ \frac{d^2\sigma}{d\Omega dE'}(k, s, P, S; k') - \frac{d^2\sigma}{d\Omega dE'}(k, s, P, -S; k') \right] \\
&= \frac{8\alpha^2 E'}{q^4 E} \left\{ [(q \cdot S)(q \cdot s) + Q^2(s \cdot S)]MG_1 \right. \\
&\quad \left. + Q^2[(s \cdot S)(P \cdot q) - (q \cdot S)(P \cdot s)]\frac{G_2}{M} \right\}, \tag{1.25}
\end{aligned}$$

where the  $G_1(P \cdot q, Q^2)$  and  $G_2(P \cdot q, Q^2)$  are two polarized structure functions. If the nucleons are longitudinally polarized, the spin of the initial lepton is along with or opposite to the nucleon polarization. Substituting  $G_{1,2}$  with  $g_{1,2}$ , the cross section difference becomes:

$$\Delta\sigma_{\parallel} \equiv \frac{d^2\sigma^{\Rightarrow}}{d\Omega dE'} - \frac{d^2\sigma^{\Leftarrow}}{d\Omega dE'} = -\frac{4\alpha^2 E'}{MQ^2 E\nu} [(E + E' \cos\theta)g_1(x, Q^2) - 2Mxg_2(x, Q^2)] \tag{1.26}$$

If the nucleons are transversely polarized, the spin of the leptons is perpendicular to the nucleon polarization. The cross section difference becomes:

$$\Delta\sigma_{\perp} \equiv \frac{d^2\sigma^{\rightarrow\uparrow}}{d\Omega dE'} - \frac{d^2\sigma^{\rightarrow\downarrow}}{d\Omega dE'} = -\frac{4\alpha^2 E'^2}{MQ^2 E\nu} \sin\theta [g_1(x, Q^2) + \frac{2E}{\nu}g_2(x, Q^2)] \tag{1.27}$$

We rewrite the unpolarized differential cross section Eq. 1.12 here in terms of  $F_{1,2}$ :

$$\sigma_{unpol} \equiv \frac{d\sigma}{d\Omega dE'} = \left( \frac{d\sigma}{d\Omega} \right)_{Mott} \left[ \frac{2}{M} F_1(x, Q^2) \tan^2 \frac{\theta}{2} + \frac{1}{\nu} F_2(x, Q^2) \right], \tag{1.28}$$

## 1.4 Structure Functions in the Quark-Parton Model

As has been briefly discussed in section 1.1.3, the Bjorken scaling can be clearly understood by the physical interpretation of the quark-parton model [2]. For a target

with a finite size, there must exist a form factor that depends on  $Q^2$ . Therefore, the scaling phenomenon is the result of scattering of point-like objects, the partons. In the quark-parton model, the nucleon is composed of a collection of point-like particles, which do not interact with each other. One of the particles carries a fraction  $x$  of the nucleon's longitudinal momentum and interacts with the virtual photon.

The nucleon cross section is thus a sum of the cross sections of each parton. The partons interact electromagnetically with the virtual photons, thus each term is weighted by its electric charge squared. Therefore,  $F_1(x)$  and  $g_1(x)$  can be expressed as [11]

$$F_1(x) = \frac{1}{2} \sum_i e_i^2 q_i(x) = \frac{1}{2} \sum_i e_i^2 \left[ q_i^\uparrow(x) + q_i^\downarrow(x) \right], \quad (1.29)$$

$$g_1(x) = \frac{1}{2} \sum_i e_i^2 \Delta q_i(x) = \frac{1}{2} \sum_i e_i^2 \left[ q_i^\uparrow(x) - q_i^\downarrow(x) \right], \quad (1.30)$$

where  $q_i^\uparrow(x)$  and  $q_i^\downarrow(x)$  are the number density of the  $i^{th}$  quark aligned parallel and anti-parallel to the nucleon spin, respectively, and carries the fraction  $x$  of the nucleon's momentum.  $q_i(x) = q_i^\uparrow(x) + q_i^\downarrow(x)$  is the unpolarized parton distribution function of the  $i^{th}$  parton, meaning the probability of finding the  $i^{th}$  parton within the nucleon carrying the fraction  $x$  of the nucleon's momentum.  $\Delta q_i(x) = q_i^\uparrow(x) - q_i^\downarrow(x)$  is the polarized parton distribution function.

The Callan-Gross relation [10] mentioned in Sec. 1.1.3 expresses  $F_2(x)$  in terms of  $F_1(x)$  as  $F_2(x) = 2xF_1(x)$ . The transverse polarized structure function  $g_2(x)$  has no simple physical interpretation within the quark-parton model [11]. However  $g_2(x)$  relates to the quark-gluon interaction inside the nucleon, and will be discussed more in chapter 2.

## 1.5 Operator Product Expansion

The Bjorken scaling behavior of structure functions are exactly true only in the Bjorken limit. At finite  $Q^2$ , there are higher order hard process contributions which come from the fact that the initial and scattered quarks can emit soft gluons. In order to calculate the cross section and define the nucleon structure, a method called the operator product expansion [13] was introduced. This method defines the product of operators as a sum of the same operator.

The operator product expansion (OPE) was introduced by Wilson [13] to conduct non-perturbative calculations of the quantum field theory (QFT). The OPE separates the perturbative part of a product of local operators from the non-perturbative part by expressing the product of the two operators in the small distance limit  $d \rightarrow 0$  as:

$$\lim_{d \rightarrow 0} \sigma_a(d) \sigma_b(0) = \sum_k C_{abk}(d) \sigma_k(0), \quad (1.31)$$

where  $C_{abk}$  are the Wilson coefficients, which contain the perturbative part and are calculable in perturbative QCD. Operators  $\sigma_k$  contain non-perturbative information, and are not calculable in perturbative QCD. Operators  $\sigma_k$  are quark and gluon operators of dimension  $d$  and spin  $n$ . The contribution of any operator to the differential cross section is of order:  $x^{-n} (\frac{M}{Q})^{D-n-2}$ . We define  $\tau \equiv d - n$  as the “twist”. At large  $Q^2$ , the leading twist  $\tau = 2$  dominates, while at small  $Q^2$  higher twist operators contribute more, and are not ignorable.

The OPE can be applied to the electromagnetic currents product in the hadronic tensor from Eq. 1.19. Then  $g_2$  can be derived under the OPE framework to be the sum of the leading-twist (twist-2) term and higher twist terms.

## 1.6 Chiral Perturbation Theory

For the low  $Q^2$  interactions, the strong coupling constant  $\alpha_s$  becomes large, thus QCD becomes highly non-perturbative. The calculations based on the quarks and gluons degrees of freedom becomes infeasible. An effective theory known as chiral perturbation theory ( $\chi$ PT) allows us to study QCD in the low-energy regime.  $\chi$ PT is based on the hadron degree of freedom [14], and constructed with an effective Lagrangian reproducing the symmetries and symmetry breaking patterns of QCD [11].

Considering the complete QCD Lagrangian [15]:

$$\mathcal{L}_{QCD} = -\frac{1}{4g^2}G_{\mu\nu}^a G^{\mu\nu,a} + \bar{q}i\gamma^\mu D_\mu q - \bar{q}\mathcal{M}q, \quad (1.32)$$

where  $G$  is the strength of the gluon field,  $q$  is the quark spinor, and  $\mathcal{M}$  is the quark mass matrix. The masses of  $u$  and  $d$  quarks are small compared to the hadronic mass scales, e.g. the proton's mass ( $m_u/M_p \approx 0.006$ ). We consider the limit of quark masses extremely close to zero, and treat the masses of light quarks as perturbations. For massless fermions, chirality is identical to the particle's helicity  $\hat{h}$ :  $\hat{h} = \frac{\vec{\sigma} \cdot \vec{p}}{|\vec{p}|}$ . The left and right handed quarks are defined as:

$$q_{R,L} = \frac{1}{2}(1 \pm \gamma_5)q, \quad (1.33)$$

The left and right handed quarks do not interact with each other so that the theory holds the  $SU(3)_L \times SU(3)_R$  symmetry, and the invariance of the Lagrangian under this group is known as chiral symmetry [11].

However, the ground state of QCD is asymmetric under chiral symmetry [15], which results in the spontaneous symmetry breaking to the  $SU(3)$  group. This is followed by the existence of eight Goldstone bosons [16]. In nature, these bosons are the pseudoscalar mesons: pions ( $\pi^\pm, \pi^0$ ), kaons ( $K^\pm, K^0, \bar{K}^0$ ), and eta ( $\eta$ ). In



addition, the existing mass of the light quark explicitly breaks chiral symmetry, and is treated as perturbations in  $\chi$ PT.

In the low-energy limit, the  $\chi$ PT Lagrangian is constructed as the sum of two parts:

$$\mathcal{L}_{QCD} = \mathcal{L}_{QCD}^0 + \mathcal{L}'_{QCD}, \quad (1.34)$$

where  $\mathcal{L}_{QCD}^0$  is the chiral symmetric part, and  $\mathcal{L}'_{QCD} = -\bar{q}\mathcal{M}q$  is regarded as a perturbation to the  $\mathcal{L}_{QCD}^0$ . The degrees of freedom are the Goldstone bosons.

The  $\chi$ PT expansion is performed in the order of small masses and momenta of the interacting particles. The convergence radius is expected to be limited, and can be tested by the measurements of the quantities calculable in  $\chi$ PT. Examples will be introduced and discussed in chapter 2.

# 2

## Structure Function $g_2$

### 2.1 Spin-dependent Structure Function $g_2$

The strong interaction, as one of the four fundamental interactions of nature, binds protons and neutrons together to form atomic nuclei, and binds quarks and gluons to form proton, neutron and other hadrons. Quantum Chromodynamics (QCD) with quark and gluon degrees of freedom is believed to be the theory of strong interaction. Two unique features of QCD are confinement and asymptotic freedom. Confinement describes the phenomenon that quarks and gluons are bound into hadrons, and cannot be observed directly. Asymptotic freedom describes the property that the strong coupling constant becomes asymptotically smaller when the distance between interacting constituent particles decreases.

These features of QCD make direct measurement of strong interaction complicated. If one uses low energy electrons to probe the nucleon, quarks are in the confinement region wrapped by dense gluon fields. If one uses high energy electrons to probe the nucleon, the strong interaction is so weak that quarks can be considered free, and the strong force can only be observed through the momentum distribution

of quarks. In order to study the one gluon exchange between quarks, the electron energy must be in the intermediate region where the strong coupling constant is large enough for one gluon exchange to be observed, but not too large that higher order terms begin to dominate.

As stated in Sec. 1.4,  $g_2$  is special because it has no simple interpretation in the quark-parton model [11]. The asymptotic-free quark part of this structure function completely depends on  $g_1$ , and is expressed as:

$$g_2^{WW}(x, Q^2) = -g_1(x, Q^2) + \int_x^1 \frac{g_1(y, Q^2)}{y} dy, \quad (2.1)$$

which is known as the Wandzura-Wilczek relation [17].

By subtracting  $g_2^{WW}$ , the remaining part of  $g_2$  is dominated by physics beyond the quark-parton model, such as quark-gluon coupling. With the method of OPE [18, 19, 20], the magnitude can be expressed in terms of the higher twist terms. Up to twist-3, the remaining part  $\bar{g}_2(x, Q^2)$  can be expressed as:

$$\bar{g}_2(x, Q^2) = - \int_x^1 \frac{\partial}{\partial y} \left[ \frac{m_q}{M} h_T(y, Q^2) + \zeta(y, Q^2) \right] \frac{dy}{y}, \quad (2.2)$$

where  $m_q$  is the quark mass,  $h_T(y, Q^2)$  is from the quark transverse polarization distribution. This term is suppressed by  $m_q/M$ , and is also twist-2.  $\zeta$  is the twist-3 part which is related to the quark-gluon interactions.

In total,  $g_2$  can be separated into twist-2 and higher twist components by ignoring the quark mass effect of order  $\mathcal{O}(m_q/\Lambda_{QCD})$  as:

$$g_2(x, Q^2) = g_2^{WW}(x, Q^2) + \bar{g}_2(x, Q^2). \quad (2.3)$$

$g_2^{WW}$  is only a good approximation of  $g_2$  in the limit  $Q^2 \rightarrow \infty$ . At finite  $Q^2$ ,  $g_2$  possesses strong deviations from leading twist behaviors, which means  $g_2$  provides a

good opportunity to study the higher twist effect, and quark-gluon interactions.

## 2.2 Sum Rule and Moments

Chapter 1 introduced the structure functions to parametrize the internal structure of the nucleon. However, the existing theoretical tools are not able to directly calculate the structure functions, and instead they provide calculations of the moments of the structure functions, and sum rules which relate the Compton scattering amplitudes to the integrals of the photoabsorption cross sections. The extension from real to virtual photon enables probes with various energies, i.e. scales. These moments and sum rules provide good opportunities to test theoretical predictions in order to probe the internal structures of the nucleon.

### 2.2.1 Virtual Photoabsorption Cross Sections

In Sec. 1.2, the inclusive electron scattering cross section is expressed in terms of four structure functions. The cross section can also be expressed as the virtual photon absorption cross section [21, 22]:

$$\frac{d\sigma}{d\Omega dE'} = \Gamma_v(\sigma_T + \epsilon\sigma_L - hP_x\sqrt{2\epsilon(1-\epsilon)}\sigma_{LT} - hP_z\sqrt{1-\epsilon^2}\sigma_{TT}), \quad (2.4)$$

where  $h = \pm 1$  denotes the helicity of the incoming electrons, and  $P_z$  and  $P_x$  denote the target polarization parallel and perpendicular to the virtual photon momentum, respectively.  $\Gamma_v$  and  $\epsilon$  are virtual photon flux factor and the transverse polarization of the virtual photon expressed as:

$$\Gamma_v = \frac{\alpha}{2\pi} \frac{E'}{E} \frac{K}{Q^2} \frac{1}{1-\epsilon}, \quad (2.5)$$

$$\epsilon = \frac{1}{1 + 2(1 + \frac{\nu^2}{Q^2})\tan^2(\frac{\theta}{2})}. \quad (2.6)$$

The virtual photon flux  $K$  is convention dependent, and one of the conventions is by Hand [23], and relates the flux with the “equivalent photon energy” as:

$$K = \nu(1 - x) = \frac{(W^2 - M^2)}{2M}. \quad (2.7)$$

The four partial cross sections consist of the longitudinal  $\sigma_L$ , transverse  $\sigma_T$ , and two interference terms - longitudinal-transverse  $\sigma_{LT}$  and transverse-transverse  $\sigma_{TT}$ . In the real photon limit  $Q^2 = 0$ ,  $\sigma_L$  vanishes, and the total photoabsorption cross section  $\sigma(\nu) = \sigma_T(\nu)$ .  $\sigma_T$  and  $\sigma_{TT}$  can be expressed in terms of the helicity dependent photoabsorption cross sections  $\sigma_{3/2}$  and  $\sigma_{1/2}$ , which correspond to total helicity projection of the photon and target equal to  $\frac{3}{2}$  and  $\frac{1}{2}$ , respectively. Fig. 2.1 illustrates the helicity projections.

$$\sigma_T = \frac{1}{2}(\sigma_{1/2} + \sigma_{3/2}), \quad (2.8)$$

$$\sigma_{TT} = \frac{1}{2}(\sigma_{1/2} - \sigma_{3/2}). \quad (2.9)$$

The four virtual photoabsorption cross sections are related to the structure functions  $F_{1,2}$  and  $g_{1,2}$  as:

$$\sigma_T = \frac{4\pi^2\alpha}{MK} F_1, \quad (2.10)$$

$$\sigma_L = \frac{4\pi^2\alpha}{K} \left( \frac{1 + \gamma^2}{\gamma^2\nu} F_2 - \frac{1}{M} F_1 \right), \quad (2.11)$$

$$\sigma_{TT} = \frac{4\pi^2\alpha}{MK} (g_1 - \gamma^2 g_2), \quad (2.12)$$

$$\sigma_{LT} = \frac{4\pi^2\alpha}{MK} \gamma (g_1 + g_2), \quad (2.13)$$

where  $\gamma = Q/\nu$ , and the relations depend on the virtual photon flux  $K$ .

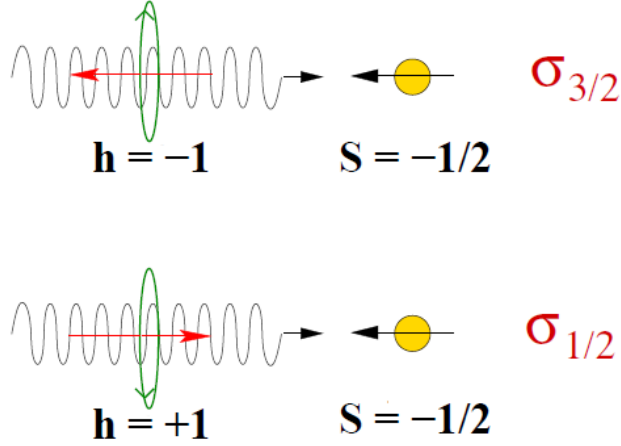


FIGURE 2.1: Schematic of the helicity dependent virtual photoabsorption cross section  $\sigma_{\frac{1}{2}}$  and  $\sigma_{\frac{3}{2}}$  [24].

### 2.2.2 Generalized Forward Spin polarizability $\gamma_0$ and Longitudinal-Transverse Polarizability $\delta_{LT}$

The spin-flip forward doubly-virtual Compton scattering (VVCS) amplitude  $g_{TT}$  satisfies an unsubtracted dispersion relation as [25, 21]<sup>1</sup>:

$$\text{Re}[g_{TT}(\nu, Q^2) - g_{TT}^{pole}(\nu, Q^2)] = \frac{\nu}{2\pi^2} \mathcal{P} \int_{\nu_0}^{\infty} \frac{K(\nu', Q^2) \sigma_{TT}(\nu', Q^2)}{\nu'^2 - \nu^2} d\nu', \quad (2.14)$$

where the  $g_{TT}^{pole}$  is the nucleon pole (elastic) contribution,  $\mathcal{P}$  denotes the principle value integral. The lower limit of the integration  $\nu_0$  is the pion-production threshold of the nucleon. If we expand the integration at low energy, the relation becomes:

$$\text{Re}[g_{TT}(\nu, Q^2) - g_{TT}^{pole}(\nu, Q^2)] = \frac{2\alpha}{M^2} I_A(Q^2) \nu + \gamma_0(Q^2) \nu^3 + \mathcal{O}(\nu^5). \quad (2.15)$$

The  $\mathcal{O}(\nu^3)$  term coefficient  $\gamma_0$  leads to a sum rule of the generalized forward spin polarizability by implementing Eq. 2.12 [21]:

<sup>1</sup> Assume  $g_{TT}$  has appropriate convergence behaviour.

$$\begin{aligned}
\gamma_0(Q^2) &= \left(\frac{1}{2\pi^2}\right) \int_{\nu_0}^{\infty} \frac{K(\nu, Q^2)}{\nu} \frac{\sigma_{TT}(\nu, Q^2)}{\nu^3} d\nu \\
&= \frac{16\alpha M^2}{Q^6} \int_0^{x_0} \left[ g_1(x, Q^2) - \frac{4M^2}{Q^2} x^2 g_2(x, Q^2) \right] x^2 dx.
\end{aligned} \tag{2.16}$$

Similarly the longitudinal-transverse interference amplitude  $g_{LT}$  can be expressed as:

$$Re[g_{LT}(\nu, Q^2) - g_{LT}^{pole}(\nu, Q^2)] = \frac{2\alpha}{M^2} Q I_3(Q^2) + Q \delta_{LT}(Q^2) \nu^2 + \mathcal{O}(\nu^4). \tag{2.17}$$

The  $\mathcal{O}(\nu^2)$  term gives the generalized longitudinal-transverse polarizability [21]:

$$\begin{aligned}
\delta_{LT}(Q^2) &= \left(\frac{1}{2\pi^2}\right) \int_{\nu_0}^{\infty} \frac{K(\nu, Q^2)}{\nu} \frac{\sigma_{LT}(\nu, Q^2)}{Q\nu^2} d\nu \\
&= \frac{16\alpha M^2}{Q^6} \int_0^{x_0} [g_1(x, Q^2) + g_2(x, Q^2)] x^2 dx.
\end{aligned} \tag{2.18}$$

### 2.2.3 The Burkhardt-Cottingham Sum Rule

The spin-flip amplitude  $g_{TT}$  and  $g_{LT}$  are also related to the covariant spin-dependent VVCS amplitude  $S_1$  and  $S_2$  as:

$$S_1(\nu, Q^2) = \frac{\nu M}{\nu^2 + Q^2} [g_{TT}(\nu, Q^2) + \frac{Q}{\nu} g_{LT}(\nu, Q^2)], \tag{2.19}$$

$$S_2(\nu, Q^2) = -\frac{M^2}{\nu^2 + Q^2} [g_{TT}(\nu, Q^2) - \frac{\nu}{Q} g_{LT}(\nu, Q^2)]. \tag{2.20}$$

Considering the unsubtracted dispersion relations of  $S_2$  and  $\nu S_2$ , we obtain the “superconvergence relation” [21]:

$$\int_0^{\infty} Im S_2(\nu, Q^2) d\nu = 0. \tag{2.21}$$

Expressing Eq. 2.21 in terms of  $g_2$ , the relation is written as:

$$\int_0^1 g_2(x, Q^2) dx = 0, \quad (2.22)$$

which is known as the Burkhardt-Cottingham (BC) sum rule [26] and is valid for any value of  $Q^2$ . Therefore the test of the BC sum rule can be taken either in the DIS region or the low-energy region.

## 2.3 Existing Measurements

### 2.3.1 $g_2$

The earliest results for  $g_2$  are from SLAC in the DIS region by measuring both the longitudinal and the transverse asymmetries [27]. During the same period with SLAC, the SMC collaboration at CERN used a polarized muon beam instead of a polarized electron beam to extract the  $g_{1,2}$  from the longitudinal and transverse asymmetries of the polarized proton and deuteron target in the DIS region [28, 29, 30, 31].

The experiments that followed continued to measure  $g_2$  for both neutron and proton in the DIS region. The most precise  $g_2$  data for the proton and deuteron are from SLAC E155x [32, 33]. The  $g_2$  for the neutron was also extracted by the difference of the proton and deuteron data from E155x. Also, SLAC E143 [34] and E155 [35] experiments contributed precise data to  $g_2$ . Fig. 2.2 shows the  $g_2$  results from SLAC E143, E155 and E155x. The data points mostly match the  $g_2^{WW}$  curve (Eq. 2.1), but with some deviations, especially in the small  $x$  region. The differences between the  $g_2$  data and the  $g_2^{WW}$  reveal the high-twist effect, which is sensitive to the quark-gluon interaction.

With the high luminosity polarized beam, JLab provided precise  $g_2$  data for the neutron in the DIS region. Experiment E97-103 obtained  $g_2^n$  data at low  $Q^2$  and DIS



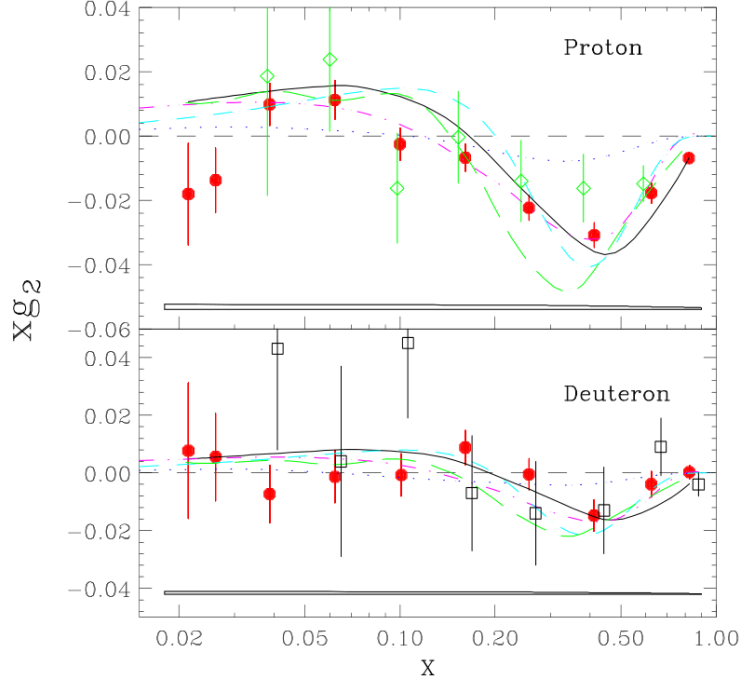


FIGURE 2.2: Result of  $g_2$  for the proton and deuteron in DIS region [35]. The solid circle is from E155x, the open diamond is from E143, and the open square is from E155. The solid line is the  $g_2^{WW}$  at the average  $Q^2$  of E155x. Also the model calculations from Stratmann [36] (dash-dot-dot), Song [37] (dot), Weigel [38] (dash-dot) and Wakamatsu [39] (dash) are compared.

region in order to study the  $Q^2$  dependence of  $g_2$  [40], as shown in Fig. 2.3. Five  $Q^2$  values are covered in the  $Q^2$  range of  $0.58 < Q^2 < 1.36 \text{ GeV}^2$  at  $x \approx 2$ . The result shows that  $g_2$  is consistently higher than  $g_2^{WW}$  in this kinematic range, which was observed by any experiment for the first time.

Comparing with the DIS region, the resonance region shows stronger effect of the quark-gluon interaction. Many experiments collected  $g_2$  data in the region of  $W < 2 \text{ GeV}$ , which offered opportunities to study the internal structure of the nucleon resonance states. The first experiment to measure the  $g_2$  in the resonance region is the E143 experiment at SLAC with the beam energy of  $9.7 \text{ GeV}$  and the  $Q^2$  value of  $0.5 \text{ GeV}^2$  and  $1.2 \text{ GeV}^2$  [41]. Experiment E94-010 at Jefferson Lab collected extensive data for the neutron [42] at low  $Q^2$ , as shown in Fig. 2.4. The data show

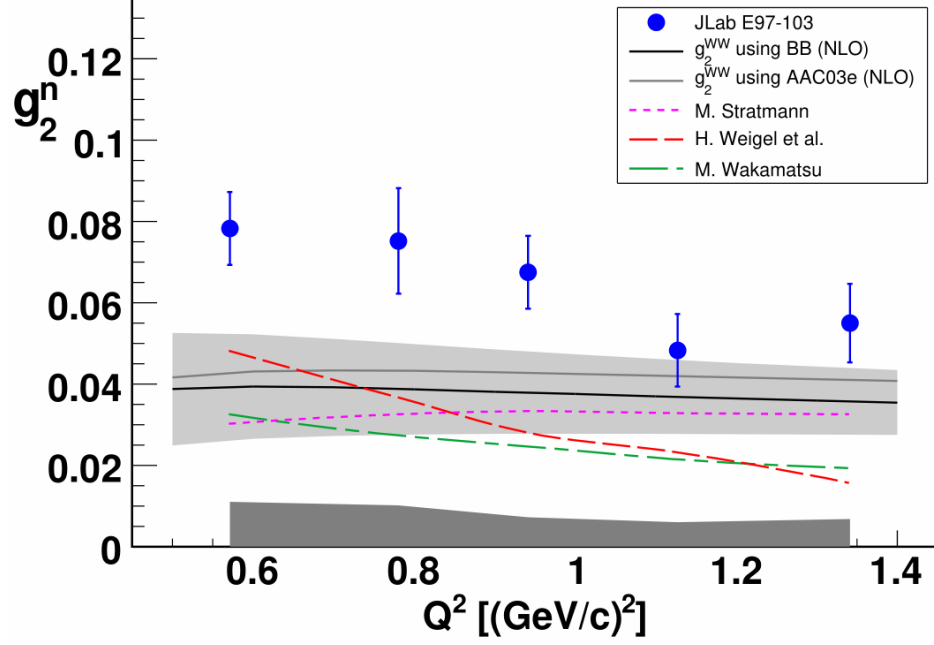


FIGURE 2.3:  $g_2^n$  extracted from experiment E97-103 at JLab for  $x \approx 0.2$  [40]. The low-dark grey band is the systematic uncertainties. The error bar represents the statistical uncertainties. The light grey line and the dark solid line with grey uncertainty band are  $g_2^{WW}$  from the fit of world  $g_1$  data.

a significantly positive response of  $g_2$  in the  $\Delta(1232)$  resonance region, and a large deviation from that of  $g_2^{WW}$ .

Currently the lowest momentum transfer investigated for proton  $g_2$  is  $1.3 \text{ GeV}^2$  by the RSS collaboration [43] in Hall C at Jefferson Lab. The results are shown in Fig. 2.5. The comparison of  $g_2$  and  $g_2^{WW}$  also provides evidence that  $g_2^{WW}$  is insufficient to describe the data in the low  $Q^2$  region. These data all showed the significance of higher-twist terms in the low  $Q^2$  range.

### 2.3.2 BC Sum Rule

The first moment of  $g_2$  is expected to be 0 in all of the  $Q^2$  ranges as the result of the BC sum rule. The first measurement for the first moment of  $g_2$  is from E155x at SLAC, which included the results of proton, deuteron and neutron (extracted from the difference of proton and deuteron data). Neutron  $g_2$  integral was extensively

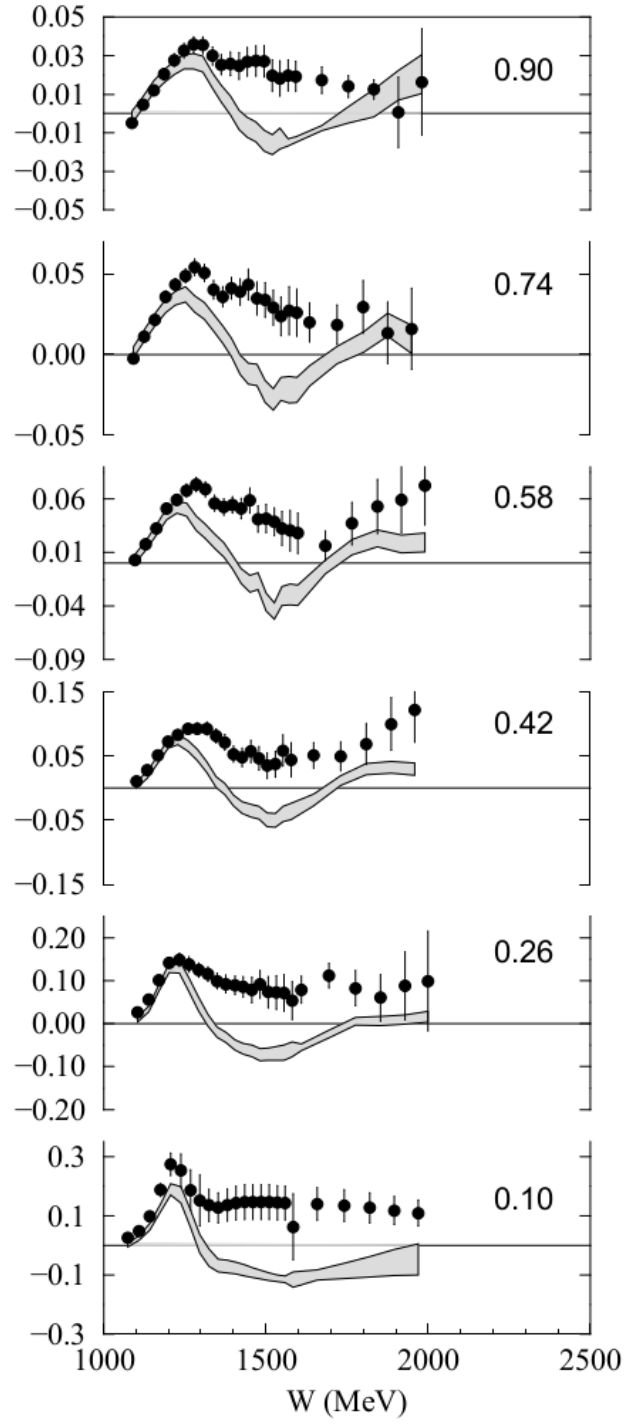


FIGURE 2.4:  $g_2^n$  extracted from experiment E94-010 for different  $Q^2$  values in the resonance region, and compared with  $g_2^{WW}$  (grey band) [42]. The unit for the constant  $Q^2$  in each panel is  $\text{GeV}^2$ .

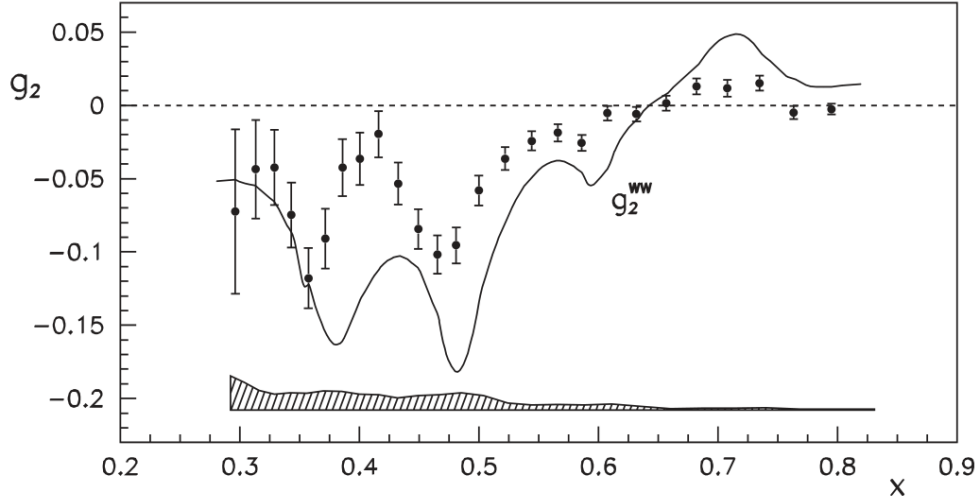


FIGURE 2.5: Proton  $g_2$  results and the  $g_2^{WW}$  (line) in resonance region from *RSS* collaboration [43]. The  $\Delta(1232)$  resonance region is at large  $x$  around 0.7.

extracted over a wide kinematic region in several experiments at JLab Hall A: E94-010 [44], E99-117 [45], E97-103 [40], E97-110 [46], E02-012 [47]. The RSS experiment in Hall C at JLab provided the proton  $g_2$  integral in the average  $Q^2$  of  $1.3 \text{ GeV}^2$  [43]. The unmeasured low  $x$  DIS contribution mostly uses the assumption of  $g_2 = g_2^{WW}$ , and the elastic contribution ( $x=1$ ) is mostly from the well known elastic form factors. The results for the BC sum rule are shown in Fig. 2.6.

The neutron data show agreement with the BC sum rule within a large error bar. The neutron data from RSS also agree with the BC sum rule. Other extensive data from JLab Hall A were extracted by using longitudinally and transversely polarized  $^3\text{He}$  target. The results from E94-010 in the measured region show a significantly positive value, but consistent with 0 after extended to the elastic and DIS regions. The total integral exhibits a significant cancellation of the inelastic and elastic contributions. Most precise data is from E97-110, E94-010 and E01-012, which are consistent with 0.

The proton data from E155x show large deviation from the BC sum rule, while

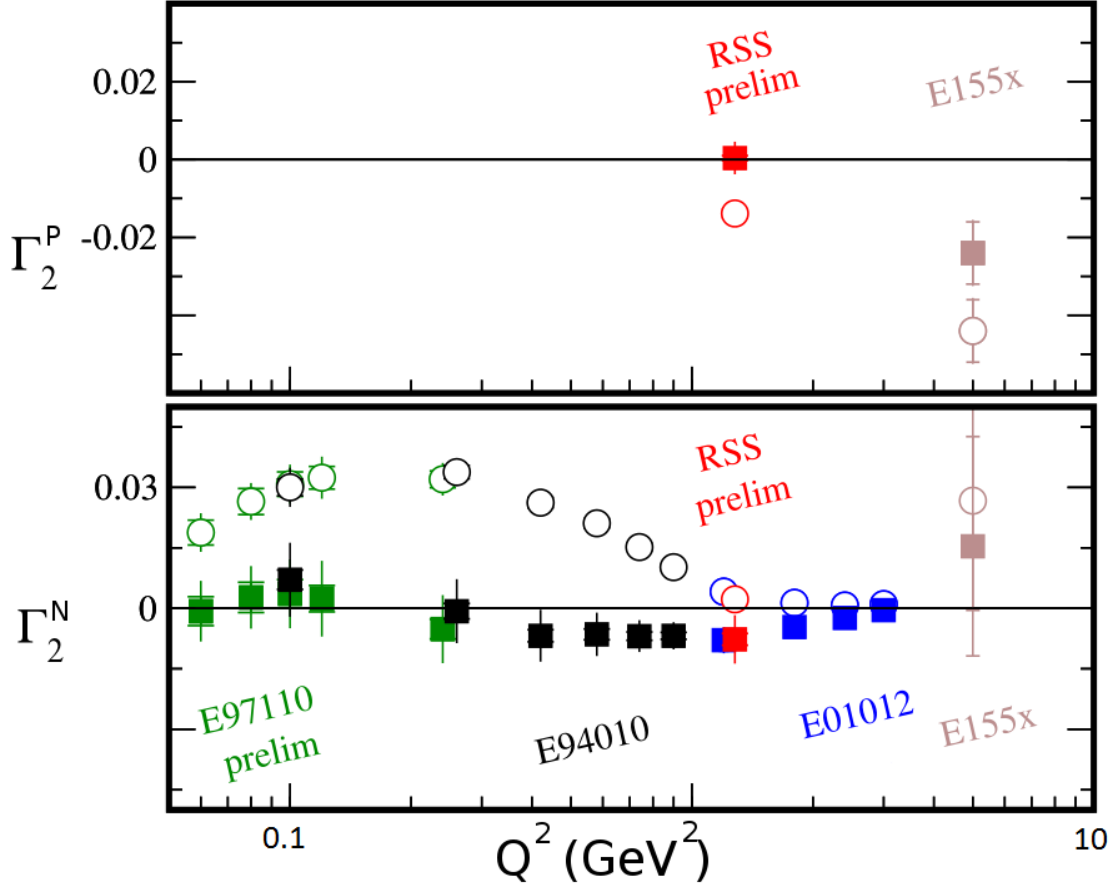


FIGURE 2.6: Verification of BC sum rule [48]. The top plot is for proton and the bottom one is for neutron. The open circle are the measured values, while the solid square are the total integral for  $0 \leq x \leq 1$ . The proton data is from JLab RSS experiment (red) and SLAC E155x experiment (brown). The neutron data is from JLab E97-110, E94-010 [49], E01-012 [47] and RSS experiment and SLAC E155x experiment. The neutron data from RSS and E155x is extracted from proton and deuteron data, while others are from  $^3\text{He}$  data.

the error bar is large. For the  $x \rightarrow 0$  extrapolation, they assumed  $g_2 = g_2^{WW}$ , which is difficult to quantify. The preliminary result from RSS in the measured resonance region is negative, and it is consistent with 0 after the elastic contribution and the small- $x$  part are added. The proton data on the BC sum rule are scarce. Data from this experiment E08-027 will help fill this gap.

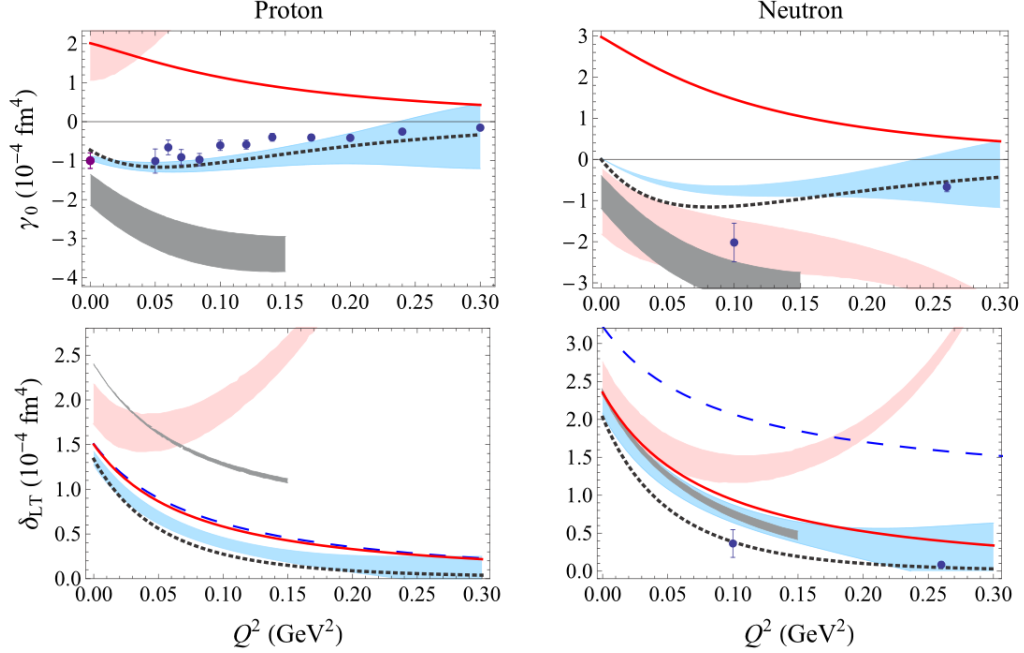


FIGURE 2.7: Generalized spin polarizabilities of proton and neutron. The proton  $\gamma_0$  data points are from Mainz ( $Q^2 = 0$ , purple square) [50] and EG1 experiment at JLab Hall B (finite  $Q^2$ , blue dots) [51]. All the neutron data points (blue dots) are from E94-010 experiment [49]. Red solid lines and blue bands are the baryon  $\chi PT$  LO and NLO results calculated by Lensky, et al. [52]. Black dotted lines are from MAID 2007. Grey bands are the covariant  $B\chi PT$  calculations [53]. Blue dashed lines are the  $\mathcal{O}(p^4)$  HB calculations [54], off the scale in the upper panels. Red bands are the  $RB\chi PT$  calculation [55].

### 2.3.3 Spin polarizabilities $\gamma_0$ and $\delta_{LT}$

The experimental results compared with the prediction of the  $\chi PT$  calculation are shown in Fig. 2.7. Since the forward spin polarizability  $\gamma_0$  can be expressed as the photoabsorption cross section from Eq. 2.16, it can be measured by the real photon Compton scattering experiment with  $Q^2 = 0$ . An experiment at MAMI (Mainz) measured the  $\gamma_0$  by using a circularly polarized photon beam on a longitudinally polarized proton (butanol) target [56]. Fig. 2.7 shows the proton  $\gamma_0$  results as purple dots.

The first results for the neutron  $\gamma_0$  and  $\delta_{LT}$  were obtained from E94-010 experiment at Jefferson Lab [49] (blue dots for neutron  $\gamma_0$  and  $\delta_{LT}$  in Fig. 2.7). Top right

panel of Fig. 2.7 shows the results of  $\gamma_0^n(Q^2)$ , and the comparison with  $\chi PT$  calculations and MAID predictions. At  $Q^2 = 0.1 \text{ GeV}^2$ , the experimental result agrees with the  $RB\chi PT$  calculation (Red band), but discrepancies with the  $HB\chi PT$  calculation are so large that the calculation is off scale in the panel. The  $\gamma_0$  is sensitive to the contribution of the  $\Delta$  resonance, which implies the importance of understanding this contribution. The MAID model predictions agree with the result at higher  $Q^2$  point, while overestimate the lower one.

Since  $\delta_{LT}$  is insensitive to the  $\Delta$  resonance contribution, it was believed that  $\delta_{LT}$  should be more suitable to provide tests for the  $\chi PT$  calculations [54, 55]. Bottom right panel of Fig. 2.7 shows the results of  $\delta_{LT}$ , and the comparison with  $\chi PT$  calculations and MAID predictions. MAID describes the data quite well. However, the data show a significant disagreement with both  $HB\chi PT$  (blue dashed line) and  $RB\chi PT$  predictions (red band), which is known as the “ $\delta_{LT}$  puzzle”. The puzzle presents a challenge to the  $\chi PT$  calculations. However, recent calculations using leading-order and next-to-leading-order chiral perturbation theory show reasonable agreement with data [52] (red solid line and blue band in Fig. 2.7), which might suggest that the  $\delta_{LT}$  puzzle is solved.

The proton data for  $\delta_{LT}$ , absent in Fig. 2.7, can be obtained in this experiment E08-027, are needed for further comparison and understanding of  $\chi PT$  calculations.

## The Experiment

### 3.1 Overview

Experiment E08-027 (g2p) was conducted at the Thomas Jefferson National Accelerator Facility (Jefferson Lab) in experimental Hall A from March to May 2012. Inclusive measurements were performed at forward angles with polarized beam and target to obtain the proton spin-dependent cross sections at low  $Q^2$  region ( $0.02 < Q^2 < 0.2$   $\text{GeV}^2$ ). From these data, the proton spin structure function  $g_2^p$  will be extracted. This experiment aims at measuring  $g_2^p$  in the low  $Q^2$  region ( $0.02 < Q^2 < 0.2$   $\text{GeV}^2$ ) for the first time. The obtained g2p data also allow us to extract the longitudinal-transverse spin polarizability of the proton, which will provide a benchmark test of  $\chi$ PT calculations [57, 58, 59, 60]. The results from this experiment can be used to test the Burkhardt-Cottingham sum rule [61].

Fig. 3.1 shows the kinematic coverage of the experiment. Longitudinally polarized electron beams with four incident energies were scattered off a transversely polarized  $\text{NH}_3$  target. The scattered electrons at  $6^\circ$  were detected in the Hall A high resolution spectrometers (HRSs). The small scattering angles were achieved with a pair of



septum magnets to bend electrons into HRSs which were positioned at  $12.5^\circ$ . In each configuration with different beam energy and target field combination, a series of different HRS momentum settings were utilized to detect a spectrum of scattered electron momenta. In this way, a two dimensional coverage of  $Q^2$  and  $W$  were achieved.

## 3.2 Author Contributions

The g2p experiment and data analysis are the work of the E08-027 collaboration. My main contributions to the experiment and the analysis are listed here. Some work described in this thesis were done by other collaborators to show a full description of the experiment. In these cases, the corresponding technotes or papers are cited.

Before the experiment, I mainly worked on the preparation of the optics study. I participated in the planning of the optics data taking. With the magnetic field simulation program, I redesigned the current configuration of the spectrometer magnets for the data taking of the g2p experiment. The results from the simulation program were also used for the design of a few equipments, such as the local beam dump. I also did the vertical drift chamber (VDC) time calibration to optimize the accuracy of the tracking information from the VDC.

During the commissioning of the experiment, a study of the septum magnet current scan was conducted to test the performance of the septum magnets. I analyzed the data and found the current predicted from the field map was far from the correct value. A new field map was provided and a new set of current scans was done before the experiment to find the optimal current setting. I also led the optics data taking during the experiment running. Optics data were taken for each energy configuration. The right septum magnet was broken twice during the experiment. The current scan was done after each time the magnet was recovered. I also heavily participated in the entire data taking of the experiment, which includes taking data as planned,

monitoring the online results and taking care of problematic situations during the experiment.

For the data analysis after the experiment, I organized the information and generated the database for the data processing from the raw data. I did the central angle calibration to determine the reference angle for the optics calibration. I did the optics calibration for the optics without target field, and the optics for the setting of 1.7 GeV beam energy, 2.5 T target field. I also tuned the magnetic field simulation program and fit the transport functions from the results. The transport functions were used to simulate the physics process of this experiment. I also studied the acceptance effects of this experiment. Last but not least, I extracted the physics results of asymmetries and  $g_1$  and  $g_2$  values for this thesis.

The following chapters will present these studies in details. This chapter will first discuss the polarized electron beam, and the experimental setup in Hall A.

### 3.3 The Electron Accelerator

Jefferson Lab, in its 6-GeV era, consisted of a state-of-the-art continuous wave (CW) electron beam accelerator, and three experimental halls (A, B, and C) that utilize the beam for medium energy physics. The electron accelerator consists of one polarized source, two super-conducting linear accelerators (linac), and two re-circulation arcs (magnets). Fig. 3.2 illustrates the layout of the accelerator and its components.

The polarized electron beam is produced by illuminating circularly polarized photons onto a gallium arsenide (GaAs) photocathode. The electron beam then enters into the accelerator after being accelerated to 45 MeV in the injector. Each linac can accelerate the electron beam up to from 400 to 600 MeV, and the electron beam can pass through two linacs up to 5 rounds. Therefore, the energy of electron beam can range from 0.8 GeV to maximum about 6 GeV.

After passing through the south linac and reaching the desired beam energy one

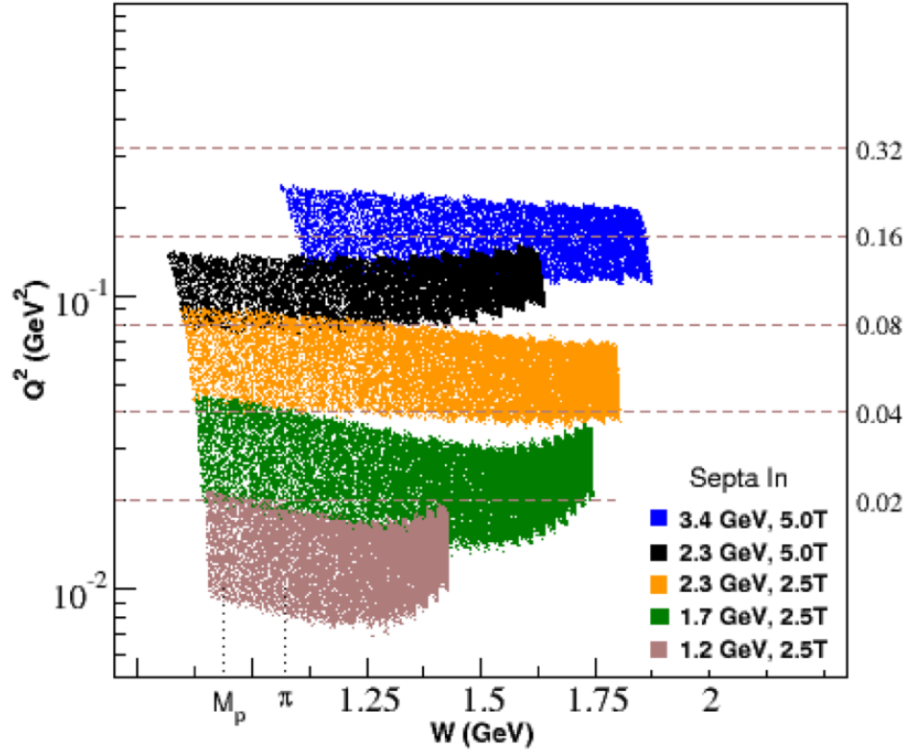


FIGURE 3.1: Kinematic coverage of experiment E08-027.

hall needs, the beam will be directed into the hall's transport channel. During the g2p experiment, 1.2 GeV, 1.7 GeV, 2.3 GeV, and 3.3 GeV beams were delivered to Hall A for production data taking.

### 3.3.1 Beam Energy

The beam energy in the g2p experiment was using the Arc energy measurement. The principle of this measurement is to determine the electron momentum with the bending angle in a well determined magnetic field. The relation can be expressed as

$$p = qB \cdot r = qB \cdot \frac{l}{\theta} = q \frac{\int \vec{B} \cdot d\vec{l}}{\theta}. \quad (3.1)$$

Fig. 3.3 shows the layout of the arc measurement including eight dipole magnets,

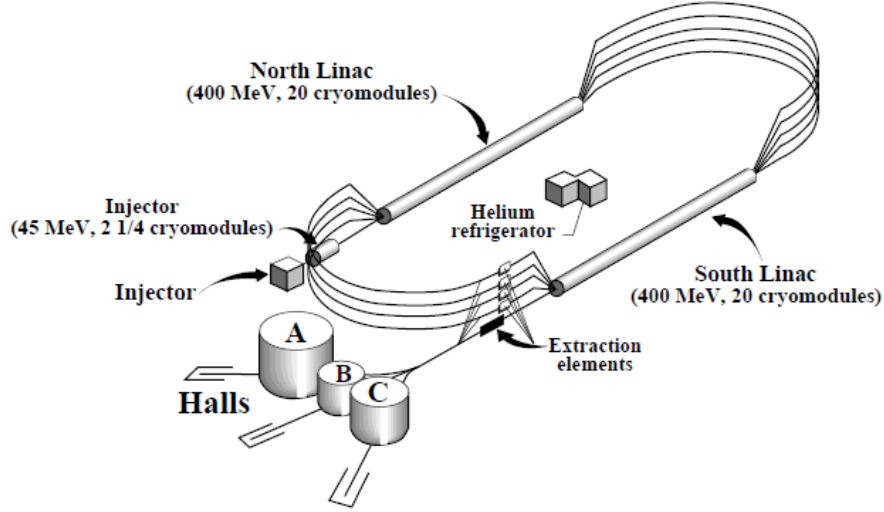


FIGURE 3.2: Schematic of the Jefferson Lab accelerator and experimental halls. Figure is from Ref. [24]

two sets of superharps (wire scanners). The nominal deflecting angle is  $34.3^\circ$ , and the superharps determine any deviations from the nominal values. The arc measurement determines the absolute energy values to the  $2 \times 10^{-4}$  GeV level.

During the g2p experiment, the beam energy was continuously monitored with the Tiefenback measurement. This measurement is non-invasive and uses the beam position monitors (BPMs) in arc to provide the bending angle. The uncertainty from this measurement is at  $5 \times 10^{-4}$  GeV level.

### 3.4 Hall A Beamline

The experimental Hall A is the largest hall among the existing halls. Fig. 3.4 shows a picture of Hall A. This hall contains two high momentum resolution spectrometers. The maximum momentum the spectrometers can reach is about 4.0 GeV. The E08-027 (g2p) experiment used a  $\text{NH}_3$  target as an effective polarized proton target, the polarization of which is sensitive to temperature and radiation. Low beam currents

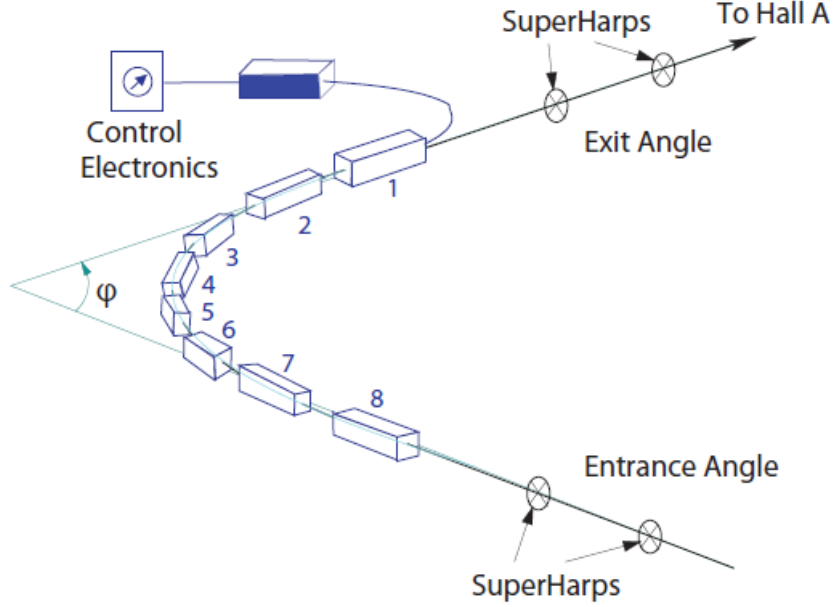


FIGURE 3.3: Schematic of the arc energy measurement. Figure is from Ref. [62]

(5 to 100nA) were required to minimize the depolarization of the target. This target was used for the first time in Hall A, therefore, beamline equipments in Hall A were upgraded for the g2p experiment. Fig. 3.5 illustrates the overview of the beamline, the components of which will be discussed in the following sections.

#### 3.4.1 Beam Current Monitors

g2p experiment utilized two beam current monitors (BCMs) to measure the beam current, which were located 23 m upstream from the target. The BCMs are two RF cavities which were tuned to match the beam frequency (1497 MHz), therefore the outputs' voltages of these cavities are proportional to the beam current.

In order to precisely measure the low beam current, new beam current monitor (BCM) receiver was designed and built. A tungsten calorimeter was installed to calibrate BCMs in the low current region. The principle of using the tungsten calorimeter to calibrate the beam current is to use the temperature raised by the

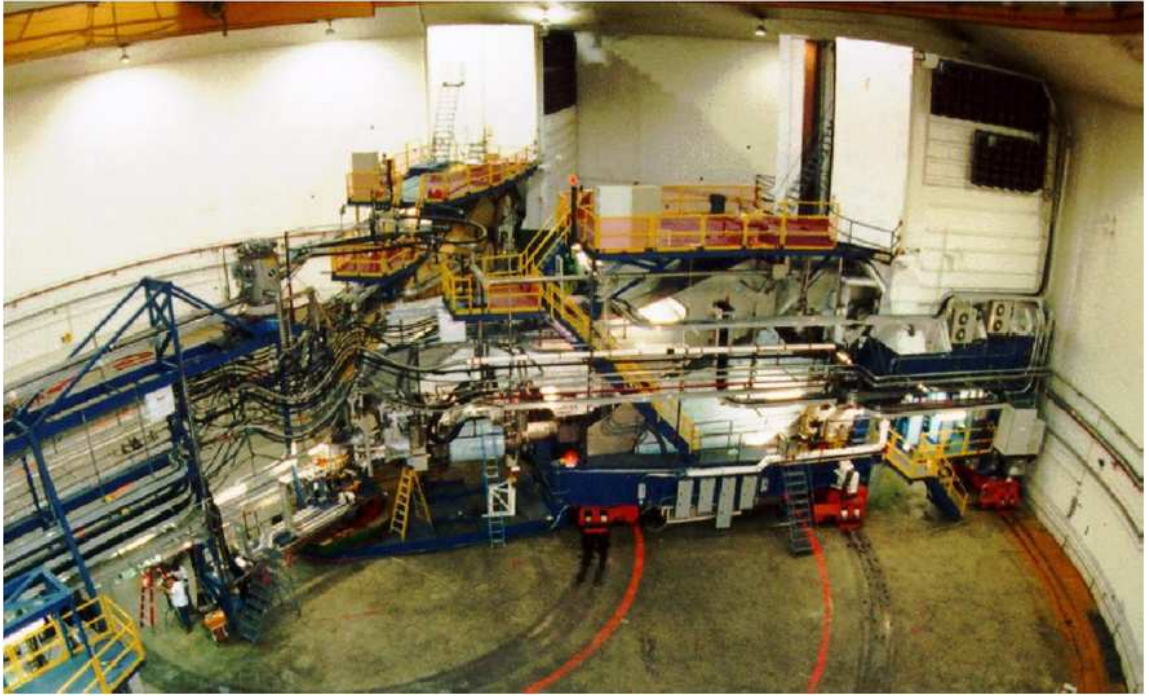


FIGURE 3.4: Picture of Hall A.

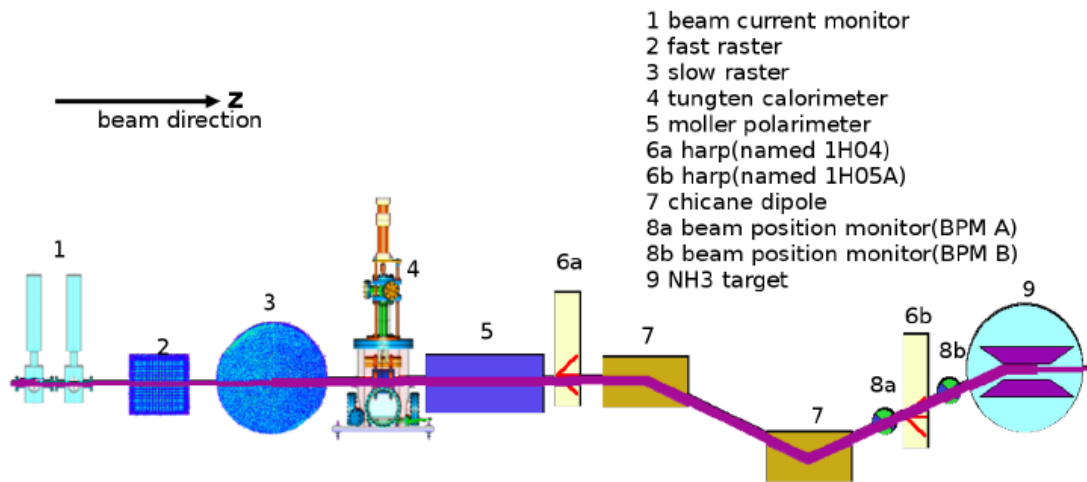


FIGURE 3.5: The beamline of the g2p experiment. Figure is from Ref. [63]

beam [64].

#### *3.4.2 Beam Position Monitors and Rasters*

For the g2p experiment, two beam position monitors (BPMs) located 95.5cm and 69cm upstream from the target were used to measure the beam positions and directions at the target. BPM is a cavity with four antennas oriented at  $45^\circ$  from the horizontal and vertical planes. When the beam passes through the BPM system, the antennas pick up signals that are inversely proportional to the distance from the beam.

Because of the low beam current (5 to 100nA) during the g2p experiment, the existing beam position monitors (BPMs) and calibration methods did not work at such low currents, new BPM readout electronics system were designed and diagnosed for this situation. A pair of new superharps were installed to calibrate the BPMs [63].

The size of the beam spot is around  $100\mu\text{m}$  when it enters Hall A, which will cast intensive energy onto one small spot of the target. Thus, the beam was rastered to avoid overheating the target material and minimize the depolarization of the target. For the g2p experiment, in addition to the existing fast raster system, a slow raster system was installed at 17m upstream from the target. The fast raster is a square shape of  $2\text{mm} \times 2\text{mm}$ , and slow raster is a circle shape of 2cm diameter by adjusting the frequency and magnitude of the magnetic field of the steering magnets. A 2.2cm circular rastered beam was achieved combining these two rasters. Fig. 3.6 shows an example of the rastered beam pattern.

#### *3.4.3 Beam Helicity*

For the g2p experiment, the inclusive electron scattering cross section difference between two opposite helicity states of the electron beam was formed to extract the  $g_2$  structure function. Thus the helicity scheme of the electron beam was recorded

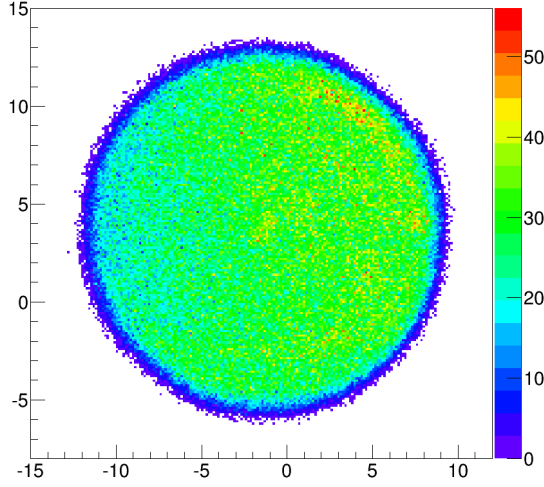


FIGURE 3.6: The circular rastered beam pattern. The axes are in the unit of mm.

and decoded to obtain the helicity states.

As described in Sec. 3.3, the polarized electron beam is produced by illuminating circularly polarized photons onto a photocathode. The spin of the photo-emitted electron is correlated to the circular polarization state of the photon, which is either parallel (1 or +) or anti-parallel (0 or -) to the electron momentum direction. These defines the two helicity states of the electron beam.

During the g2p experiment, the helicity pattern was set to be a Quartet, which can either be  $(+ - - +)$  or  $(- + + -)$ . This pattern eliminates the linear background, and minimizes the low frequency systematic uncertainty [65].

#### 3.4.4 Beam Polarization

The beam polarization is measured by the Møller polarimeter which was illustrated in Fig. 3.5 as id 5. The polarimeter uses the process of Møller scattering of  $\bar{e}^- + \bar{e}^- \rightarrow e^- + e^-$  with a ferromagnetic foil magnetized in a magnetic field of about 24 mT as a target of polarized electron [66]. The beam polarization can be obtained from the measured asymmetry:



Table 3.1: Summary of the Møller measurements for g2p experiment [67]

#	date	polarization (%)	Syst.err.
1	03.03.2012	79.91 $\pm$ 0.20	$\pm 1.7\%$
2	03.30.2012	80.43 $\pm$ 0.46	$\pm 1.7\%$
3	03.30.2012	79.89 $\pm$ 0.58	$\pm 1.7\%$
4	04.10.2012	88.52 $\pm$ 0.30	$\pm 1.7\%$
5	04.23.2012	89.72 $\pm$ 0.29	$\pm 1.7\%$
6	05.04.2012	83.47 $\pm$ 0.57	$\pm 1.7\%$
7	05.04.2012	81.82 $\pm$ 0.59	$\pm 1.7\%$
8	05.04.2012	80.40 $\pm$ 0.45	$\pm 1.7\%$
9	05.15.2012	83.59 $\pm$ 0.31	$\pm 1.7\%$

$$P_b = \frac{A_{measured}}{AnPow * P_t}, \quad (3.2)$$

where  $AnPow$  is the analyzing power which depends on the beam position,  $P_t$  is the Mller target polarization. The measured asymmetry  $A_{measured} = \frac{N_+ - N_-}{N_+ + N_-}$ , where  $+/-$  corresponds to the helicity states.

Nine measurements were performed corresponding to different beam energies and beamline configurations during the experiment, as shown in Table 3.1 [67].

#### 3.4.5 Chicane Magnets

The transverse magnetic field in the target region will cause the beam deflected downward when the beam passes the target region. To compensate this effect and have beam straightly incident on the target, two chicane magnets were placed in front of the target to pre-bend the beam upwards (Fig. 3.5, id 7). The first chicane magnet was installed 5.92 m upstream of the target which bend the beam down of the horizontal plane. The second chicane magnet, which was installed 2.66 m upstream of the target, bend the beam upward back to the target. The beam profile is also illustrated in Fig. 3.5.

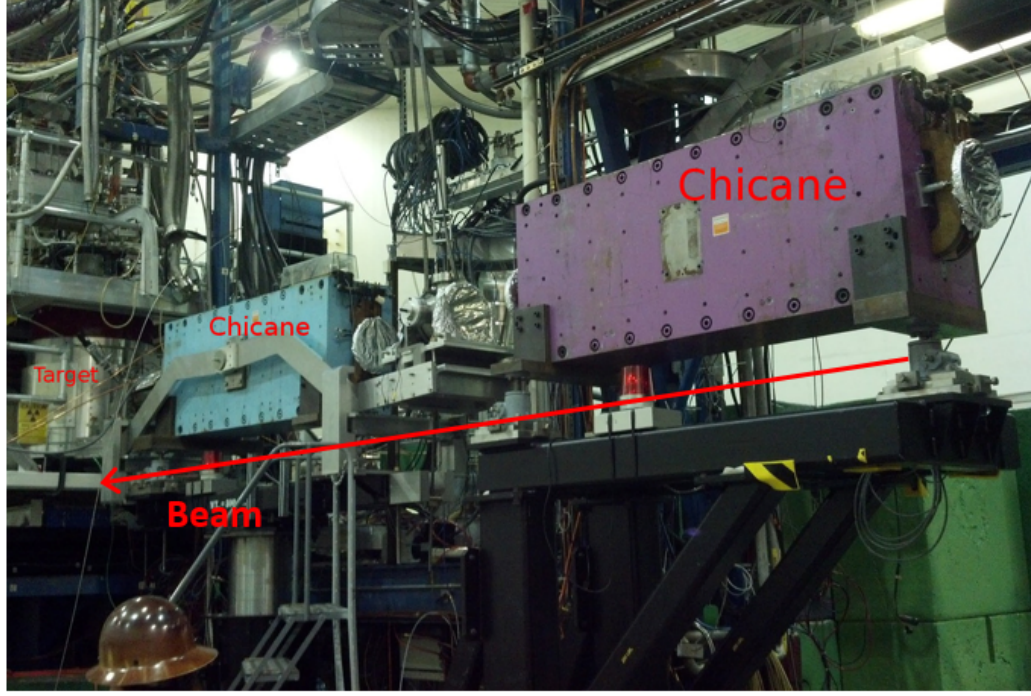


FIGURE 3.7: Chicane dipole magnets upstream of the target.

#### 3.4.6 Local Beam Dump

For the settings with 5 T transverse target field, the chicane magnet cannot bend the beam to the Hall A beam dump. The low beam current for the experiment allow for the use of a local beam dump, which was installed downstream of the  $NH_3$  target and upstream of the septum magnet, as shown in figure 3.8. The local beam dump worked great during the experiment without any high radiation recorded.

### 3.5 The Polarized $NH_3$ Target

In the g2p experiment, a polarized solid  $NH_3$  target was used as an effective polarized proton target. The polarization was achieved through the process of Dynamic Nuclear Polarization (DNP). This process can provide greater than 90% proton polarization in a 5T magnetic field and at around 1K. Since the target magnetic field significantly bends electron trajectories, in order to achieve the low  $Q^2$  region which

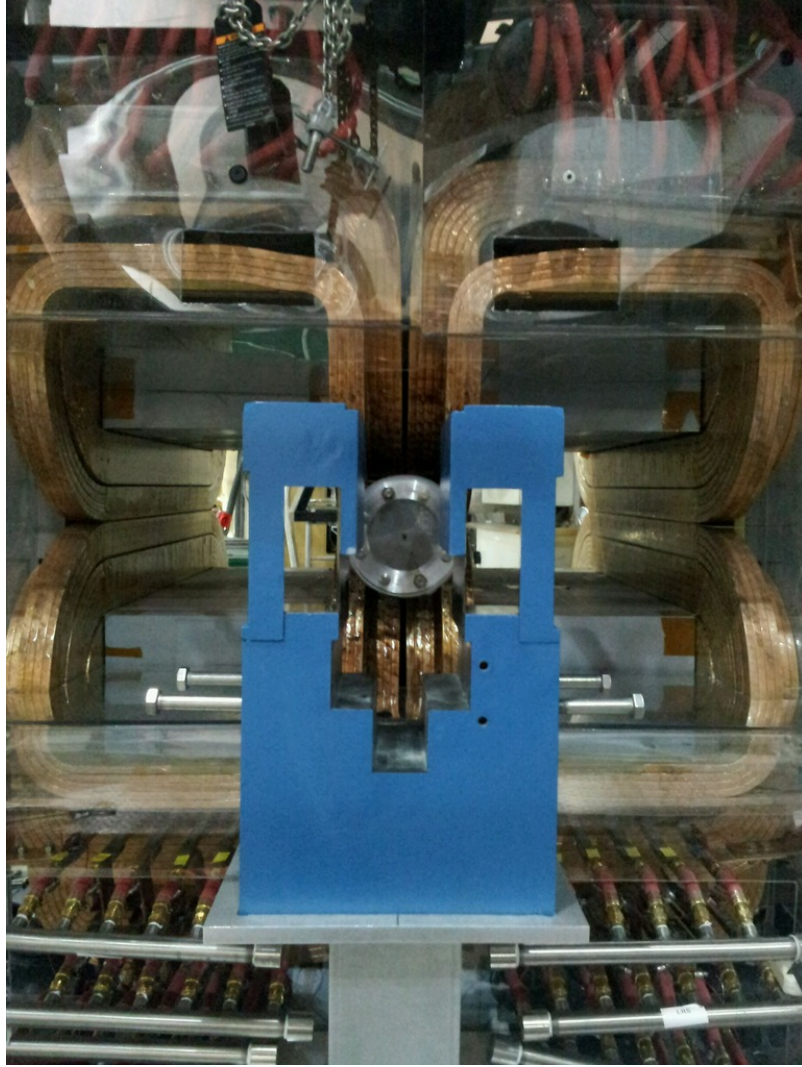


FIGURE 3.8: The local beam dump (blue) positioned in front of the septum magnet (bronze coils).

requires small scattering angle, the target was also operated in a 2.5T field during the experiment. Fig. 3.9 shows the setup of the target.

The operating mechanism to polarize the target is illustrated in Fig. 3.10. The starting point of this mechanism is thermal equilibrium (TE) polarization. By placing the material in a high magnetic field  $B$  and at low temperature  $T$ , according to Boltzmann statistics, the polarization after the material reach thermal equilibrium should be:

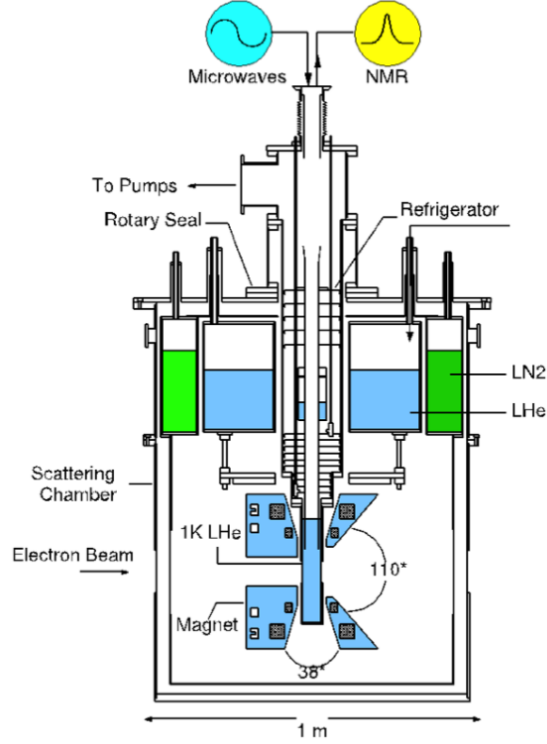


FIGURE 3.9: Setup of the  $\text{NH}_3$  target.

$$P_{TE} = \frac{e^{\frac{\mu B}{kT}} - e^{\frac{-\mu B}{kT}}}{e^{\frac{\mu B}{kT}} + e^{\frac{-\mu B}{kT}}}. \quad (3.3)$$

With 5T field and 1K temperature, Eqn. 3.3 gives polarization around 0.3% for protons, while almost 100% for electrons. This starting point will serve as one calibration point when we measure the polarization with NMR.

DNP is utilized to elevate the polarization of protons via the spin-spin transitions with microwaves [68]. Using microwaves of frequencies corresponding to the energy gaps shown in Fig. 3.10, the spin of the proton and electron can be flipped by transitions between different energy splitting levels. The (down, down) state can be flipped to the (up, up) state with microwaves, and by changing the microwave frequency, the (down, up) state can also be flipped to the (up, down) state. This

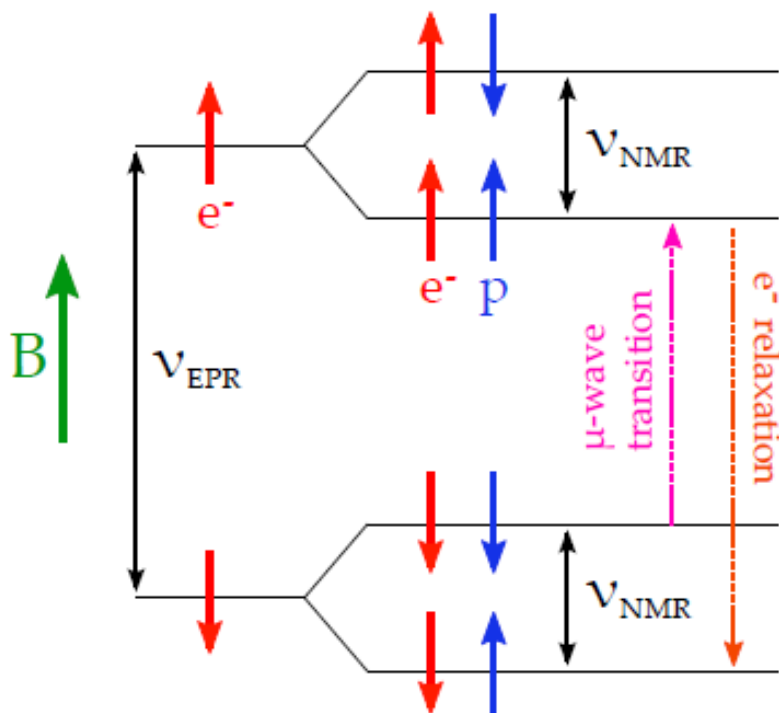


FIGURE 3.10: DNP spin flip transitions of target. Figure is from Ref. [68].

enables us to align protons in different directions without changing the magnetic field. Both positive and negative polarizations can be achieved with the same field. Since the relaxation time of the electrons at 1K is much shorter than that of the protons, the same electron can be used to polarize many protons.

During the g2p experiment, the NMR measurements of the polarization, temperature, timestamp, and various other readings were collected roughly every 30 seconds. The offline polarizations were calculated using Thermal Equilibrium (TE) measurements and the online NMR signals. The target polarization for 5T and 2.5T field settings are shown in Fig. 3.11 [69]. The average polarization is 15% and 70% for 2.5T and 5T settings, respectively. More details about this analysis can be found in [69].

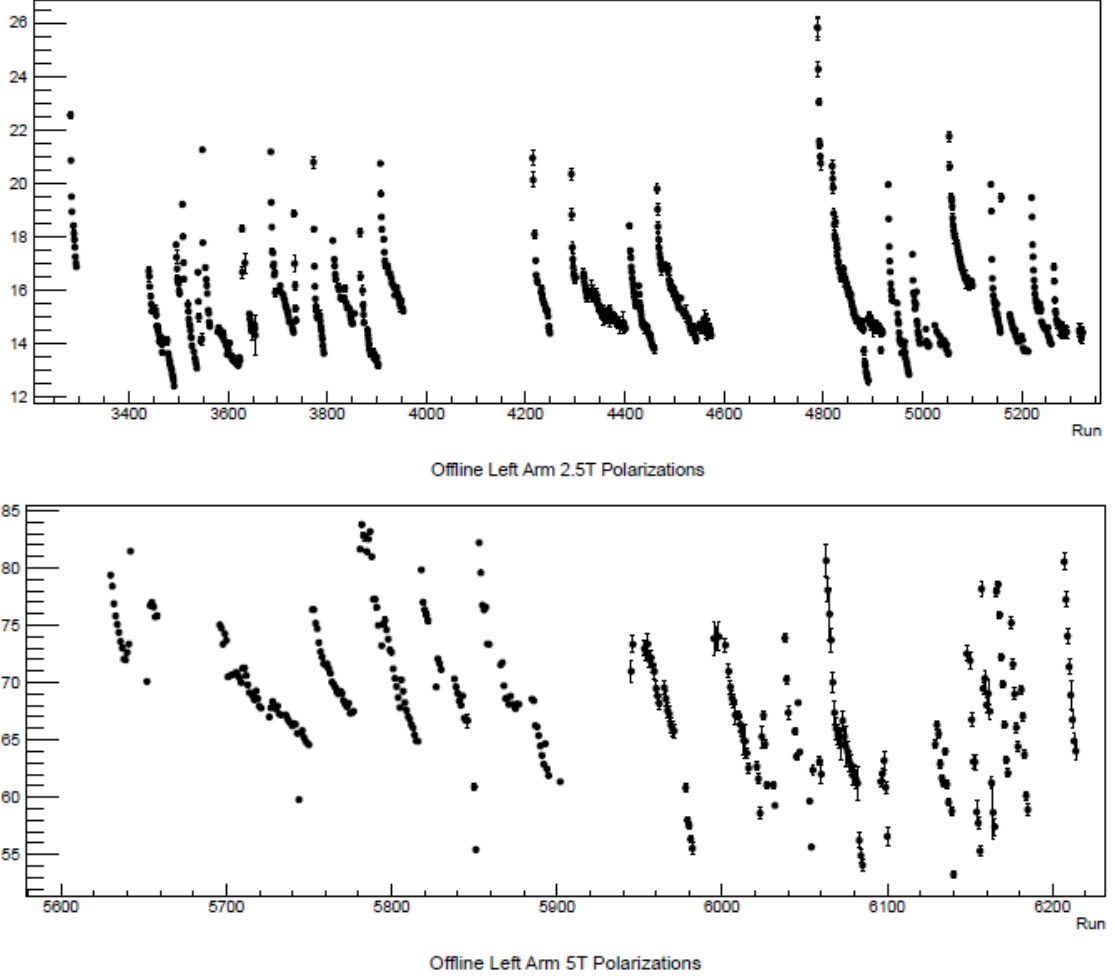


FIGURE 3.11: Target polarization for 2.5T and 5T settings of left HRS [69].

### 3.6 Hall A Spectrometer

Hall A contains two nearly identical high resolution spectrometers (HRS). The E08-027 experiment used these two spectrometers to detect inclusive electrons. Fig. 3.12 illustrates the schematic view of HRS. They will be referred to as LHRS and RHRS from hereon.

Each HRS consists of a pair of quadrupoles, a dipole and a third quadrupole. The dipole bends particles  $45^\circ$  vertically, and provides the momentum resolving power of the spectrometer. The first quadrupole focuses particles in the dispersive (vertical)

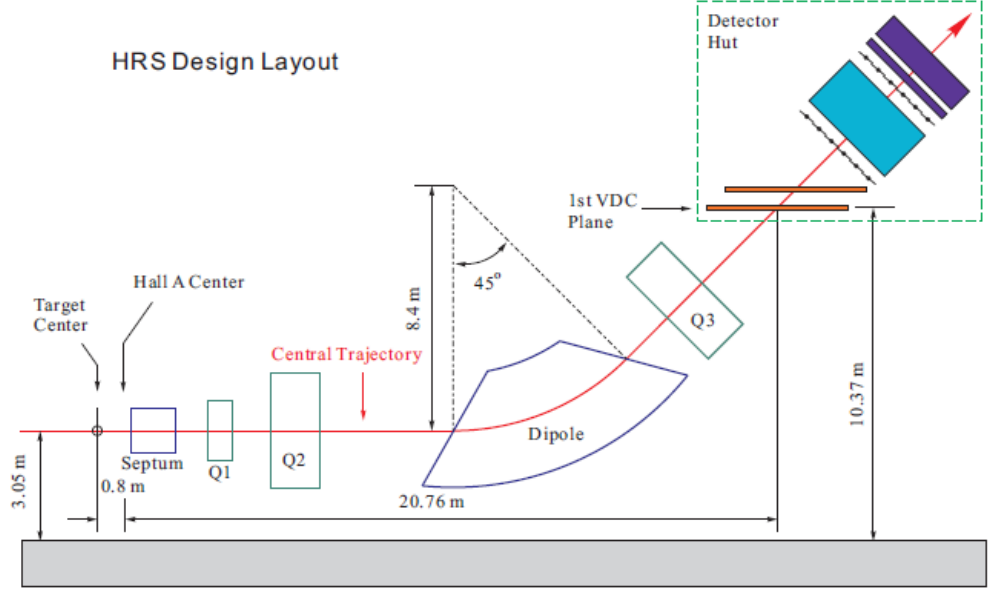


FIGURE 3.12: Schematic of Hall A High Resolution Spectrometer and the detector hut. The figure is from [24].

plane. The second and third quadrupoles are identical and focus particles in the transverse plane. This QQDQ design provides high momentum resolution at the  $10^{-4}$  level, a good position and angular resolution, and a relatively large acceptance in both angle and momentum. The main characteristics are summarized in Table 3.2 [66].

The HRS rotates around the axis in Hall A center pointing up. The minimum achievable angle with respect to the beam direction is  $12.5^\circ$  due to the size of the HRS. This means the HRSs can only detect forward scattered electrons in the angles larger than  $12.5^\circ$ . The E08-027 experiment aims at measuring the proton structure function  $g_2$  in the low  $Q^2$  region ( $0.02 < Q^2 < 0.2 \text{ GeV}^2$ ). To reach the small scattering angle of  $5^\circ$ - $6^\circ$  necessary for this kinematic range, a pair of septum magnets were installed between the target and the HRSs. The details will be presented in Sec. 3.7.

Table 3.2: Main characteristics of the Hall A HRS. The resolution values are FWHM.

Configuration	QQDQ
Bending Angle	45°
Optical Length	24m
Momentum Range	0.3 ~ 4.0 GeV/c
Momentum Acceptance ( $\delta p/p$ )	$\pm 4.5\%$
Resolving Power (D/M)	5.0
Angular Range	6 12.5°
Angular Acceptance (horizontal)	$\pm 25$ mrad
Angular Acceptance (vertical)	$\pm 50$ mrad
Solid Angle at $\delta=0, y_{tg}=0$	4.3 msr
Angular Resolution (horizontal)	1.5 mrad
Angular Resolution (vertical)	4.0 mrad
Transverse Position Resolution	2.5mm

### 3.7 Septum Magnets

A pair of room temperature septum magnets were used in the E08-027 experiment for the first time in Hall A, JLab. The septa were designed to bend electrons with momenta up to 2.8 GeV and angles between 5° and 6° into spectrometers as illustrated in Fig. 3.13.

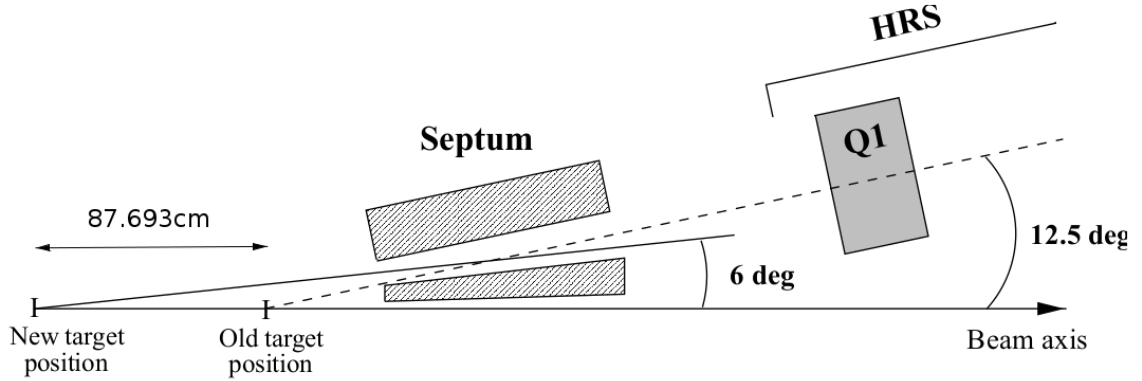


FIGURE 3.13: Schematic of how septum magnet deflects small angle electrons into HRS. Target was moved upstream from the old target position.





FIGURE 3.14: Picture of the pair of septum magnets.

The target was positioned 89.6 cm upstream to accommodate the septum magnets. Fig. 3.14 shows the picture of the pair of septum magnets. They are symmetric on left and right. Each side has three pairs of coils with (48 - 48 - 16) turns on top and (16 - 48 - 48) turns on bottom. These coils are made of  $1 \times 1$  cm square shape copper hollow wires. During the experiment, beam goes through the central pipe, and scattered electrons go through the tunnels to the left and right to be bent into the HRS on each side.

Unfortunately during the experiment, the right septum electrical lead was burned twice, and wires were shorted to iron. After the first and second repairs, the top right septum has (40 - 32 - 16) turns and (40 - 00 - 16) turns, respectively. The coils on the bottom and the left septum coils remain unchanged. However, the field in left

Table 3.3: Production data of the g2p experiment corresponding to different septa configurations.

Septa	Production Data
Good	2.3 GeV, 2.5T, HRS $p_0 = 2.228$ (elastic)
Second (bad)	2.3 GeV, 2.5T
Third (very bad)	1.7 GeV, 2.5 T
	1.2 GeV, 2.5 T
	2.3 GeV, 5 T
	3.4 GeV, 5 T

septum also changed since it was affected by the change in the right septum field. The field in both parts were no longer symmetric after the right septum failures. TOSCA field maps were provided for each case. This situation leads to analysis for each of the septum configurations. Table 3.3 lists the production data distribution in terms of different beam energy and target field combinations and HRS momentum ( $p_0$ ) settings. We can see that most production data were taken with the third (very bad) septum configuration. Calibration data were taken for each configuration for analysis. The physics results shown in chapter 6 analyzed the 1.7 GeV data which were taken under the third septum configuration.

### 3.8 Detector Package

E08-027 utilized elements of the detector package of the spectrometers. This package was designed to characterize particles passing through the spectrometer. Fig. 3.15 illustrates the configuration of the package. A pair of vertical drift chambers (VDCs) provided tracking information of particles (position and angle). A pair of scintillator planes formed triggers to activate the data-acquisition electronics. A gas Cherenkov detector and lead-glass calorimeter enabled the particle identification (PID).

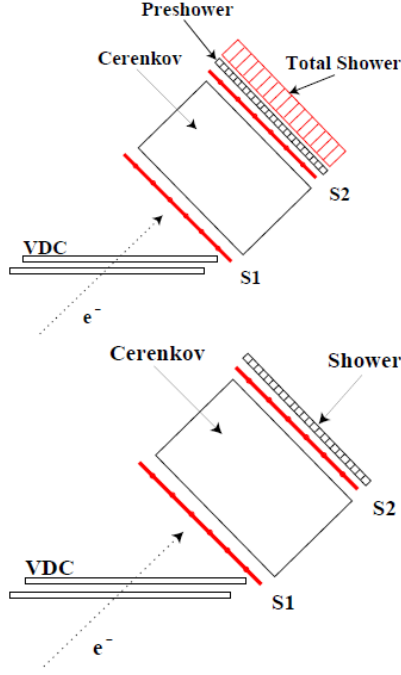


FIGURE 3.15: Detector packages for RHRS (top) and LHRS (bottom). The figure is from [70]

### 3.8.1 Vertical Drift Chamber

Each HRS contains a pair of VDCs after the exit of the third quadrupole. These VDCs provide a precise measurement of the positions and angles of incident charged particles. Fig. 3.15 illustrates the schematic lay-out of the VDCs for one HRS. Each VDC contains two wire planes, which are horizontal in the lab frame. There are 368 sensing wires in each plane, and are orthogonal to each other (see Fig. 3.15). The nominal trajectory traverses the wire planes at an angle of  $45^\circ$ , and the wires in the planes are oriented at an angle of  $45^\circ$  with respect to the dispersive and non-dispersive directions. The two planes are separated by 355 mm. A high voltage of -4.0 kV is held on the cathode planes, and the anode sense wires are grounded. A mixture of argon and ethane gas was used as the medium in the chambers. The argon

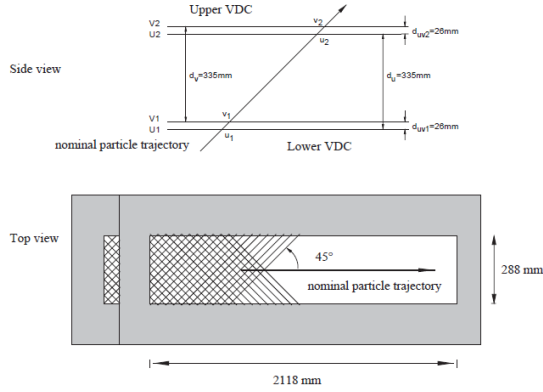


FIGURE 3.16: Vertical Drift Chambers (VDCs). The figure is from [66]

serves as the ionization medium, and the ethane absorbs the produced photons from ionization.

By design, nominal electron trajectory at the angle of  $45^\circ$  will fire five sensing wires per plane. Electrons at extreme angle of  $52^\circ$  will still fire three wires. The hits information is collected by time-to-digital converters (TDCs). From the TDC values and the drift velocity, the trajectory distance for each wire can be determined. The distances versus wire positions are then linearly fit to obtain the cross over point. Two VDC planes allows determination of angle of the trajectory. The typical resolutions of position and angle in VDCs are  $100 \mu\text{m}$  and  $0.5 \text{ mrad}$ , respectively.

### 3.8.2 Scintillators and Trigger Electronics

Two scintillator planes (denoted S1 and S2) were utilized to form the main triggers for E08-027. They are spaced 2 m apart, and each plane contains six overlapping 5mm thick paddles. See Fig. 3.17. Each paddle, made of thin plastic scintillator, is viewed by two photomultipliers (PMTs). The active area of the paddles are  $35.5 \text{ cm} \times 29.3 \text{ cm}$  and  $54.0 \text{ cm} \times 37.0 \text{ cm}$ , respectively. The time resolution of each plane is approximately  $0.30 \text{ ns}$  ( $\sigma$ ).

Triggers are generated by the PMT signals from the scintillator planes, and are

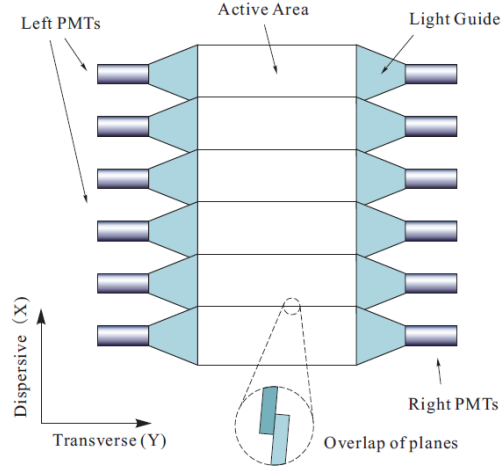


FIGURE 3.17: Lay-out of one scintillator plane. Figure is from [62].

sent to all other detectors and DAQ. Rules were set up to form triggers to select good events for the analysis. An event is considered to be “good event” if it triggers one paddle of both S1 and S2 with two PMTs of each paddle fired. The good events for RHRS and LHRS are called T1 and T3, respectively, and are the main triggers.

In order to measure the trigger efficiency, secondary events are considered. These events trigger one of the scintillator planes and the gas Cherenkov detector. They are called T2 and T4 for RHRS and LHRS, respectively.

In g2p experiment, scattered electrons were detected in both HRS arms, thus we mainly used single arm triggers, T1 - T4. Fig 3.18 illustrates the single arm trigger design. These trigger are counted by scalers and sent to the trigger supervisor (TS). The scalers are helicity gated. TS synchronizes all the detector readouts and sends them to start the data acquisition (DAQ) system.

When the event rate is high, the DAQ system cannot record all the events, and we need to treat the efficiency to obtain physics quantities. Analysis of trigger efficiency will be discussed in Section 5.2.2

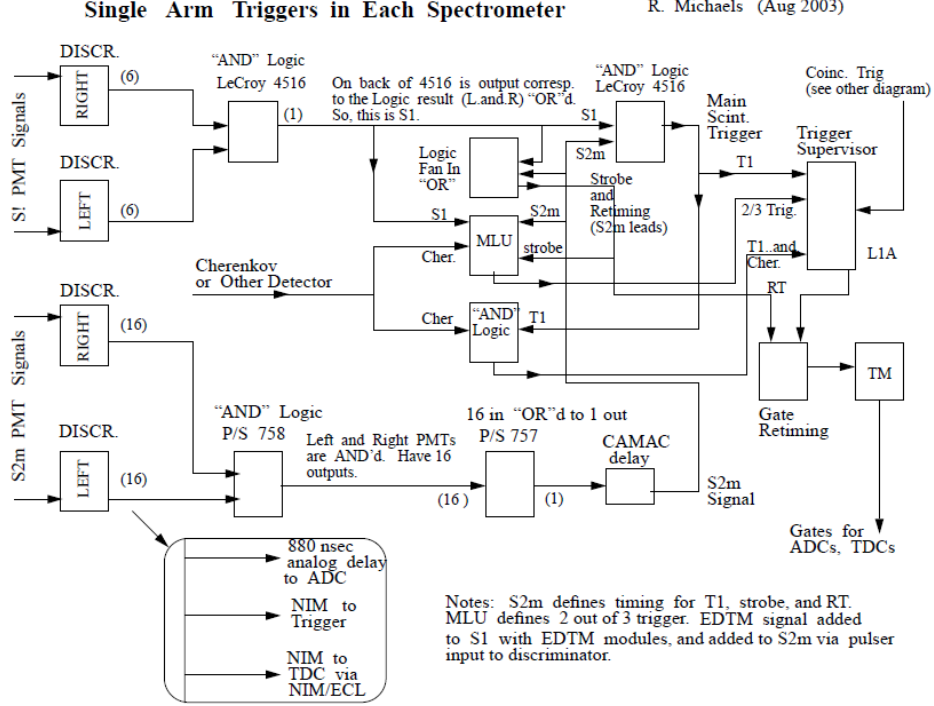


FIGURE 3.18: Single arm trigger design. Figure is from [71].

### 3.8.3 Cherenkov Detectors

E08-027 measures the inclusive electron scattering, thus one of the major tasks of particle detection is to distinguish electrons from background particles, most of which are pions here. PID in E08-027 was accomplished by a gas Cherenkov detector and two layers of lead glass calorimeter.

The Cherenkov radiation is emitted when the velocity of a charged particle passing through transparent material is higher than the velocity of light in the material  $c/n$ . Here  $c$  is the speed of light in vacuum and  $n$  is the refractive index of the material. Then the momentum threshold for a particle of mass  $m$  is

$$p_{th} = \frac{mv}{\sqrt{1 - \frac{v^2}{c^2}}} = \frac{mc}{\sqrt{n^2 - 1}}. \quad (3.4)$$

LHRS and RHRS both possess gas Cherenkov detectors, which mounted between S1 and S2 planes. The Cherenkov tanks are filled with atmospheric pressure  $\text{CO}_2$  gas with an refractive index  $n = 1.00041$  [66]. Therefore, calculated from Eqn. 3.4, the threshold is 18 MeV/c for electron and 4.9 GeV/c for pion. In the designed HRS momentum range  $0.3 \sim 4.0$  GeV/c, electrons will emit Cherenkov radiation, whereas pions will not.

#### 3.8.4 Lead Glass Calorimeter

Lead glass calorimeters were used in experiment E08-027 to improve PID performance in addition to the gas Cherenkov detectors. When a energetic particle passes through lead glass, showers of secondary particles ( $\gamma$ ,  $e^+$ ,  $e^-$ ) will be produced. The signal detected from lead glass calorimeter is linearly proportional to the energy deposited by the incoming particle [72]. For particles of momenta at GeV/c level, electrons will develop electromagnetic showers, whereas hadrons will not due to the longer hadronic mean free path. Thus the energy deposition in the calorimeter can be used to distinguish electrons from pions: high ADC signal for electrons and low ADC signal for hadrons.

Both HRSs contains two layers of lead glass calorimeters, which have different configurations (see Fig. 3.19)[66]. The LHRS is equipped with two identical layers of lead glass (called “pion rejectors”), both of which are perpendicular to the particle trajectories, and composed of 34 lead glass blocks. The RHRS is equipped with a total absorber. The first layer (called “pre-shower”) is perpendicular to the particle trajectories and composed of 48 lead glass blocks, while the second layer (called “shower”) is parallel to the trajectories and composed of 80 lead glass blocks.

Due to different thickness’s of the lead glass blocks, the pre-shower and shower detectors of RHRS provide a better performance than the pion rejectors of LHRS. The PID analysis will be presented in Section 5.2.3.

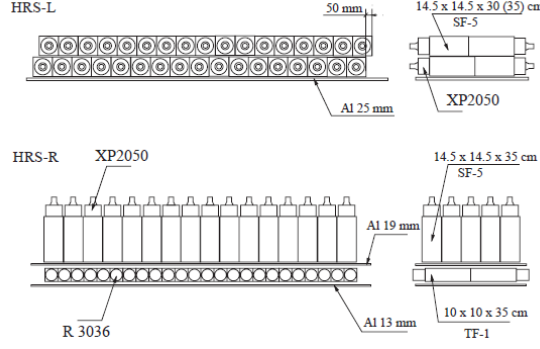


FIGURE 3.19: Schematic lay-out of the calorimeters in LHRs (top) and RHRS (bottom). Reproduced from Ref. [66].

### 3.9 Data Acquisition System

During the g2p experiment, the standard HRS data acquisition (DAQ) system was used to record the detector information. The DAQ system consists of three fastbus crates, one trigger supervisor scaler crate, and one HAPPEX crate for each arm. The setup is illustrated in Fig 3.20. The main trigger and the efficiency trigger were connected to the trigger supervisor after several logic modules and trigger the ADC and TDC in fastbus crate to collect the data from detectors. The trigger supervisor is a device distributes triggers and maintains system busy signals. The charge information from BCM and the trigger count were recorded in scaler.

The CEBAF Online Data Acquisition (CODA) system is a combination of software and hardware packages. The signal outputs of each component of the experiment were collected and processed by the CODA. The recorded data file consists of the following major components:

- Header including a time stamp and run information such as run number, pre-scale factors and event size.
- CODA events from the detectors and the beam helicity signal.



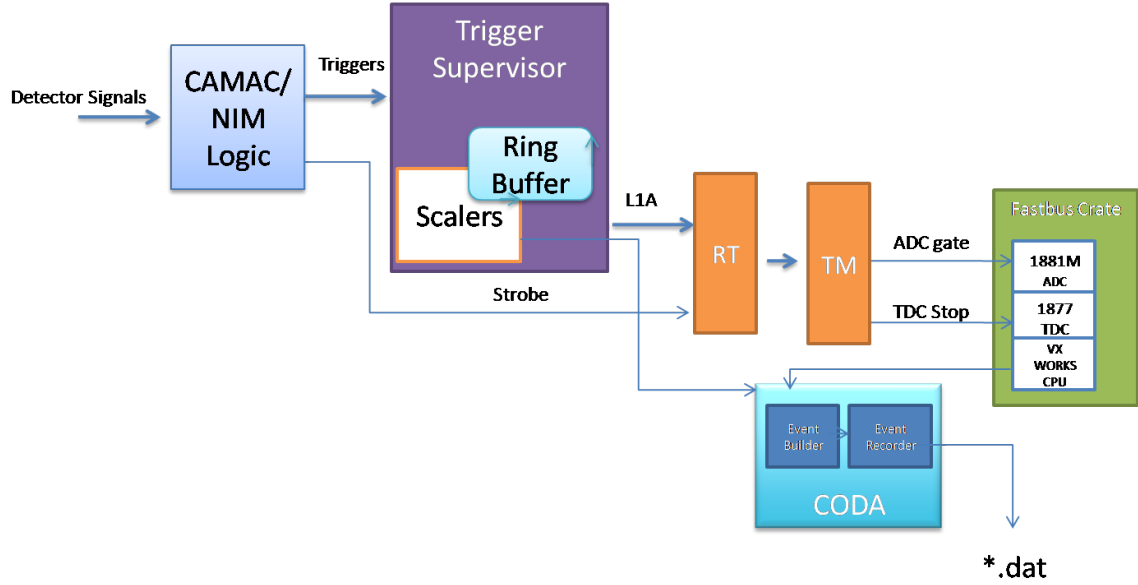


FIGURE 3.20: Schematic of the Hall A DAQ system setup.

- EPICS [73] data from the slow control software used at JLab, which records many characteristics of experimental devices such as spectrometer magnet settings and angles, beam energies, and target temperature.
- CODA scaler events that the DAQ reads every 1 to 4 seconds and feeds them into the main data stream. Since the scaler values are counted by stand-alone units, they are not affected by the DAQ deadtime and can be used to correct DAQ deadtime (see section 5.2.2). Fig. 3.20 shows the schematic of the setup of Hall A DAQ system.

## Optics and Simulation

### 4.1 Overview

The optics optimization procedure aims to reconstruct the target variables at vertex from the focal plane variables recorded by detectors (VDC). The target variables will be used to extract physics results.

The optics here is not the traditional “optics” of mirrors and lenses. It describes the property of the magnet system of the spectrometer in which charged particles travel like light travelling through lenses: they are focused and defocus in different magnets, and eventually focused on the focal plane.

The goal of the optics calibration for the g2p is to obtain good uncertainty of angle reconstruction to obtain precise measurements of cross section and asymmetry. The magnetic field of each component of the spectrometer was configured to take angle resolution as first priority. The addition of the septum magnets and target magnetic field<sup>1</sup> requires a careful study to determine the optical properties of the new system. The optimization is achieved with a set of optics matrices. This chapter will describe

---

<sup>1</sup> A target magnetic field as high as 2.5T was used for the first time in Hall A, JLab.

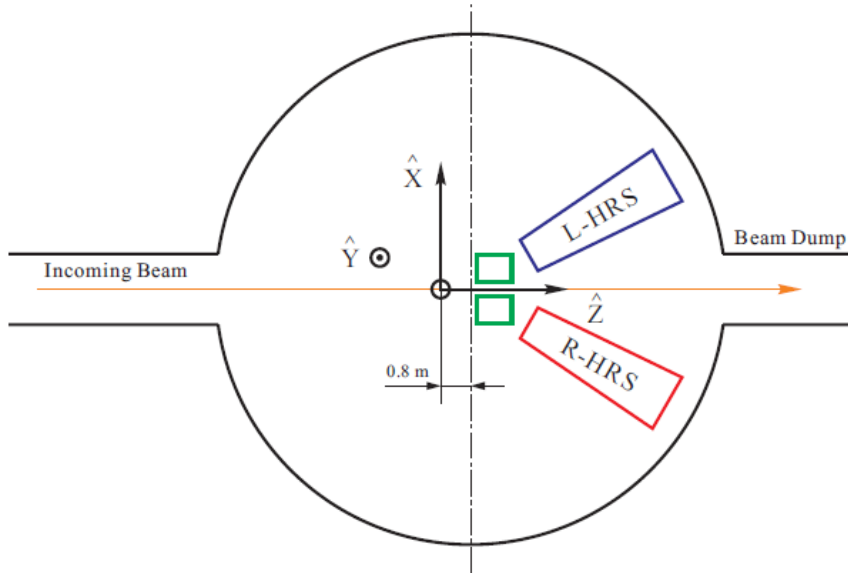


FIGURE 4.1: Hall coordinate system (top view). The figure is from [71].

the procedures to determine the optics matrices.

## 4.2 Coordinate Systems

In this section, a short overview of Hall A target and focal plane coordinate systems will be presented. For a full description refer to Ref. [74]. All coordinate systems presented are Cartesian.

- Hall Coordinate System (HCS).

The origin of the HCS is at the center of the hall.  $\hat{z}$  is along the beamline and in the direction of the beam.  $\hat{x}$  points to the left facing the beam downstream, and  $\hat{y}$  is vertically up (see Fig. 4.1).

- Target Coordinate System (TCS).

In g2p experiment, a septum magnet is bundled with each HRS as a whole system, thus the definition of TCS is slightly different from the standard one. The g2p target was positioned in the upstream about 89 cm away from the hall

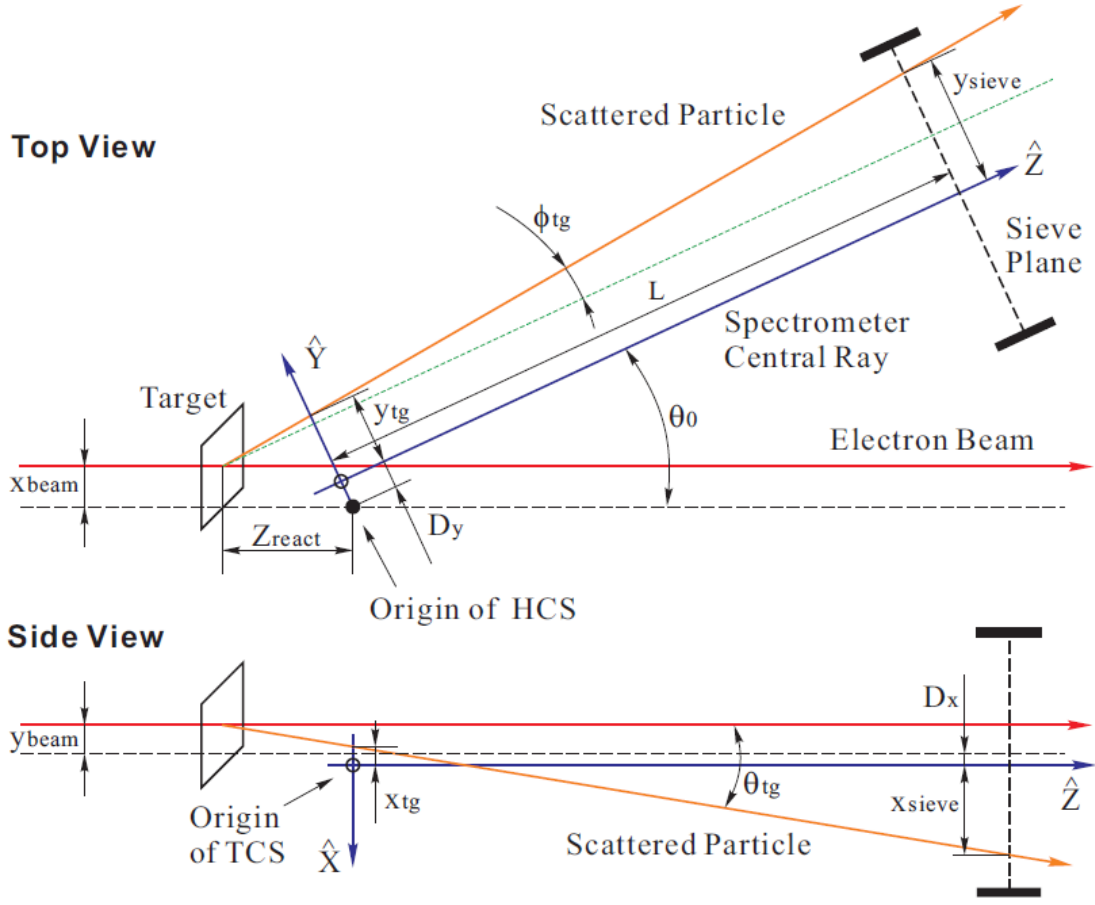


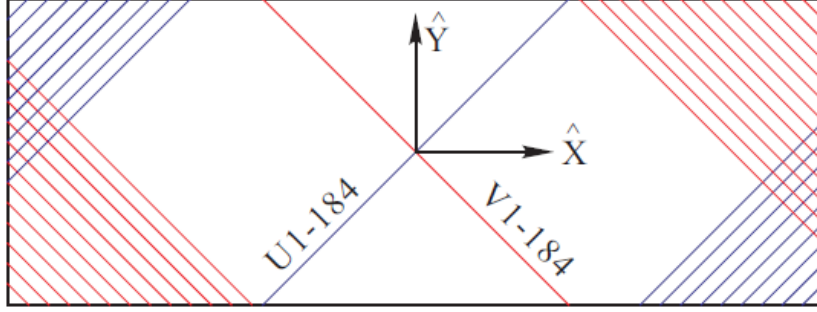
FIGURE 4.2: Target coordinate system for electron scattering off a thin foil target. The figure is from [71].

center because of the septum magnets. The origin of the TCS is at the g2p target center.  $\hat{z}_{tg}$  is defined by a line from target center to the central sieve slit hole in the direction pointing away from target.  $\hat{y}$  points to the left facing the beam downstream, and  $\hat{x}$  is vertically down. Fig. 4.2 illustrates the TCS.  $\theta_{tg}$  is the tangent of the out-of-plane angle in the  $\hat{x}$ - $\hat{z}$  plane.  $\phi_{tg}$  is the tangent of the in-plane angle in the  $\hat{y}$ - $\hat{z}$  plane.

- Detector Coordinate System (DCS).

The intersection of wire 184 of VDC1 U1 plane and the projection of wire

### Top View



### Side View

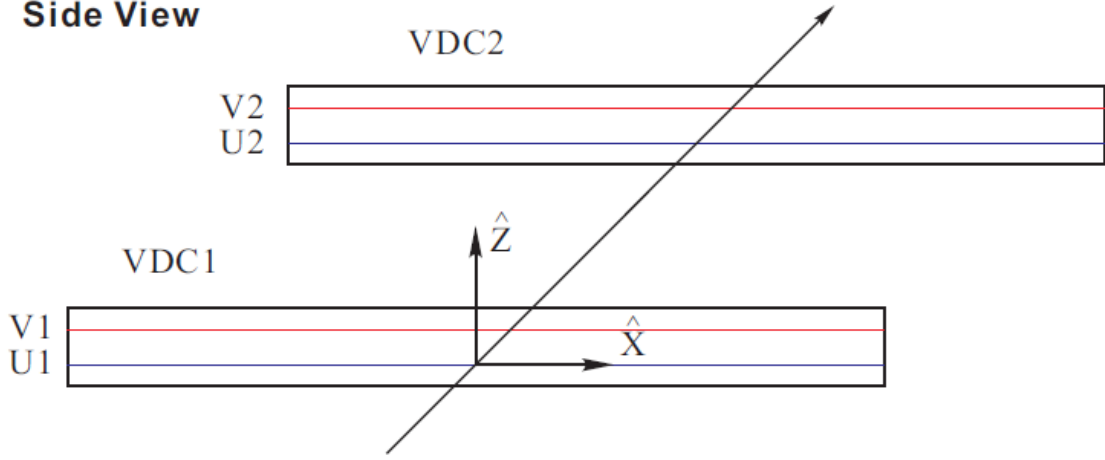


FIGURE 4.3: Detector coordinate system (top and side views). The figure is from [71].

184 of the VDC1 V1 plane onto the U1 plane defines the origin of DCS.  $\hat{z}$  is perpendicular to the VDC1 U1 plane pointing up,  $\hat{x}$  is along the long symmetry axis of VDC1 pointing away from the center of dipole (see Fig. 4.3).

- Transport Coordinate System (TRCS).

Rotating the DCS clockwise around its y-axis by  $45^\circ$  leads to the TRCS at focal plane as illustrated in Fig. 4.4.

- Focal plane Coordinate System (FCS).

This is the coordinate system we use to do optics analysis. HRS was configured

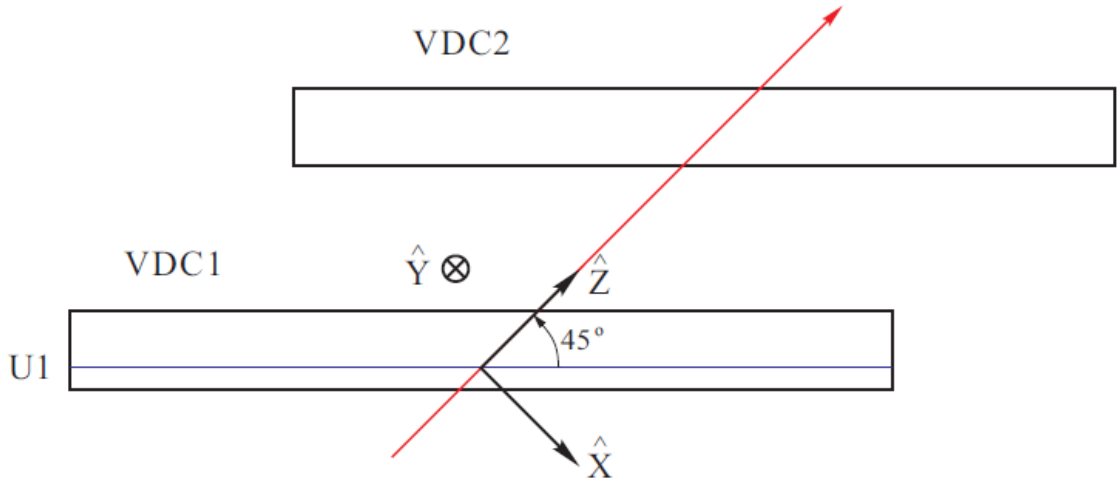


FIGURE 4.4: Transport coordinate system. The figure is from [71].

that particles from different target angles with same momentum will be focused at the focal plane. Therefore, if we define the relative momentum to the central momentum of the spectrometer as

$$\delta = \frac{p - p_0}{p_0}, \quad (4.1)$$

this factor approximately only depends on  $x_{tra}$  and  $p_0$ . FCS is generated by rotating the DCS around its y-axis by a varying angle  $\rho$  so that the new  $\hat{z}$  axis is parallel to the local central ray which has scattering angle  $\theta_{tg} = \phi_{tg} = 0$  (see Fig. 4.5). In this rotated coordinate system, the dispersive angle  $\theta_{fp}$  is small all over the focal plane, and symmetric with  $\theta_{fp} = 0$ . This will make the reconstruction process converge faster during the optics calibrations.

### 4.3 Experimental Setup and Techniques

#### 4.3.1 Introduction

Fig. 4.6 shows the Hall A setup to detect scattered electrons. After the reaction, scattered electrons go through a sieve slit, enter septum and are bent into the HRS,

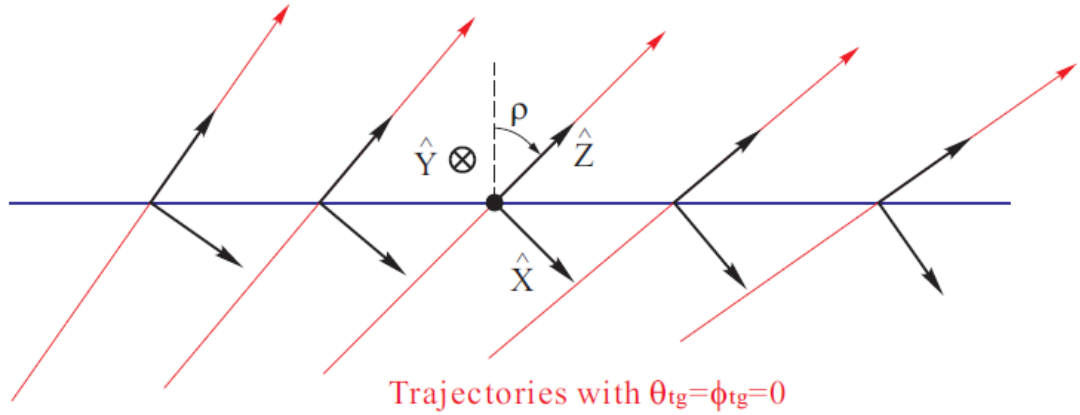


FIGURE 4.5: Rotated focal plane coordinate system. The figure is from [71].

and are finally detected in VDC (first plane denoted as focal plane). Fig. 4.7 shows the scattered electrons going from target foil to sieve slit. Fig. 3.13 shows the septum magnets bend  $6^\circ$  electrons into  $12.5^\circ$  HRSs.

The target used in g2p experiment to take optics data is a thin carbon foil (40 mil or 125 mil). The sieve slit is used to provide calibration information of the angles of scattered electrons. The design is shown in Fig. 4.8. The sieve has 49 holes in a  $7 \times 7$  grid pattern. Two holes are larger than the others to determine the orientation of the images at focal plane. The slit was positioned in a way that the larger hole not in the center was up and away from the beamline. Column A is closest to the beamline. Different from the standard sieve slit, the four columns closest to the beamline are spaced closer than the next three columns. This is designed to coordinate with the higher event rate on the side closer to the beamline due to the smaller scattering angle. The vertical spacings are uniform. The design report is included in Appendix.

#### 4.3.2 Data Acquired

The optimization procedure is performed on a set of data that covers the entire acceptance of the spectrometer in  $\delta$ ,  $\theta_{tg}$ ,  $\phi_{tg}$  and  $y_{tg}$ . The physics process used here

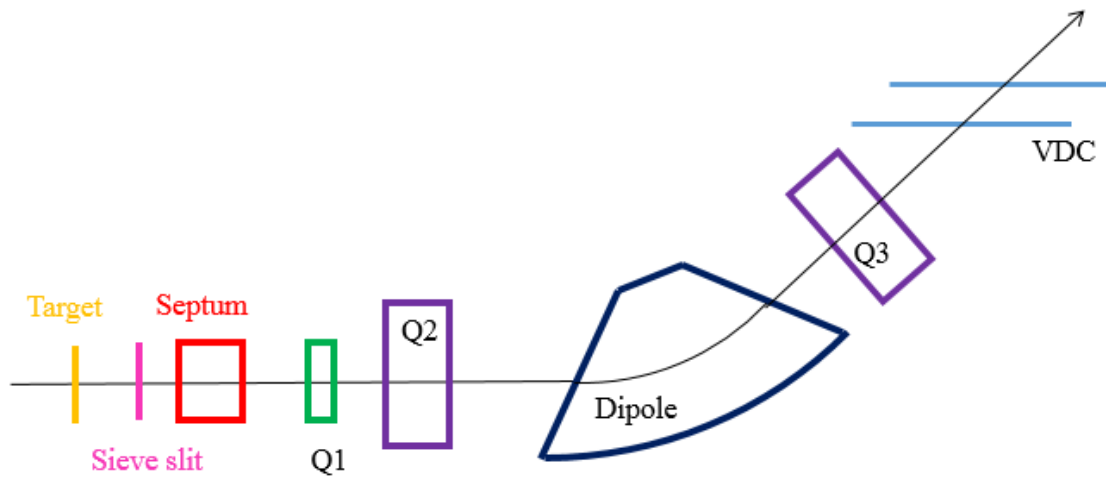


FIGURE 4.6: Hall A optics setup to detector and reconstruct scattered electrons (side view).

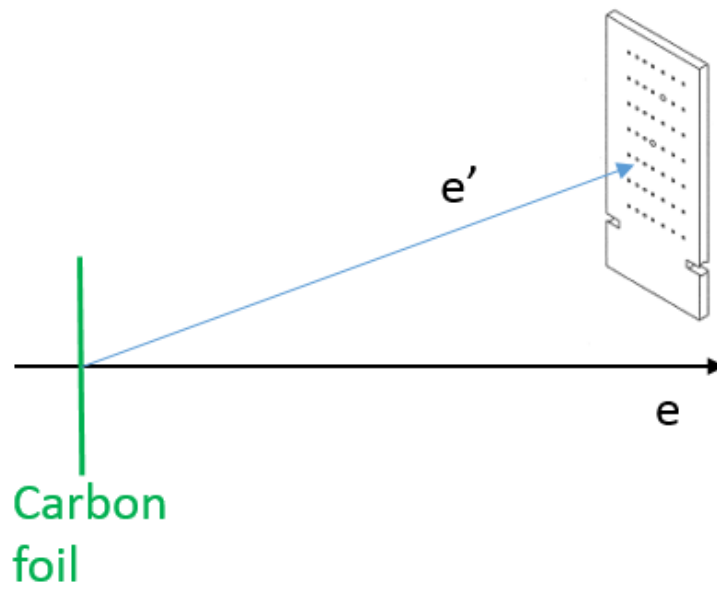


FIGURE 4.7: An illustration of how optics data was taken (side view).



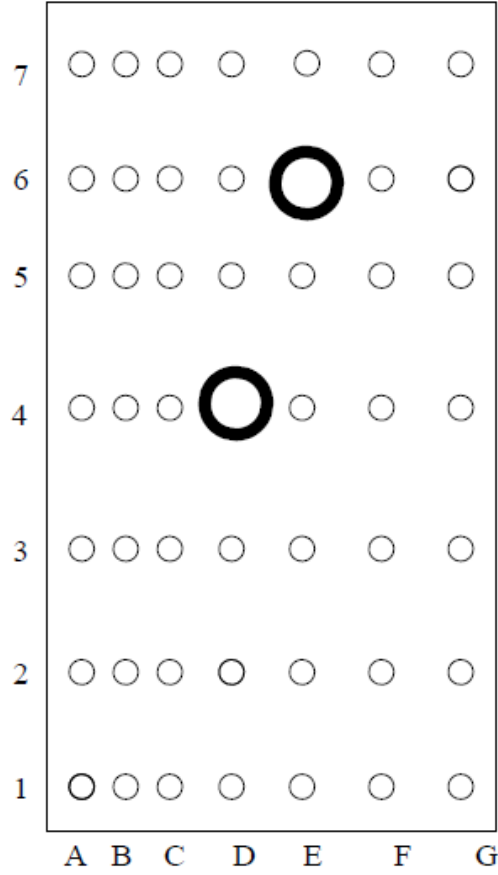


FIGURE 4.8: The design of the sieve slit used during the g2p experiment. The column A is closest to the beamline.

is electron elastic scattering off carbon foil target. The data acquired includes:

- A five or seven steps delta scan, which moved the spectrometer momentum so that the  $^{12}\text{C}$  elastic peak covered  $\pm 3\%$  or  $\pm 4\%$  spectrometer momentum acceptance.
- A set of beam position scan of both vertical and horizontal shifts. The horizontal scan is taken to cover  $y_{tg}$  acceptance. This set of data was acquired instead of standard multi-foils method because g2p production data target  $\text{NH}_3$  is short, around 3cm. The vertex will not be good enough to differentiate

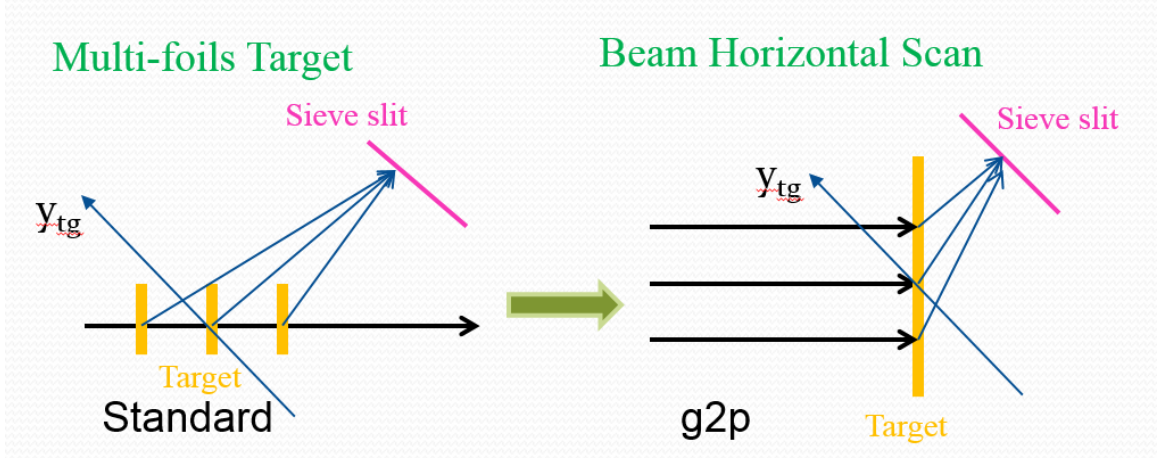


FIGURE 4.9: An illustration of how horizontal beam scan runs cover the  $y_{tg}$  acceptance in the similar way as multi-foils method. (top view).

multi-foils if they are placed within this range. These two methods are illustrated in Fig. 4.9 to show that they both cover the  $y_{tg}$  acceptance. The vertical scan was taken to provide vertical correction information.

- Above data are all taken with sieve slit collimator placed between target and the septum magnets to provide angle calibration information.

These sets of data were acquired for each beam energy and target field configuration. In addition, to determine the position of the target foil, and position for sieve holes, survey reports were provided with precise knowledge of the target position, septum position, and the position of the sieve slit center. Appendix B shows the survey reports.

In the optics for the g2p experiment, the new and most challenging part is how to treat the strong transverse target field. Our strategy is to separate the reconstruction into two parts. The first part includes septum magnet and HRS, and is assumed to be presented by the matrix without target field, which reconstructs focal plane data to target plane. Since septum field and HRS field are proportional to the central momentum, the optical property does not change when the electron momentum

setting changes. However, because of the broken septum magnet, the configuration changed during the experiment. Therefore, the matrix needs to be re-calibrated for each configuration. The second part uses ray-tracing method to treat the target region with field map. A Monte-Carlo simulation program (section 4.7) is developed to facilitate the calibration. Details will be described in the following sections.

#### 4.4 Optics without Target Field

The optics matrix elements connect the focal plane and target coordinates. For each event, two spatial coordinates ( $x_{fp}$  and  $y_{fp}$ ) and two angular coordinates ( $\theta_{fp}$  and  $\phi_{fp}$ ) are measured at the focal plane detectors. The position of the particle and the tangent of the angle made by its momentum along the dispersive direction are denoted as  $x_{fp}$  and  $\theta_{fp}$ , while  $y_{fp}$  and  $\phi_{fp}$  represent the position and angle in the transverse direction. The focal plane observables are used to calculate  $\delta$ ,  $\theta_{tg}$ ,  $\phi_{tg}$  and  $y_{tg}$  via the optics matrix. The first order approximation without the septa and target field is

$$\begin{bmatrix} \delta \\ \theta \\ y \\ \phi \end{bmatrix}_{tg} = \begin{bmatrix} \langle \delta | x \rangle & \langle \delta | \theta \rangle & 0 & 0 \\ \langle \theta | x \rangle & \langle \theta | \theta \rangle & 0 & 0 \\ 0 & 0 & \langle y | y \rangle & \langle y | \phi \rangle \\ 0 & 0 & \langle \phi | y \rangle & \langle \phi | \phi \rangle \end{bmatrix} \begin{bmatrix} x \\ \theta \\ y \\ \phi \end{bmatrix}_{fp} \quad (4.2)$$

The mid-plane symmetry shown in Eq. 4.2 is broken with the addition of the septum magnet, and the full matrix (Eq. 4.3) was optimized for the g2p experiment.

$$\begin{bmatrix} \delta \\ \theta \\ y \\ \phi \end{bmatrix}_{tg} = \begin{bmatrix} \langle \delta|x \rangle & \langle \delta|\theta \rangle & \langle \delta|y \rangle & \langle \delta|\phi \rangle \\ \langle \theta|x \rangle & \langle \theta|\theta \rangle & \langle \theta|y \rangle & \langle \theta|\phi \rangle \\ \langle y|x \rangle & \langle y|\theta \rangle & \langle y|y \rangle & \langle y|\phi \rangle \\ \langle \phi|x \rangle & \langle \phi|\theta \rangle & \langle \phi|y \rangle & \langle \phi|\phi \rangle \end{bmatrix} \begin{bmatrix} x \\ \theta \\ y \\ \phi \end{bmatrix}_{fp} \quad (4.3)$$

Each of the target variables can be expressed as polynomials of focal plane variables. For example,  $\theta_{tg}$  is written as

$$\theta_{tg} = \sum_{j,k,l} T_{jkl} \theta_{fp}^j y_{fp}^k \phi_{fp}^l \quad (4.4)$$

$$T_{jkl} = \sum_i C_i x_{fp}^i \quad (4.5)$$

where  $C_i$  are the optics matrix elements for the corresponding polynomial terms. Similar expressions are used for  $\phi_{tg}$ ,  $y_{tg}$  and  $\delta$ .

#### 4.4.1 Calibration Procedure

The optics calibration requires data sets for which the optics variables are known at both the target plane and focal plane. The matrix elements are determined by minimizing  $\chi^2$ :

$\chi^2 = \sum_{event} (\text{reconstructed variable} - \text{nominal variable calculated from survey})^2$ , where variable represents  $\theta_{tg}$ ,  $\phi_{tg}$ ,  $y_{tg}$  or  $\delta$ . Each target variable is fitted independently, except for the vertex, i.e.  $y_{tg}$  calibration, which also depends on a good reconstruction of horizontal angle  $\phi_{tg}$ . The calibration procedures are as following:

- The angular calibration used the elastic scattering on the carbon foil target with sieve slit inserted as shown in Fig. 4.7. All delta scan runs are used to cover the full momentum acceptance. The sieve slit is a 0.2 inch-thick

tungsten plate. Electrons lose energy passing through the tungsten. However, it is possible that the higher energy scattered electrons passing through the tungsten, though lose a fraction of their energies, can still reach the detector and mix with lower energy inelastic electrons. Thus, only the detected carbon elastic scattering events are selected for the calibration to ensure the data sample events are all coming from sieve holes. Each selected event corresponds to one of the holes on the sieve slit. The locations of the target and sieve slit were surveyed, and then the actual angle of the trajectories can be calculated, since the trajectories from target to sieve slit are straight lines.

- The momentum calibration used the same data sample as the angular calibration. The full momentum acceptance was scanned by changing the HRS central momentum  $p_0$  around the carbon elastic peak, i.e.  $\delta$  scan at  $p_0 = p_{elastic}, \pm 1\%, \pm 2\%$ , etc. The nominal momentum value is calculated using elastic scattering formula with known beam energy, the scattering angle and collision energy loss in the target material.

The optics optimization routine was updated with new features:

- Event selection steps were improved to select cleaner data samples. Standard procedure consists of cut on the focal plane to avoid junk events, cut on each sieve hole, and a  $\delta$  cut for the entire run to select the elastic events. The  $\delta$  cut was improved to be performed on each sieve hole, so that no events from materials other than carbon will be mixed in the data sample.
- The number of events chosen in each hole can be different and controlled by an configuration input file. This makes the optimization more flexible.

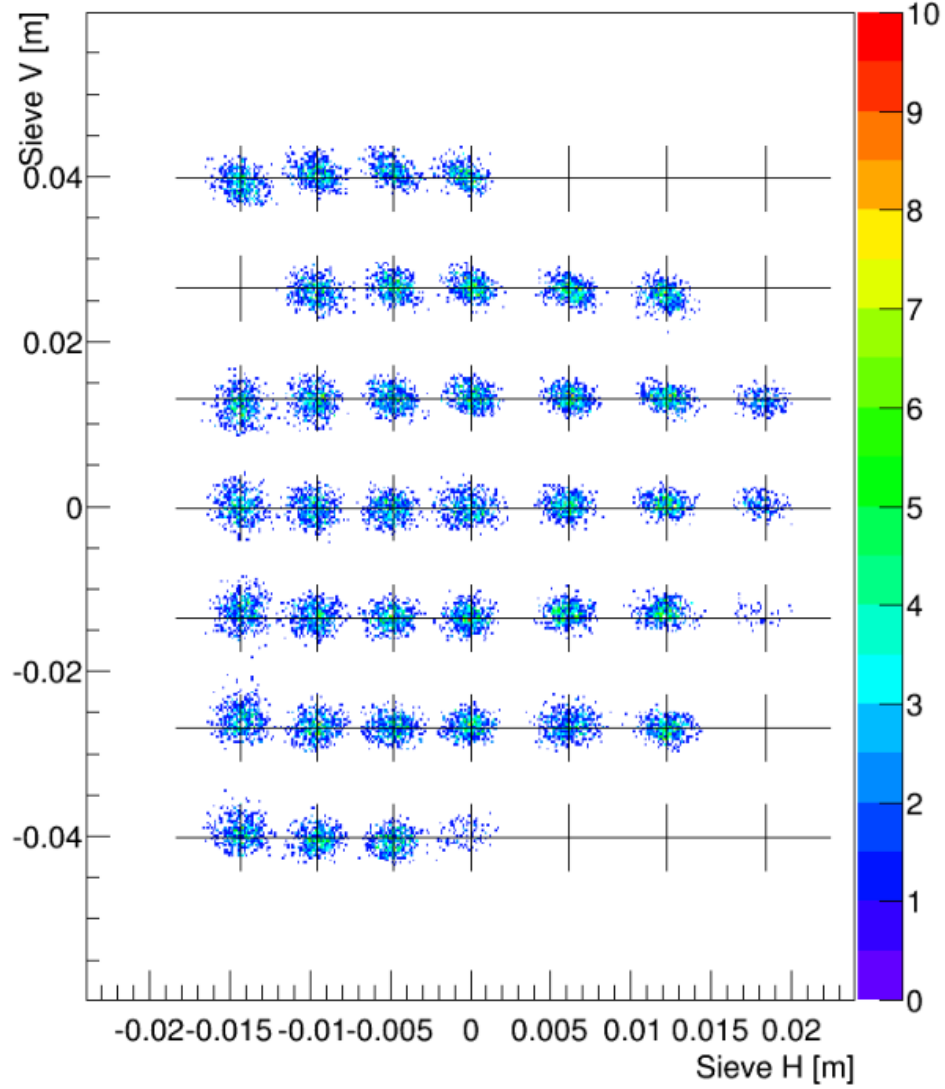


FIGURE 4.10: Optics reconstructed sieve slit pattern. The vertex trajectories are projected on the sieve plane. The black crosses illustrate the sieve hole positions.

#### 4.4.2 Results and Performances

The reconstruction results of  $\theta_{tg}$  and  $\phi_{tg}$  are shown in Fig. 4.10. The trajectories are projected on the sieve slit plane. The black crosses are the positions of the sieve holes. All the  $\delta$  scan runs are drawn together. Fig. 4.11 shows the momentum reconstruction results. The resolution of the results of the optics without target field are close to the nominal performance of the HRS system [74] as listed in Table 4.1.

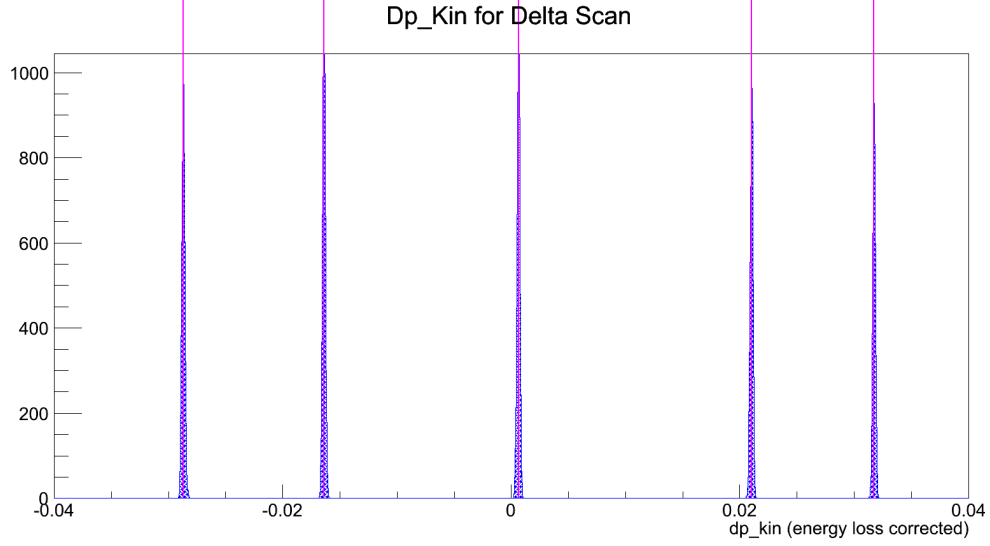


FIGURE 4.11: Optics momentum reconstructed results for five  $\delta$  scan runs. The pink lines represent the calculated nominal values of the momenta. The purple distributions are reconstructed data, which are well optimized.

Table 4.1: Performance summary of RMS values for optics study without target field.

RMS	LHRS	RHRS	Nominal performance [74]
$\delta$	$1.3 \times 10^{-4}$	$2.0 \times 10^{-4}$	$1.1 \times 10^{-4}$
$\theta$	1.5 mrad	1.6 mrad	2.5 mrad
$\phi$	0.9 mrad	0.9 mrad	0.8 mrad

## 4.5 Optics with Target Field

### 4.5.1 Calibration Approach

For each configuration of different target field and beam energy, optics matrix was calibrated. The calibration started with the matrix from the calibration of optics data without target field, which provided the starting point of polynomials and coefficients.

As shown in Fig. 4.12, with inputs of the reaction vertex and the geometries of the sieve hole, the simulation program is used to select electron trajectories that

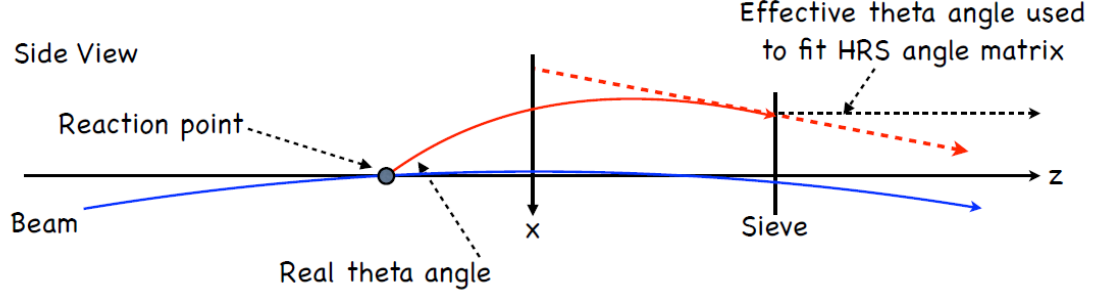


FIGURE 4.12: Method to do optics optimization with target field drifting.

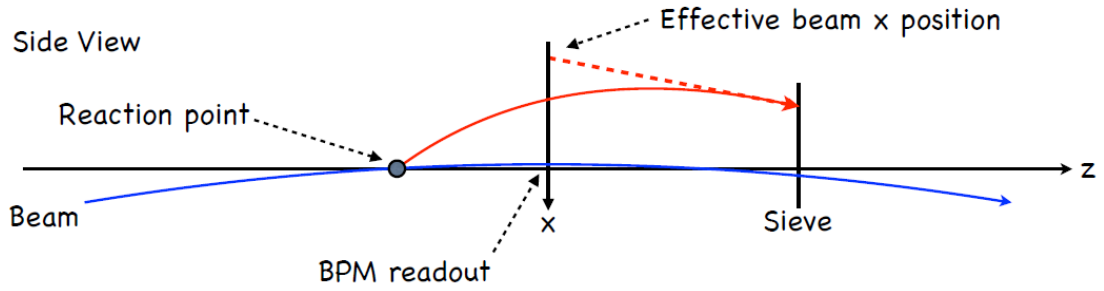


FIGURE 4.13: Reconstruction of scattering angles with optics calibration.

pass through the sieve slit holes. The effective  $\theta$  and  $\phi$  of these trajectories at sieve plane serve as reference for optics matrix calibration without target field described in section 4.4.

When the optics matrix is used to reconstruct the scattering angle and momentum in production runs, the procedure is shown in Fig. 4.13. The matrix is used to obtain the effective variables at target plane. Since the electron trajectory between the target plane and sieve plane is a straight line if there is no target field. The effective variables at target can be traced back to obtain the variables at the sieve plane. Then the simulation program traces the trajectories from sieve plane back to the target plane in the target field, and the variables can be obtained there.



Table 4.2: Uncertainties of survey measurements and target position determination

sieve x,y	0.5mm
sieve z	1mm
target z	1.5mm

#### 4.5.2 Calibration Results

Calibration results of 1.7 GeV beam energy and 2.5 T transverse target field configuration are shown in Fig. 4.14 and Fig. 4.15. Fig. 4.14 shows the reconstructed sieve slit pattern. All the  $\delta$  scan runs are drawn together. Fig. 4.15 shows the momentum reconstruction results for each delta scan run of the same setting. Uncertainties better than  $5 \times 10^{-4}$  is achieved.

### 4.6 Central Scattering Angle Measurements

Scattering angle is the angle between the direction of a scattered electron and the direction of electron beam. Scattering angle measurement contains two parts: central scattering angle  $\theta_0$  and spectrometer (optics) reconstruction angles ( $\theta_{tg}$ ,  $\phi_{tg}$ ). The central scattering angle ( $\theta_0$ ) is defined as the angle between the line connecting target center and sieve slit center and the ideal beam line.  $\theta_{tg}$  and  $\phi_{tg}$  are defined with respect to the  $\theta_0$ . The relation between scattering angle ( $\theta$ ) and  $\theta_0$  and target angles ( $\theta_{tg}$  and  $\phi_{tg}$ ) is <sup>2</sup>

$$\theta = \arccos \frac{\cos(\theta_0) - \phi_{tg} \sin(\theta_0)}{\sqrt{1 + \theta_{tg}^2 + \phi_{tg}^2}} \quad (4.6)$$

#### 4.6.1 Survey

A survey measures the position of sieve slit and target center as shown in Appendix B. The uncertainties of the survey measurements are shown in Table. 4.2

---

<sup>2</sup> This equation is valid in the condition that beam incident angle is zero.

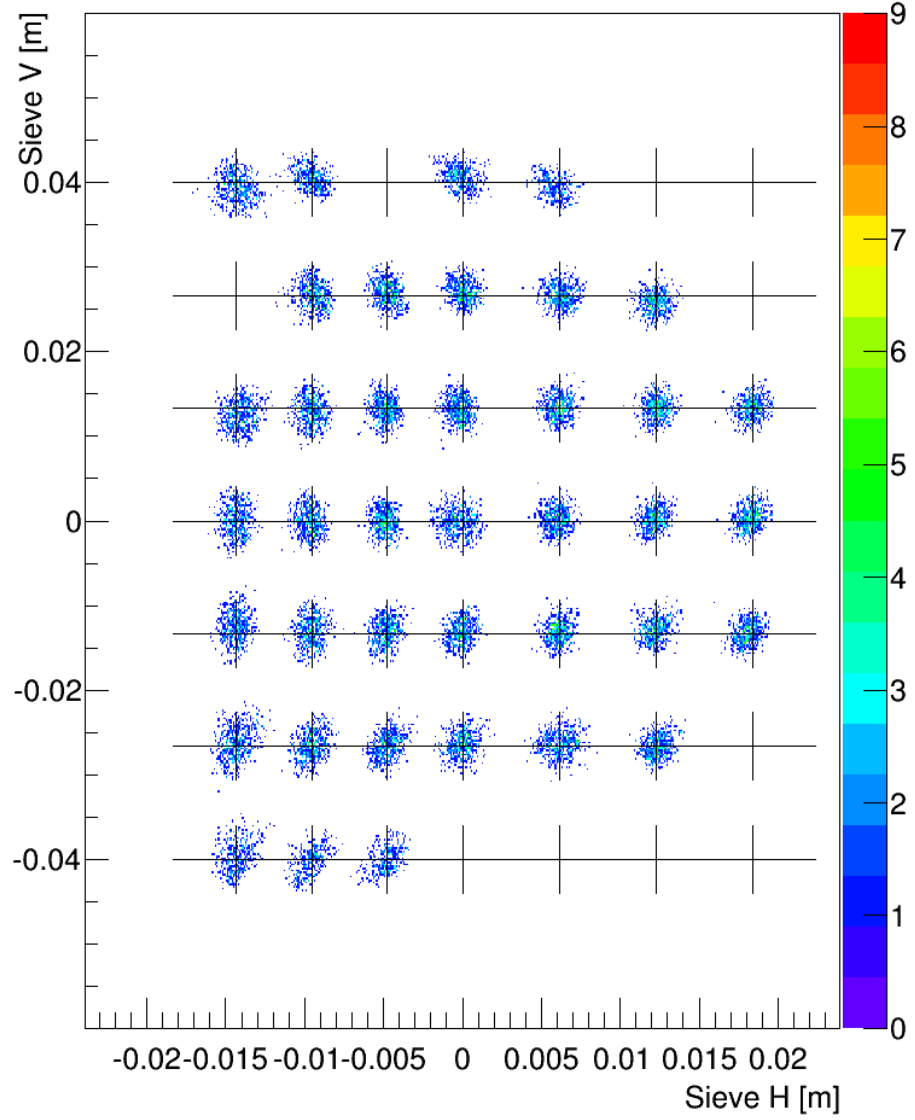


FIGURE 4.14: Optics reconstructed sieve slit pattern for 1.7 GeV beam energy and 2.5 T transverse target field configuration. The vertex trajectories are projected on the sieve plane. Black crosses illustrate the sieve hole positions.

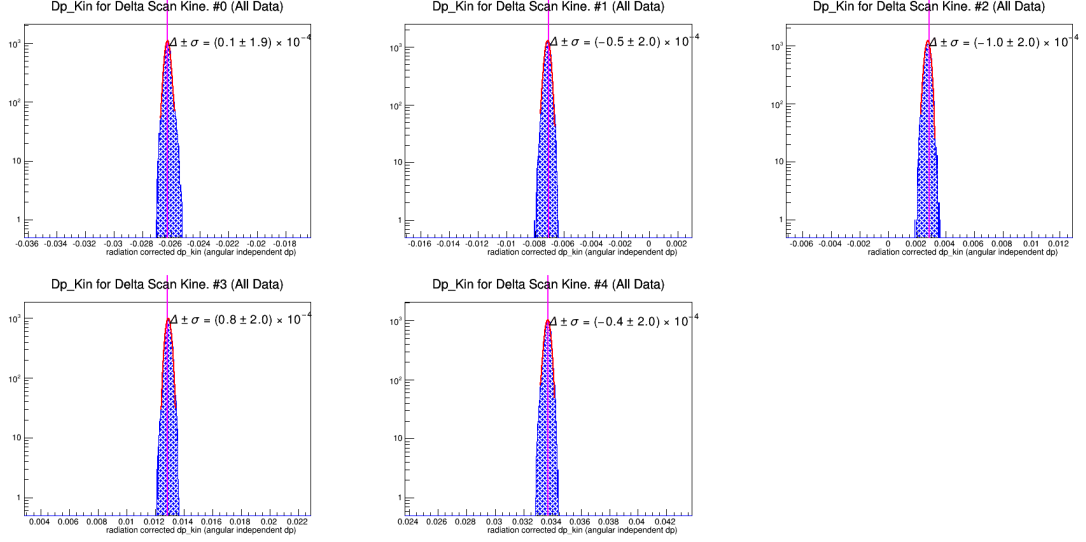


FIGURE 4.15: Optics momentum reconstruction results for 1.7 GeV beam energy and 2.5 T transverse target field configuration. The pink lines represent the calculated nominal values of the momenta. The purple distributions are reconstructed data. The peaks of data distributions were fit, and the fitting results are shown as the uncertainty of the center  $\pm$  the resolution of the peak.

Table 4.3: Survey results of central scattering angle

Arm	Survey values (rad)
LHRS	$0.1007 \pm 0.0007$
RHRS	$0.1009 \pm 0.0007$

The uncertainties from these measurements lead to the uncertainty of the survey angle as 0.7 mrad. The values and uncertainties of center angles for LHRS and RHRS are listed in Table. 4.3.

#### 4.6.2 Pointing Measurement

Pointing measurement is a method to determine the central scattering angle using elastic scattering. The equation for elastic scattering off a target of mass  $M$  is

$$E' = \frac{E - E_{loss}}{1 + \frac{E - E_{loss}}{M}(1 - \cos \theta)} - E'_{loss}, \quad (4.7)$$

where  $E$ ,  $E'$ ,  $\theta$  and  $E_{loss}$  represent beam energy, scattered electron energy, scattering angle, and energy loss respectively. Since  $M$  is known, by accurately measuring  $E$  and  $E'$ ,  $\theta$  could be calculated.

The uncertainty of this calculation will be reduced by using the difference of  $E'$  between two nuclei, as shown in Eqn. 4.8.  $\Delta E'$  can be determined with higher accuracy than  $E'$ . In most cases, these two nuclei are in the same target, such as  $\text{CH}_2$  foil or water cell target, where  $E_{loss}$ 's cancel out, and also reduce the uncertainty.

$$\Delta E' = E'_1 - E'_2 = \frac{E - E_{1loss}}{1 + \frac{E - E_{1loss}}{M_1}(1 - \cos \theta)} - \frac{E - E_{2loss}}{1 + \frac{E - E_{2loss}}{M_2}(1 - \cos \theta)} - (E'_{1loss} - E'_{2loss}). \quad (4.8)$$

In the g2p experiment, carbon foil in Liquid Helium and  $\text{CH}_2$  foil targets were used for different configurations to have two nuclei. Pointing measurements were performed with central momentum settings of HRS to reduce the uncertainties. In the process of determining the central scattering angle  $\theta_0$ , only events going through the central sieve slit hole were selected. Fig. 4.16 shows the double elastic peaks from the run with the carbon foil in liquid helium. The left peak is helium elastic peak, and right one is from carbon.  $\Delta E'$  can be obtained from the fitting of these two peaks.

Before looking into the calculation, the g2p experiment has a special situation. The electron beam in g2p has an offset from the nominal beamline, which is changing frequently over the period of the experiment. The beam position has an uncertainty of about 1.5mm, which is an order larger than the standard situations in the previous experiments in Hall A at Jefferson Lab. An illustration of the situation is shown in Fig. 4.17.

Fig. 4.17 shows the schematic of central angle measurement with  $\text{CH}_2$  foil target. The electron beam deviates from nominal beamline by  $x_b$ , and scatters on the target

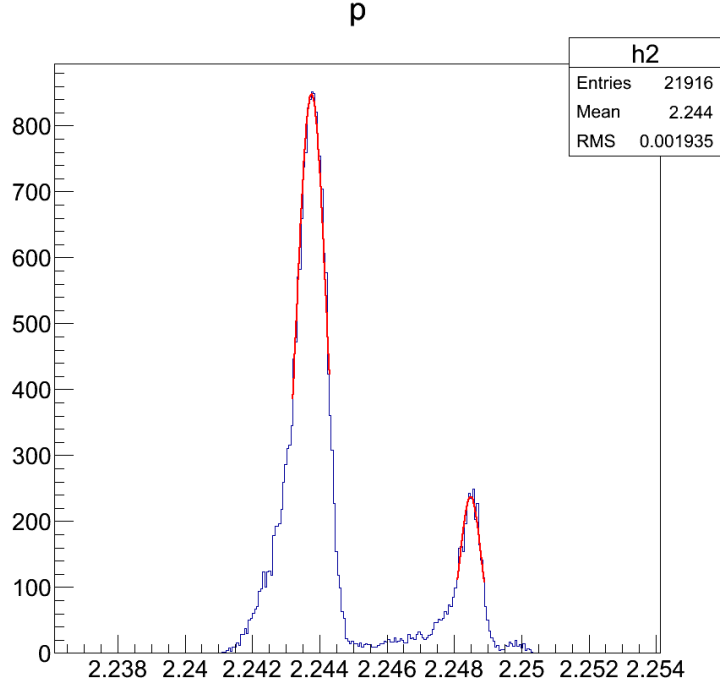


FIGURE 4.16: Double elastic peaks from carbon and helium.

with incoming angle  $\theta_b$ . The distance of the sieve slit center from the target center is  $x$  and  $z$  in Hall coordinate system. The scattering angle of electron is  $\theta$ , while the central scattering angle is  $\theta_0$ . This figure shows that the pointing calculation will determine  $\theta$ , and the relation between  $\theta$  and  $\theta_0$  need to be determined to obtain  $\theta_0$ .

A Monte Carlo simulation was developed to find out the uncertainty of this relation. Besides the uncertainty of  $x_b$  1.5 mm as mentioned above, uncertainties of other variables were used as shown in Table 4.2. Events are generated under Gaussian distribution around the reaction point. Sieve slit center position was also smeared by both the survey position uncertainty and sieve hole dimension. Then two relation options,  $\theta - \theta_0$  and  $\theta/\theta_0$ , are formed as in Figure 4.18. The uncertainties of these relations are 1.8 mrad and 18.3 mrad, respectively. They are both larger than the uncertainty of the survey results. Studies have also been performed to change the uncertainty of the beam position. The results show that if the beam uncertainty

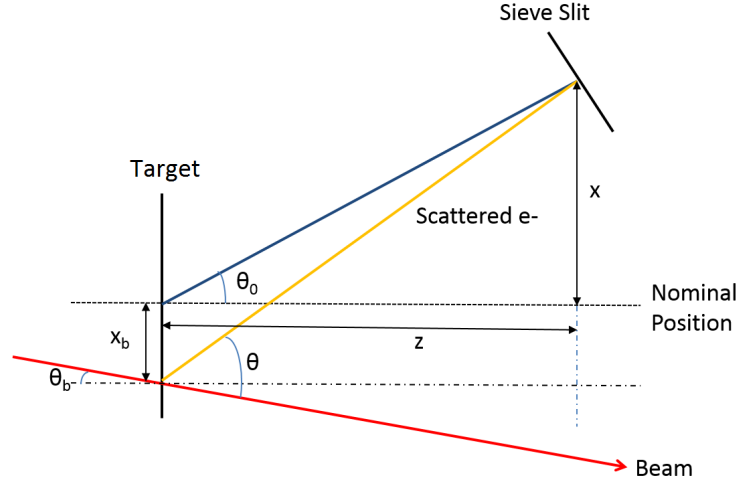


FIGURE 4.17: Schematic of the pointing measurement with beam off center.

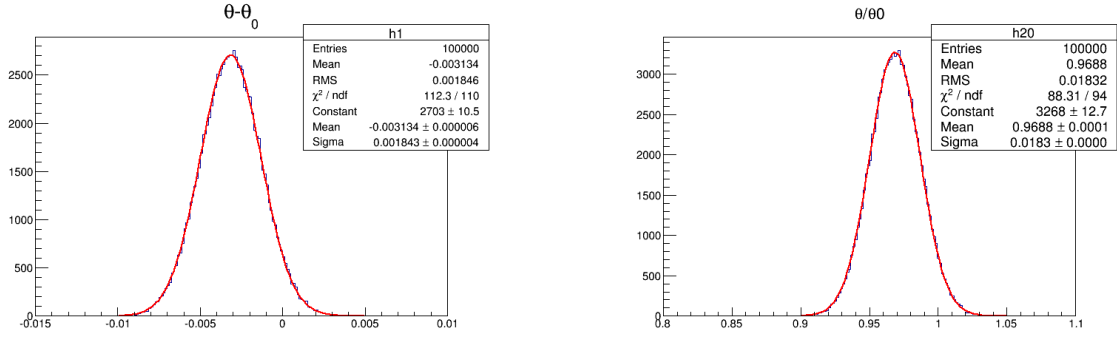


FIGURE 4.18: Uncertainty of  $\theta - \theta_0$  (left) and  $\theta/\theta_0$  (right) from MC simulation.

reduces to 0.5 mm, the angle difference uncertainty reduces to 0.6 mrad, which is smaller than the uncertainty of survey.

#### 4.6.3 Conclusion

Fig. 4.19 shows the results of central angle measurements from LHRS. Left point and right triangle represent results from pointing and survey, respectively. They are consistent within uncertainties. In the current level of beam position and incoming angle uncertainties, survey provides more accurate results of the central scattering angle. The results are shown in Table 4.3.

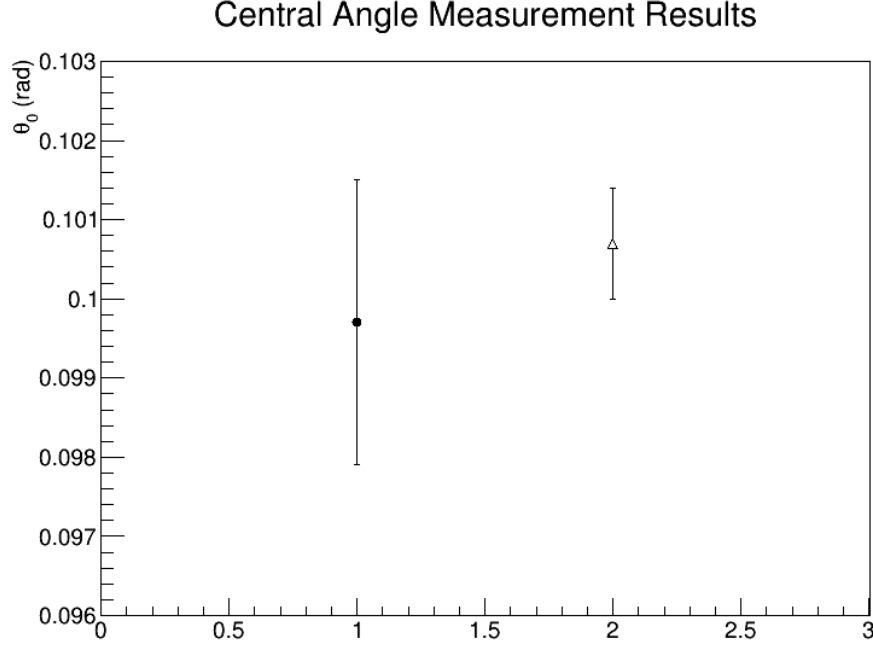


FIGURE 4.19: Central angle measurement results. Left point and right triangle represent results from pointing and survey, respectively. They are consistent within uncertainties.

## 4.7 Simulation

### 4.7.1 Snake Simulation

Snake is a simulation program to trace the electron trajectories from target, through the spectrometer, to the focal plane. This program utilizes the Runge-Kutta method to trace the trajectories through a series of boxes. Each box corresponds to a component of the spectrometer (QQDQ) or the overlapping region, and contains the corresponding magnetic field. The field configurations are either from the built-in models of the program, such as dipole, quadrupole, multipole-multipole overlapping fringe field, or from field map files generated in the format Snake requires. For g2p experiment, the septum configuration was added by using a field map file. Since the target for the g2p experiment was positioned upstream of the old target position to make space for the septum magnets, the configuration was reorganized before

running the program. In the boxes, a series of “endplanes” are defined. Snake transports electrons from endplane to endplane and records trajectory information at each endplane.

The magnetic field strength of each magnet was tuned before the experiment to satisfy the optics goal of the g2p experiment, which is small uncertainty of angle (Sec. 4.1). In the meantime, the tuning still needs to maintain the point to point spectrometer focusing property, which means trajectories starting at same position with different angles will end up be focused at the same position on the focal plane. This tuning also needs to make sure the resolving power of the spectrometer is large enough. The resolving power indicates the resolution of electron trajectories detected on the focal plane of different momenta. The tuned configuration was set into the hardware control system and used for the experiment running.

With the information recorded at the target plane (vertex) and focal plane (detector), trajectories were recorded as output files. A reconstruction matrix from focal plane to target plane was generated based on the fit of the trajectory output. This matrix served as the initial matrix for online replay of data and further optics calibration. On the first day of optics data taking, we saw definite sieve pattern on the online results (see Fig. 4.20), which proved the tuning and initial matrix were good enough for the optics data taking and offline calibrations.

With the information recorded at each endplane, transport functions can be fitted between two endplanes. These functions will be used in Monte-Carlo simulation programs so that the ray-tracing process does not need to be run every time. The forward and reverse functions between target plane and focal plane are obtained to transport the electron trajectories back and forth in the simulation. In order to study acceptance, forward transport functions are fit between target plane and a series of endplanes in each component along the trajectory. Geometric apertures of each endplane are modelled in Snake configuration to reflect the real apertures of the septa



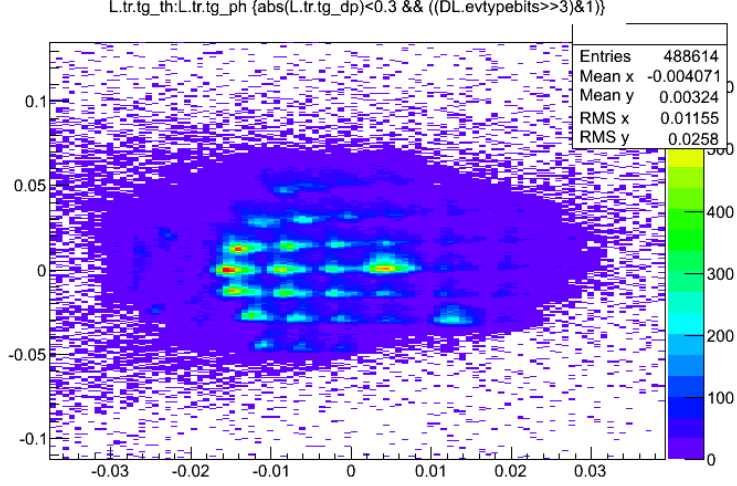


FIGURE 4.20: First optics online result, which proved further optics calibration is possible.

and HRS components. In Snake, a number of events are generated at the target plane in a acceptance range wider than the actual range, and usually two endplanes that block the most events in each component are chosen to be the acceptance endplanes. In the end, about 10 transport functions are obtained to depict the acceptance. The forward transport functions are expressed as polynomials of target plane variables. For example,  $\theta_f$  is written as:

$$\theta_f = \sum_{i,j,k,l,m} F_{ijklm} x_{tg}^i \theta_{tg}^j y_{tg}^k \phi_{tg}^l \delta_{tg}^m, \quad (4.9)$$

where  $F_{ijklm}$  are constants. Similarly the reverse transport function are expressed as polynomials of focal plane variables. For example,  $\theta_f$  is written as:

$$\theta_{tg} = \sum_{i,j,k,l,m} R_{ijklm} x_{fp}^i \theta_{fp}^j y_{fp}^k \phi_{fp}^l \delta_{fp}^m, \quad (4.10)$$

where  $R_{ijklm}$  are constants.

Since septa configuration changed during the experiment, transport functions were generated corresponding to the good septa and the third septa (most production

data) configurations. Work on the second septa configuration is underway.

#### *4.7.2 g2p Simulation*

A Monte-Carlo simulation package `g2psim` was developed to simulate the entire physics process of this experiment. This program consists of the target region ray-tracing, transport functions from Snake, cross section models, and energy loss and radiation processes.

For the target region, this program uses a target field map to ray-trace the electron trajectories, which is developed using an optimized Runge-Kutta method with self-adjusting step length to improve the speed and accuracy. The trajectories in septum magnet and HRS follow the forward and reverse transport functions described in Sec. 4.7.1. The forward transport functions to different planes of septum and HRS components together with the aperture cuts define which event can reach the detector. Tags are recorded to indicate which plane stops the event. An overall flag is recorded to indicate whether the event is successfully transported through a model of septum and HRS. The geometry of a sieve slit plane was also built to study the optics run processes.

The Monte-Carlo generates events uniformly distributed in  $(x, y, z, \delta, \theta, \phi)$  at target plane. The particles are then transported through the target, septum, and HRS, and reconstructed back to target plane. The events passing through the system can then be weighted by the calculated cross section to represent the physics events. This program facilitates the study of optics calibration and acceptance with target field.

# 5

## Data Analysis

In experiment E08-027 (g2p), asymmetry were measured for polarized electron scattering off polarized  $\text{NH}_3$  (effective polarized proton) target. This chapter will present an overview of the analysis of proton inelastic asymmetry. Detector calibrations and particle identification (PID) will be reviewed. Correction to the physics data will also be discussed.

### 5.1 Physics Analysis Overview

The g2p experiment aims at measuring the spin structure function  $g_2^p$  at low  $Q^2$  region. The most intuitive way to measure  $g_2$  is to measure the transverse and parallel cross section differences in Eq. 1.26 and 1.27. The cross section measurements are complicated by the need to understand the acceptance, while the acceptance cancels in the asymmetry. An alternative way is to measure asymmetries and use the world unpolarized data to predict the cross section. The unpolarized cross section is defined as the average of the cross sections of electron beam helicity state  $+$  and  $-$  as expressed in Eq. 5.1 [11]. Then, the polarized cross section differences can be

formed as the product of the asymmetries and cross sections in Eq. 5.2.

$$\sigma_{unpol} = \frac{1}{2} \left( \frac{d^2\sigma^{\Rightarrow}}{d\Omega dE'} + \frac{d^2\sigma^{\Leftarrow}}{d\Omega dE'} \right) = \frac{1}{2} \left( \frac{d^2\sigma^{\rightarrow\uparrow}}{d\Omega dE'} - \frac{d^2\sigma^{\leftarrow\uparrow}}{d\Omega dE'} \right) \quad (5.1)$$

$$\Delta\sigma_{\parallel,\perp} = 2A_{\parallel,\perp} \cdot \sigma_{unpol}. \quad (5.2)$$

The g2p experiment was performed to take the transverse data, and measure either the asymmetry or do the full cross section analysis. While the transverse data dominates  $g_2$ , the parallel data input will be from the Eg4 experiment in Hall B, JLab. The analysis of this thesis is limited to the asymmetry analysis, and utilize the world data model for the unpolarized cross section to form the transverse cross section difference. The parallel cross section difference is also obtained from model. The details will be described in Chapter 6. The physics results of this thesis will focus on the configuration of 1.7 GeV beam energy and 2.5 T transverse target field. The kinematic coverage is illustrated in Fig. 3.1.

## 5.2 Detector Calibrations and Efficiencies

The detectors efficiencies and trigger livetime are studied for the asymmetry measurements. These studies aim to optimize detector cuts to distinguish good electrons from background events. The background events are mostly negatively charged pions. The detectors under the studies include VDCs, scintillators, gas Cherenkov, and calorimeters.

### 5.2.1 VDC Multi-track Efficiency

A good electron event used in asymmetry analysis should have only one track in the VDC, however multi-track events happen when several particles simultaneously pass through the VDC. This can also happen due to noisy wires. For certain kinematic

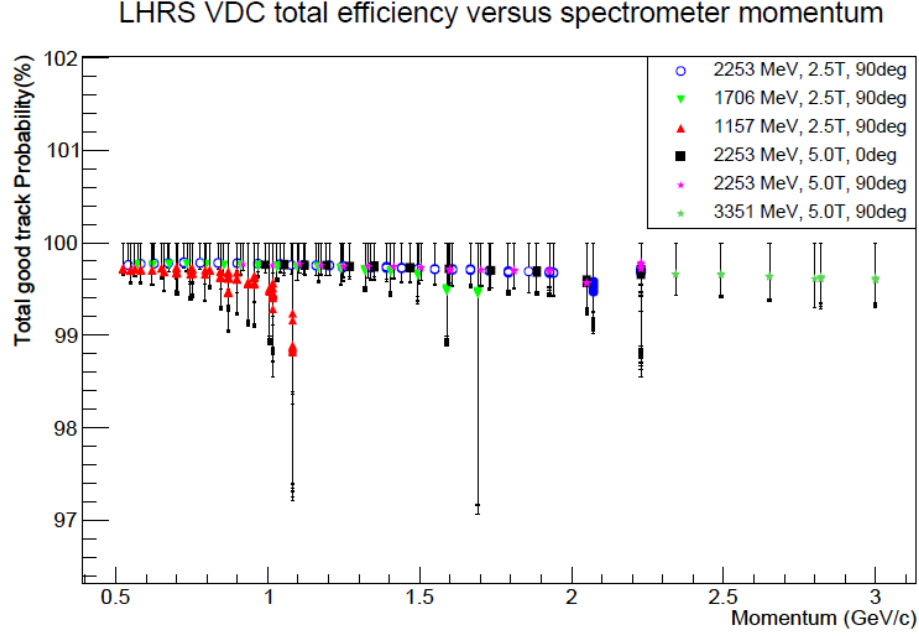


FIGURE 5.1: VDC good track efficiency for LHRs. Figure is from [75].

settings, the number of events with multiple tracks can be as high as 30%. If we only consider one track events, this situation will result in a large uncertainty in the asymmetry measurement. Therefore, the multi-track events were carefully studied to distinguish good events out of them. Fig. 5.1 shows the total VDC good track efficiency plotted against spectrometer momenta [75]. The VDC efficiency is high, and the systematic uncertainty is below 1% for most kinematic settings.

### 5.2.2 Trigger Efficiency

The g2p experiment requires trigger scintillator efficiencies in the cross section measurement. As described in Sec. 3.8.2, the main triggers for RHRS and LHRs are T1 and T3, respectively. The secondary trigger T2 (T4) for the RHRS (LHRs) is used to measure the efficiency of the main trigger. The trigger scintillator efficiency is determined by

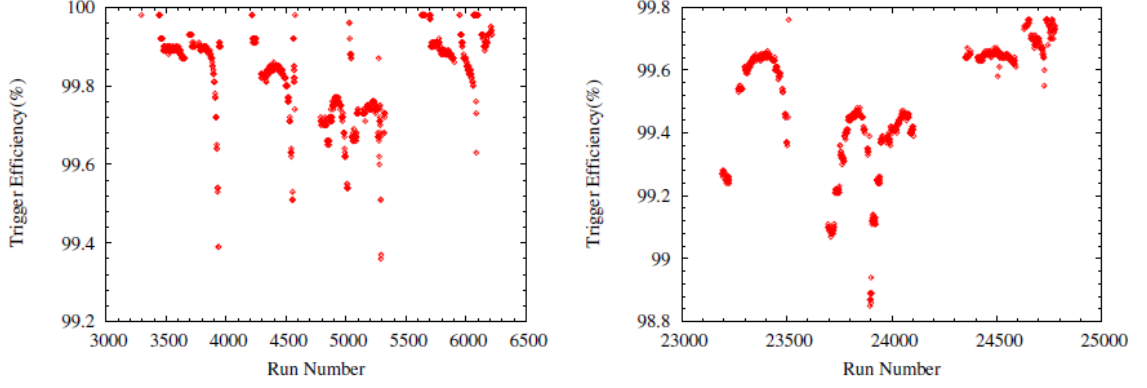


FIGURE 5.2: Trigger efficiency for LHRS (left) and RHRS (right). Figure is from [76].

$$\epsilon_{trig} = \frac{T_{main}}{T_{main} + T_{sec}}, \quad (5.3)$$

where  $T_{main}$  and  $T_{sec}$  are the total number of trigger counts for the main and secondary triggers respectively. For g2p experiment, the trigger efficiency is very high (mostly above 99%) for all runs. The results are shown in Fig. 5.2 [76].

The trigger counts in Eq. 5.3 can be obtained from either the trigger scalers or the trigger latch pattern. The trigger latch pattern is trigger signals formed in the TDC, and thus is better over the scalers since this is correlated with the recorded events and analysis cuts can be applied. However, because of this correlation with the recorded events, the latched trigger can possess deadtime effects. The deadtime (DT) is related to the livetime (LT) by  $DT = 1 - LT$ . The livetime is then the ratio of accepted triggers multiplying the prescale factor to the total triggers expressed as:

$$LT = \frac{ps_i T_i^{acc}}{T_i^{tot}}, \quad (5.4)$$

where the accepted triggers are obtained from the latch pattern, and the total triggers are from the trigger scalers.

### 5.2.3 PID Efficiency

The g2p experiment requires good PID to minimize the pion contamination in the asymmetry analysis. This is achieved by a combination of the gas Cherenkov detector and lead glass calorimeters. The Cherenkov threshold cut removes the majority of pions because pions cannot directly trigger this detector. The detection efficiency of the gas Cherenkov is determined by the number of events that trigger the Cherenkov divided by the number of events selected in the calorimeters. For g2p experiment, the efficiency of the gas Cherenkov was above 99.8% for all kinematic settings. The lead glass calorimeters for LHRS consists of two identical layers of pion rejectors. A two-dimensional cut on the two pion rejectors removes the low energy electrons. Similarly the detection efficiency of the pion rejectors is determined by the number of events that trigger both layers of the lead glass divided by the events selected in the gas Cherenkov. The efficiency for the lead glass calorimeters is above 98% for all kinematic settings.

The detector cuts used for PID are gas Cherenkov threshold cut, cut on the first pion rejector, and total energy deposit cut. These cuts are optimized to suppress most pions while minimize cutting away good electron events. The details of the cuts can be found in Ref. [77]. The cut efficiency for gas Cherenkov is very high (greater than 99.8%) for most of the kinematic settings (see Fig. 5.3). The cut efficiency for pion rejectors is approximately 99% for all kinematic settings (see Fig. 5.4).

The pion suppression is checked by examining the residual pion contamination with the above cuts. The level of residual pions contamination is very low, with  $\pi/e < 0.0052$  for all kinematic settings (see Fig. 5.5).

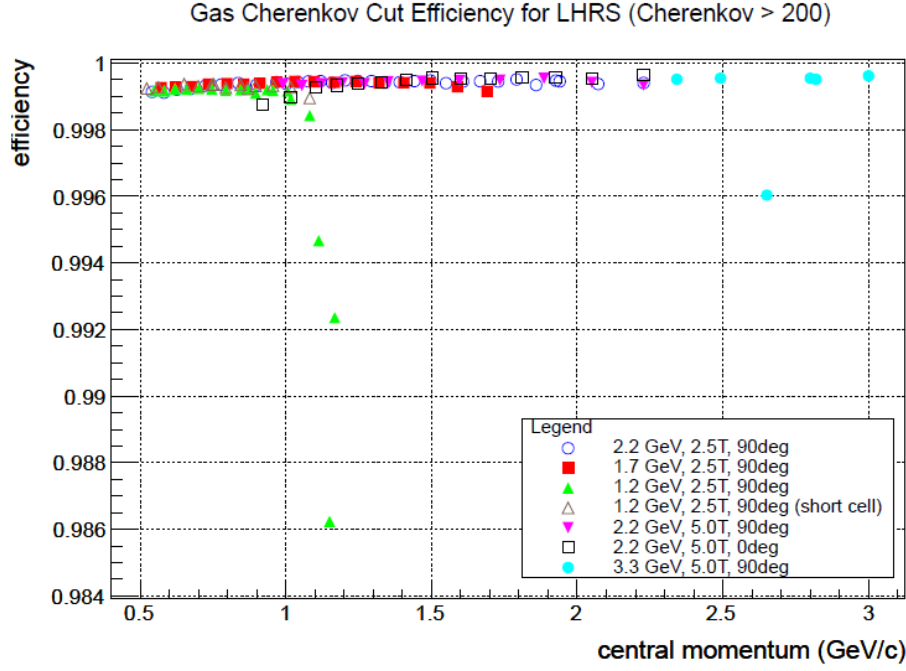


FIGURE 5.3: Cut efficiency for the LHRS gas Cherenkov. Figure is from [77].

### 5.3 False Asymmetry

The false asymmetry for the electron beam was checked with unpolarized data from unpolarized target (carbon and dummy) runs, since the beam charge, the trigger livetime, the power supply for each electronics, and the commercial electricity can potentially cause false asymmetry. Good electrons were selected by applying the PID cuts that were also used for the polarized  $\text{NH}_3$  target data, while loose acceptance cuts were applied to improve the statistics. Fig. 5.6 shows the false asymmetries for each run for the setting of 1.7 GeV beam energy and 2.5T transverse target field. The average false asymmetry is  $-190 \pm 151$  ppm, which will be used as part of the systematic uncertainty on the final results.



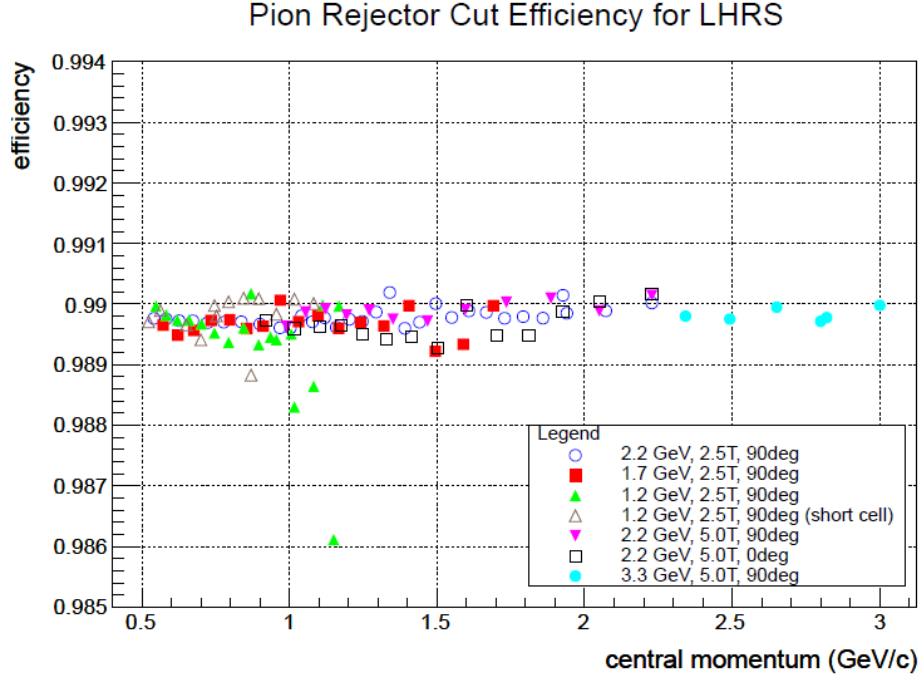


FIGURE 5.4: Cut efficiency for the LHRS lead glass calorimeters. Figure is from [77].

## 5.4 Dilution Factor

The raw asymmetry needs to be corrected by the dilution factor to remove the contamination from unpolarized material in the target cell. In g2p experiment, the dilution comes from the nitrogen in the  $\text{NH}_3$  target material, the helium used to keep the target at low temperature, and the aluminum target end caps. The raw asymmetry can be written as:

$$A_{raw} = \frac{Y_{H+} - Y_{H-}}{Y_{H+} + Y_{H-} + Y_{bg}}, \quad (5.5)$$

where  $Y_{bg}$  is the background yield arisen from the other elements:

$$Y_{bg} = Y_N + Y_{He} + Y_{Al}. \quad (5.6)$$

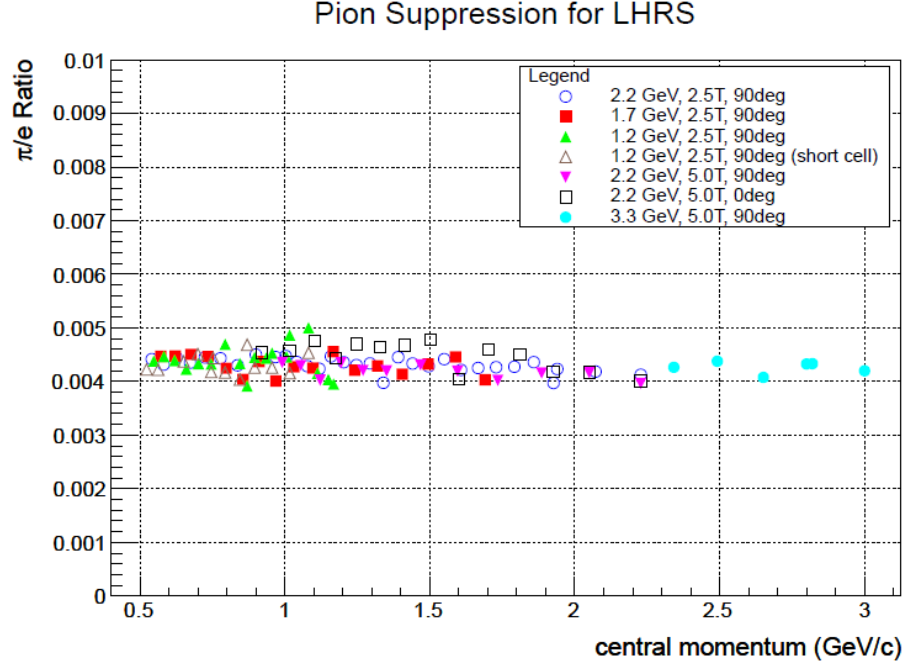


FIGURE 5.5: Residual pion contamination for LHRs. Figure is from [77].

The asymmetries of the background events are very small from the false asymmetry results in Sec. 5.3, and are neglected here.

The dilution factor is defined as:

$$D_f = 1 - \frac{Y_{bg}}{Y_{prod}}, \quad (5.7)$$

where  $Y_{prod}$  is the yield of a production run with  $\text{NH}_3$  target.

In the resonance scattering region of this experiment, events from the other elements cannot be isolated from the H events with detector or acceptance cuts. The dilution is determined with data taken with reference target cells: the dummy target which is an empty target identical to the production target cell, and the carbon target foil. The target stick was inserted into a target nose filled with liquid helium. Fig. 5.7 illustrates the target setup on the target stick. In addition, data were also taken with “empty” target, which is the target nose filled with liquid helium.

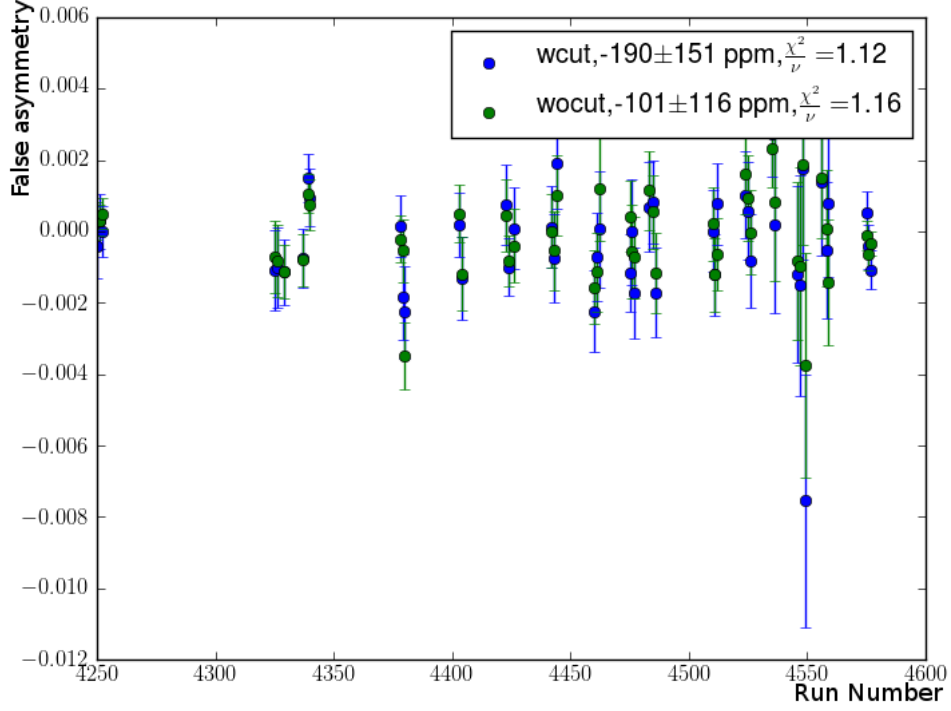


FIGURE 5.6: False asymmetries plotted against run number for the setting of 1.7 GeV beam energy and 2.5T transverse target field. Blue dots represent results obtained with the detector cuts, while green ones are without cuts. Figure is from [78].

Yield of each target can be expressed by the cross sections:

$$Y_{prod} = N_A \left( \frac{p_f l_{tg} \rho_N}{M_N} \sigma_N + \frac{p_f l_{tg} \rho_H}{M_H} \sigma_H + \frac{(l_{tot} - p_f l_{tg}) \rho_{He}}{M_{He}} \sigma_{He} + \frac{l_{Al} \rho_{Al}}{M_{Al}} \sigma_{Al} \right), \quad (5.8)$$

$$Y_{bg} = N_A \left( \frac{p_f l_{tg} \rho_N}{M_N} \sigma_N + \frac{(l_{tot} - p_f l_{tg}) \rho_{He}}{M_{He}} \sigma_{He} + \frac{l_{Al} \rho_{Al}}{M_{Al}} \sigma_{Al} \right), \quad (5.9)$$

$$Y_{dummy} = N_A \left( \frac{l_{tot} \rho_{He}}{M_{He}} \sigma_{He} + \frac{l_{Al} \rho_{Al}}{M_{Al}} \sigma_{Al} \right), \quad (5.10)$$

$$Y_{empty} = N_A \left( \frac{l_{tot} \rho_{He}}{M_{He}} \sigma_{He} \right), \quad (5.11)$$

$$Y_{carbon} = N_A \left( \frac{(l_{tot} - l_C) \rho_{He}}{M_{He}} \sigma_{He} + \frac{l_C \rho_C}{M_C} \sigma_C \right), \quad (5.12)$$

where  $N_A$  is the Avogadro's number, and  $l_x$  is the length of type  $x$  target. The definitions of  $l_{tg}$  and  $l_{tot}$  are illustrated in Fig. 5.8, where  $l_{tg}$  is the target cell length,



FIGURE 5.7: Target setup on the target stick for the g2p experiment.

and  $l_{tot}$  is the length of beam path inside the target nose. Both of them were surveyed before the experiment [79]. The contamination from the aluminum end caps of target cell is formed by the subtraction of the empty target yield from the dummy target yield:

$$Y_{Al} = Y_{dummy} - Y_{empty}, \quad (5.13)$$

and the helium contamination in the production run can be extracted from the empty target yield:

$$Y_{He} = Y_{empty} \cdot \left(1 - \frac{l_{tg}}{l_{tot}} p_f\right). \quad (5.14)$$

where  $p_f$  is the packing fraction which represents the relative length of ammonia to the target cell. We will introduce the extraction of this factor in Sec. 5.4.1.

The nitrogen contamination is more complicated since no nitrogen target data

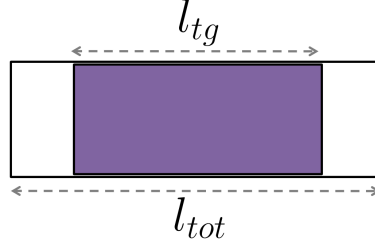


FIGURE 5.8: Illustration of target cell and target nose.  $l_{tg}$  is the target cell length, and  $l_{tot}$  is the length of beam path inside the target nose.

have been taken in the g2p experiment. The cross section ratio  $\sigma_N/\sigma_C$  from the Bosted model [80] is used to scale up the carbon cross section to represent the nitrogen cross section. The Bosted model is tuned with the nitrogen data from the Small Angle GDH (saGDH) experiment, which was performed at similar kinematics as the g2p experiment. The Bosted model has been tuned to  $\pm 5\%$  level [81]. The nitrogen contamination is then expressed by the tuned Bosted model ratio with the g2p carbon target data:

$$Y_N = (Y_{carbon} - Y_{empty} \cdot \frac{l_{tot} - l_C}{l_{tot}}) p_f K_{CN} \frac{\sigma_N}{\sigma_C}, \quad (5.15)$$

where  $K_{CN} = \frac{l_{tg} \rho_N M_C}{l_C \rho_C M_N}$ .

The dilution factor is derived from the above formulae to be:

$$D_f = 1 - \left( \frac{Y_{dummy}}{Y_{prod}} + p_f K_{CN} \frac{\sigma_N}{\sigma_C} \frac{Y_{carbon}}{Y_{prod}} - p_f \frac{l_{tg} + (l_{tot} - l_c) K_{CN} \frac{\sigma_N}{\sigma_C}}{l_{tot}} \frac{Y_{empty}}{Y_{prod}} \right), \quad (5.16)$$

Alternatively, the dilution factor can be extracted from the cross section model:

$$D_f = \frac{3 \frac{\rho_{NH3} p_f l_{tg}}{M_{NH3}} \sigma_H}{\frac{\rho_{NH3} p_f l_{tg}}{M_{NH3}} (3\sigma_H + \sigma_N) + \frac{\rho_{He} (l_{tot} - p_f l_{tg})}{M_{He}} \sigma_{He} + \frac{\rho_{Al} l_{Al}}{M_{Al}} \sigma_{Al}}. \quad (5.17)$$

The preliminary results of dilution factor for each setting during the g2p experiment can be found in Ref. [82].

Table 5.1: Parameters used in dilution calculation [79].

$l_{tg}$	2.8307 cm
$l_{tot}$	3.7045 cm
$l_{Al}$	0.0004 cm
$\rho_{NH_3}$	0.817 g/cm <sup>3</sup>
$\rho_{He}$	0.145 g/cm <sup>3</sup>
$\rho_{Al}$	2.7 g/cm <sup>3</sup>

#### 5.4.1 Packing Fraction

The dilution factor calculation requires the determination of packing fraction. The  $NH_3$  target cell is comprised of solid ammonia beads and liquid helium. The packing fraction is defined as the ratio of the length of ammonia to the total target length. The packing fraction is extracted using data of the  $NH_3$  target, the dummy target and the carbon target.

The yield of production data using the  $NH_3$  target can be expressed as sum of the yields of its components [83]:

$$Y_{prod} = Y_{He}^{out} + (1 - p_f)Y_{He}^{full} + p_f Y_{NH_3}^{full}, \quad (5.18)$$

where:

- $Y_{He}^{out}$  is the yield for helium outside the target chamber while inside the target nose,
- $Y_{He}^{full}$  is the yield for the target chamber full of helium,
- $Y_{NH_3}^{full}$  is the yield for the target chamber full of ammonia,
- $p_f$  is the packing fraction.

The  $Y_{He}^{out}$ , and  $Y_{He}^{full}$  are extracted by using the yield from dummy target data:

$$Y_{He}^{out} = \frac{l_{tot} - l_{tg}}{l_{tot}} Y_{dummy}, \quad (5.19)$$

$$Y_{He}^{full} = \frac{l_{tg}}{l_{tot}} Y_{dummy}. \quad (5.20)$$

The packing fraction then can be derived from the above formulae to be:

$$p_f = \frac{l_{tot}}{l_{tg}} \left( \frac{Y_{prod}}{Y_{dummy}} - 1 \right) \left( \frac{Y_{NH_3}^{full}}{Y_{He}^{full}} - 1 \right). \quad (5.21)$$

Since it is not possible to obtain  $Y_{NH_3}^{full}$  from data, cross section input of elastic form factor models is used [84]. The yield can be expressed by the cross section as:

$$Y_x \sim \sigma_x \cdot \rho_x, \quad (5.22)$$

where  $\rho_x = \frac{\rho_{mass} \cdot l_x \cdot N_A}{M_{molar}}$ .  $\rho_{mass}$ ,  $l_x$ , and  $M_{molar}$  are the mass density, length, and molar mass of the material, respectively, and  $N_A$  is Avagadro's number. Then the expression of packing fraction from Eq. 5.21 is given as:

$$p_f = \frac{l_{tot}}{l_{tg}} \left( \frac{Y_{prod}}{Y_{dummy}} - 1 \right) \left( \frac{\sigma_N \frac{\rho_{mass,N}}{M_N} + \sigma_H \frac{\rho_{mass,H}}{M_H}}{\sigma_{He} \frac{\rho_{mass,He}}{M_{He}}} - 1 \right)^{-1}. \quad (5.23)$$

The preliminary results of packing fraction for each settings during the g2p experiment can be found in Ref [83].

## 5.5 Acceptance Cuts

For the system of septum and HRS, the small acceptance and heavy shielding provided a low background environment. Only particles with selected momentum and angles can reach the detector plane. Detector PID cuts remove more background events. Additionally, acceptance effect essentially cancels in the asymmetry. Simplified acceptance cuts were chosen to remove events far from the main acceptance, which can be rescattered events at the edge of the acceptance. Fig. 5.9 shows the acceptance cuts used for the asymmetry analysis of the setting of 1.7 GeV beam energy, and 2.5 T transverse target field. The cuts are chosen according to the distributions of momentum fraction  $\delta$  (Eq. 4.1), and  $x$  and  $y$  on the focal plane.

The cuts are placed at the falling edges of the distributions to maximize the statistics. The focal plane variable cuts were chosen instead of target plane vertex variables, because due to the transverse target field bending effect, the target plane vertical angle  $\theta$  varies a lot among different HRS momentum runs, while the positions, or equivalently angles, on focal plane cover similar region for all the runs. This makes it possible to choose a universal cut for each variable.



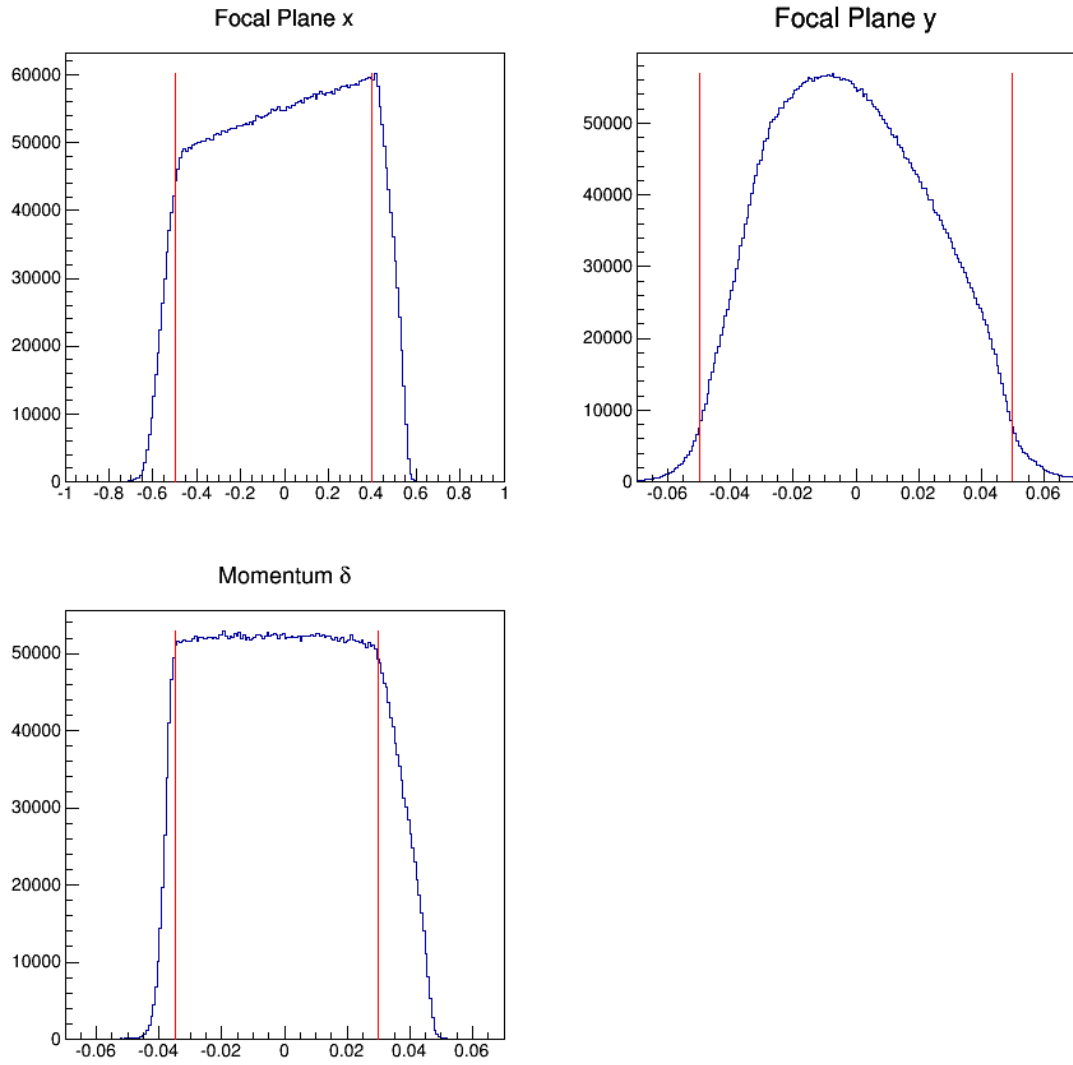


FIGURE 5.9: Acceptance cuts used for asymmetry analysis for the setting of 1.7 GeV, 2.5 T transverse target field.

# 6

## Results

### 6.1 Asymmetry Measurements

Asymmetries were measured while the target polarization was parallel ( $A_{\parallel}$ ) or perpendicular ( $A_{\perp}$ ) to the longitudinally polarized incident electrons. The raw asymmetries are calculated by forming the ratio of the difference in the counts of electrons in each helicity state to their sum by:

$$A_{raw} = \frac{Y_+ - Y_-}{Y_+ + Y_-} \quad (6.1)$$

where  $Y^{\pm}$  are the normalized yield in each helicity state. The yield can be calculated as:

$$Y = \frac{ps \cdot N}{Q \cdot LT \cdot \epsilon_{det}} \quad (6.2)$$

where

- $N$  is the number of scattered electrons detected within the acceptance and PID cuts.

- $ps$  is the prescale factor of the event type.
- $Q$  is the total charge.
- $LT$  is the livetime correction.  $N$ ,  $Q$ , and  $LT$  are extracted for each helicity state.
- $\epsilon_{det}$  is the detector efficiency, which is the product of VDC efficiency, trigger efficiency and PID efficiency:

$$\epsilon_{det} = \epsilon_{VDC} \cdot \epsilon_{trig} \cdot \epsilon_{PID}, \quad (6.3)$$

and is described in Sec. 5.2.

The physics asymmetries are related to the raw asymmetries by:

$$A_{phy} = \frac{A_{raw}}{f P_b P_t}, \quad (6.4)$$

where  $P_b$  and  $P_t$  are the beam and target polarizations, respectively, and  $f$  is the dilution factor due to the scattering from any unpolarized material as discussed in details in Sec. 5.4.

The asymmetries are extracted from the data files recorded by the detector package and the DAQ system. The raw data files are stored by the DAQ in the mass storage system (MSS) of Jefferson Lab. One raw data file was recorded for every run on each HRS arm during the experiment.

These raw data files are then analyzed using the Hall A software ANALYZER, and are converted to N-tuples in the format of ROOT files. For g2p experiment, the parts to extract information of the beam position, helicity and optics reconstruction in the standard Hall A ANALYZER are not used, and instead stand-alone programs are constructed and combined to produce the final N-tuples. The scalar information

is also extracted from the raw data files. Scalar information and N-tuples are then combined to produce results for this analysis.

The values of  $N^\pm$  in  $Y^\pm$  of Eq. 6.1 are extracted for each run from the N-tuple outputs. This process involves defining and counting the good electron events for each helicity state. A few cuts are used to choose the good events. The cuts consist of the trigger cut, the detector cut, and the acceptance cut, which are described in Sec. 5.2 and 5.5.

## 6.2 Statistical Uncertainty

From Eq. 6.1, the statistical uncertainty of the raw asymmetry can be derived as:

$$\sigma A_{raw} = \frac{1}{(Y_+ + Y_-)^2} \sqrt{4Y_-^2(\sigma Y_+)^2 + 4Y_+^2(\sigma Y_-)^2}, \quad (6.5)$$

where the calculation of  $\sigma Y$  requires the calculation of  $\sigma N$ .

The calculation of  $\sigma N$  is discussed in Appendix A, and is derived as:

$$\sigma_N = S \cdot \sqrt{N}, \quad (6.6)$$

where the correction factor  $S$  is:

$$S = \sqrt{1 - LT \cdot R(1 - \frac{1}{ps})}. \quad (6.7)$$

$R$  can be obtained as the ratio of the number of accepted events to the number of recorded events:  $\frac{N^{acc}}{N^{rec}}$ .

Then  $\sigma Y$  from Eq. 6.2 can be expressed as:

$$\sigma Y = \frac{Y \cdot S}{\sqrt{N}}. \quad (6.8)$$

Inserting this into Eq. 6.5 leads to:

$$\sigma A_{raw} = \frac{2Y_+Y_-}{(Y_+ + Y_-)^2} \sqrt{\frac{S_+^2}{N_+} + \frac{S_-^2}{N_-}} \quad (6.9)$$

And then  $\sigma A_{phys}$  is obtained by:

$$\sigma A_{phys} = \frac{1}{P_b \cdot P_t \cdot f} \sigma A_{raw}, \quad (6.10)$$

where the uncertainties of the target and beam polarizations and dilution factor are considered as systematic uncertainty, thus are not considered in this equation.

The asymmetries were formed in each bin of  $Q^2$  or  $\nu$  to show the evolution. For each momentum setting, several runs were taken, and therefore, the asymmetry calculations involve the weighted average over the corresponding runs. The average asymmetries are obtained as:

$$A = \frac{\sum_i (A_i / \sigma A_i^2)}{\sum_i (1 / \sigma A_i^2)}, \quad (6.11)$$

where  $i$  denotes each run. And the statistical uncertainties are:

$$\sigma A = \sqrt{\frac{1}{\sum_i (1 / \sigma A_i^2)}} \quad (6.12)$$

With the results of beam and target polarizations, and dilution, the physics asymmetries for the configuration of 1.7 GeV, 2.5 T transverse target field are shown in Fig. 6.1. The statistical uncertainties are shown as the error bars in the plot.

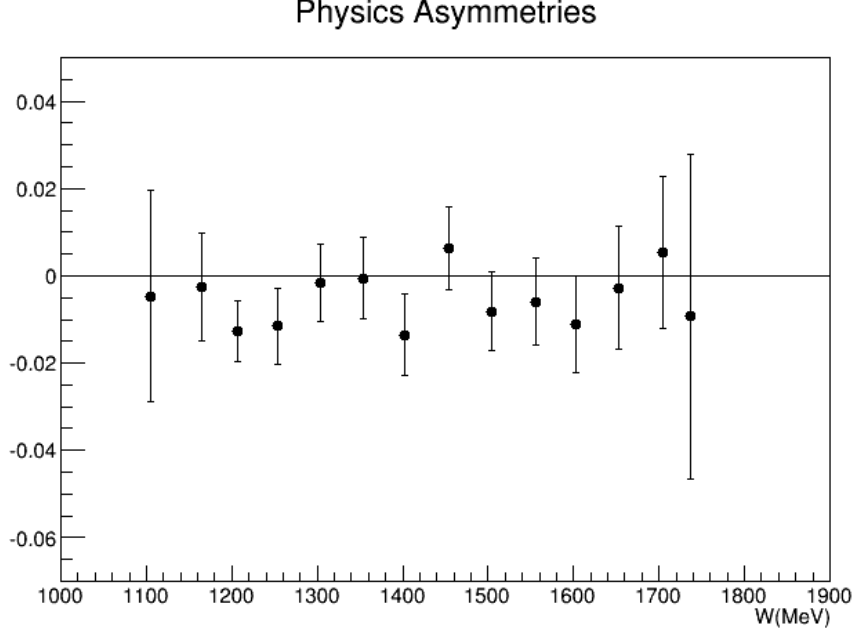


FIGURE 6.1: Physics asymmetries for the configuration of 1.7 GeV, 2.5 T transverse target field. Error bars represent the statistical uncertainties.

## 6.3 Model Predictions

### 6.3.1 MAID

The MAID model [85] utilizes phenomenological fits to the photo-production and electro-production data for the the nucleon from the pion-production threshold to  $W=2$  GeV. The major resonances are modelled by assuming the resonance contributions are in Breit-Wigner forms. The contribution of the resonances to the transverse cross sections is expressed as:

$$\sigma_{\frac{1}{2}(\frac{3}{2})} = \frac{4M}{W_{res}\Gamma_{res}} A_{\frac{1}{2}(\frac{3}{2})}^2 B(\nu, Q^2), \quad (6.13)$$

where  $M$  is the nucleon mass,  $B(\nu, Q^2)$  represents the generalization to electroproduction of the Breit-Wigner form,  $W_{res}$  is the mass of the resonance,  $\Gamma_{res}$  is the resonance width, and  $A_{\frac{1}{2}(\frac{3}{2})}$  is the relevant photo-coupling helicity amplitude. A non-resonant background and contributions from vector mesons are also included.

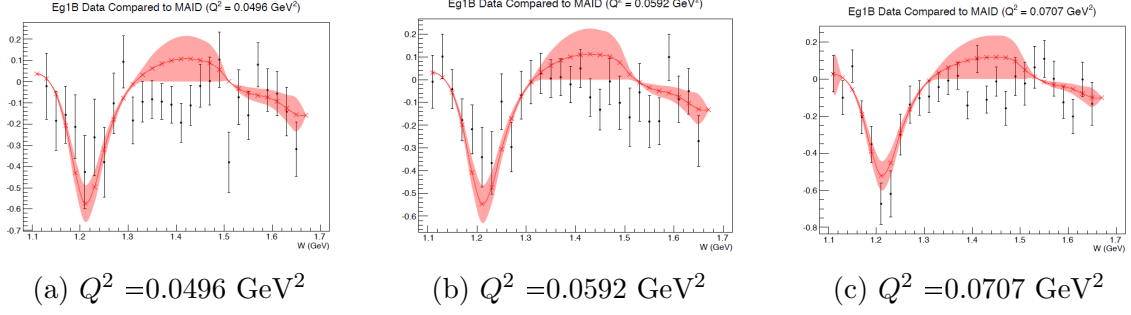


FIGURE 6.2: Comparisons of MAID model with the Eg1b data. The lowest  $Q^2$  settings, which is also closest to the kinematic region of g2p experiment, were chosen for the comparisons.

From Fig. 2.7, the generalized spin polarizabilities of both neutron and proton can be well described by the MAID2007 model in most regions, except that for neutron  $\gamma_0$ , at  $Q^2 = 0.1$  GeV point, the model overestimate the data. MAID2007 is the model used for the analysis in this thesis, which includes the polarized radiative corrections, and forming longitudinal cross section differences  $\Delta\sigma_{\parallel}$ .

In order to have an idea of the uncertainties of MAID2007 model in the low  $Q^2$  region, comparisons have been made with the data from Eg1b experiment in Hall B at Jefferson Lab as shown in Fig. 6.2. The lowest  $Q^2$  settings, which is also closest to the kinematic region of g2p experiment, were chosen for the comparisons. The uncertainties are estimated to be 15% for  $W < 1.3$  GeV, 100% for  $1.3 \text{ GeV} < W < 1.5$  GeV, and 50% for  $W > 1.5$  GeV. These numbers are used as systematic uncertainties of the MAID2007 model for the physics results.

### 6.3.2 Peter Bosted Model

The Peter Bosted model utilizes an empirical fit to the measurements of the inclusive inelastic electron-proton scattering cross sections in the kinematic range of  $0 \leq Q^2 \leq 8 \text{ GeV}^2$  and  $1.1 < W < 3.1 \text{ GeV}$  [86]. The fit covers the data from the high precision longitudinal/transverse cross section measurements from experiments E94-110 [87],

E00-116 [88], E00-002 [89] at Jefferson Lab Hall C and SLAC DIS experiments [90], and the photonproduction data from DAPHNE [91], and uses Breit-Wigner forms for all resonances. The model also includes the empirical fits to the electron-nucleus ( $A > 2$ ) scattering cross sections [92].

The Bosted model has been regularly updated in recent years to include all available unpolarized data. Attempts have also been made to address nuclear effects in the Bosted fit. The Bosted model is used to predict the unpolarized cross sections for the analysis in this thesis, which includes extracting the  $\Delta\sigma_{\perp}$  from data, the unpolarized radiative corrections, and the dilution factor analysis. A systematic uncertainty of 10% is assumed for this model in the analysis [86].

## 6.4 Radiative Correction

The electron scattering diagram shown in Fig. 1.1 is the leading order process of one photon exchange. This is the process considered in the theoretical predictions. However, the data from experiments contain higher order processes, which need to be corrected so that the data can be compared with the theory predictions. This correction analysis is known as the radiative correction, which consists of the following categories:

- Ionization.
- Virtual photon one loop diagram.
- Internal and External Bremsstrahlung.

Ionization process causes the electron to lose energy through Møller scattering when the electron passes through the target and surrounding materials. The ionization energy loss is roughly proportional to the thickness of the material: a few MeV



per  $g/cm^2$  of the material. The proportion factors are determined from the ESTAR program for stopping power.

Fig. 6.3 shows the next-to-leading order Feynman diagrams of internal radiative corrections. Graphs (a), (b), (c), and (d) represent the virtual photon one loop processes, and graphs (e) and (f) represent the bremsstrahlung before and after the scattering. The first four processes contribute to the cross section at  $\mathcal{O}(\alpha^4)$ , and are relatively small corrections compared to the bremsstrahlung processes which are of  $\mathcal{O}(\alpha^3)$ . The bremsstrahlung processes shown in graphs (e) and (f) are internal bremsstrahlung, and there is also external radiation produced when the electron passes through the materials surrounding the target. The right graph in Fig. 6.4 shows the internal and external radiations. The incident electron loses energy by passing through the materials and also during the interaction itself, before being detected in the spectrometer. Therefore, the electron energy at reaction vertex  $E'_s$  is less than the incoming energy  $E_s$  that enters the hall, and the actual scattered energy at the vertex  $E'_p$  is larger than the detected energy  $E_p$ . The physical accessible kinematic region is the area bounded by the elastic scattering energy shown in the left graph of Fig. 6.4. A state with larger scattered energy  $E'_p$  can affect the states with smaller scattered energies, but not vice versa. The elastic scattering has the largest scattered energy, and can affect the entire spectrum. Hence, the radiation tail from elastic peak needs to be subtracted from all other spectra first.

The external bremsstrahlung and ionization are spin-independent, while the internal radiation can involve spin-flip during the scattering interaction, so the polarization effects need to be considered in the internal corrections to the polarized cross section differences.

For the unpolarized cross section, the external and internal radiative corrections are calculated with Mo and Tsai's formalism [93] using the program RADCOR.F [94]. The "energy peaking approximation" by Stein [95] is used to simplify the calculation

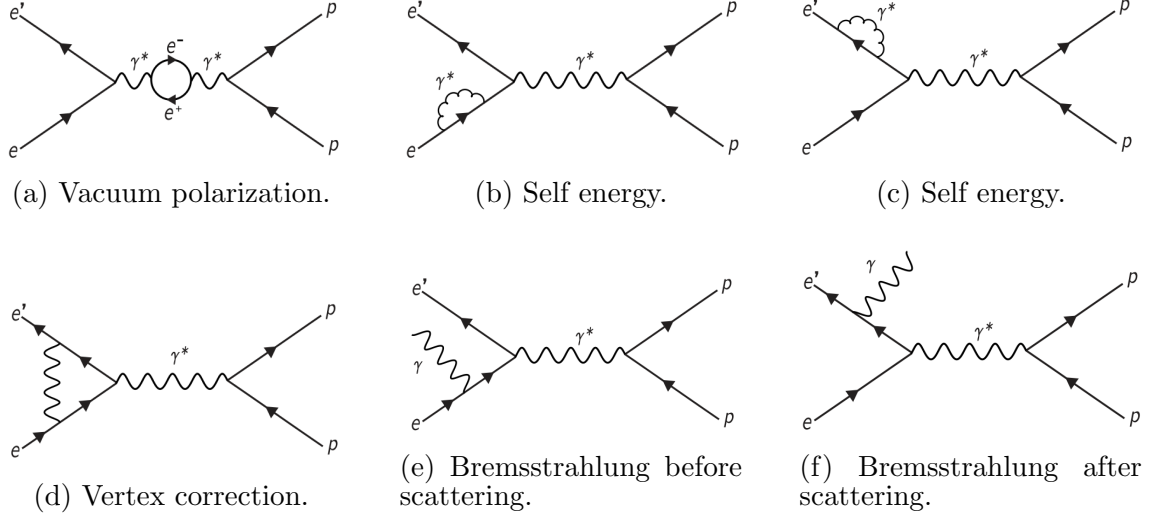


FIGURE 6.3: Next to leading order internal radiative correction.

formula, since the radiation effects are strongly peaked in the grey region in the left graph of Fig. 6.4. This approximation allows us to reduce the two dimensional integration over all incident beam energies and all scattered electron energies to two one dimensional line integrals. For the polarized cross section difference, the formalism of Akushevich [96] is used for the internal corrections with the program POLRAD [97].

In order to obtain the Born cross section of the leading order diagram in Fig. 1.1, an iterative process is implemented. Since the Born cross section  $\sigma_{Born}$  is unknown, either cross section models or data are used as the initial input. The  $\sigma_{Born}$  is then radiated to produce the experimental cross section  $\sigma_{exp}$ . This result is compared to the actual experimental measured cross section. The difference is subtracted from the initial model and the new model is used to do the radiation again. Typically the results converge after a few iterations. The POLRAD program was improved by Slifer and Choi [98] to allow an iterative procedure to obtain the Born cross section.

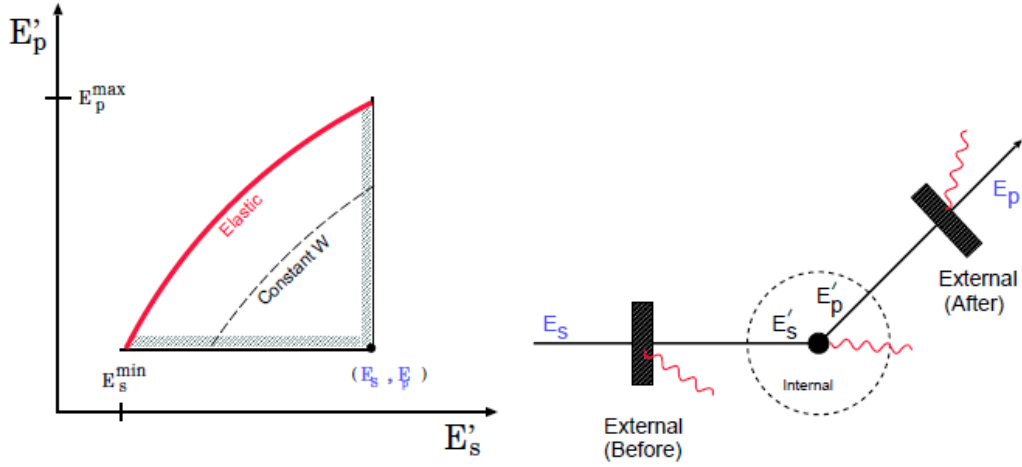


FIGURE 6.4: Left: The kinematic region involved in the radiative correction. Right: External and internal radiations.

For the analysis of this thesis, since the cross section analysis is ongoing, the unpolarized radiative corrections were carried out with the nitrogen data of the small angle GDH experiment at Jefferson Lab Hall A, and the Bosted model [80] was tuned to describe the Born cross section in the kinematic region of  $0.02 \text{ GeV}^2 < Q^2 < 0.30 \text{ GeV}^2$  at  $\pm 5\%$  level [81]. The kinematic region covers the kinematics of the g2p experiment. This tuned Bosted model is used for the unpolarized radiative correction. For the polarized cross section difference correction, MAID model [85] was used as the Born cross section input. Fig. 6.5 shows the radiated and original asymmetries from the models, in which the cross section difference comes from the MAID model and unpolarized cross section comes from the Bosted model.

The difference between these two curves are applied to the data asymmetry as the radiative correction. The results are shown in Fig. 6.6.

## 6.5 Systematic Uncertainty

Table. 6.1 summarizes the sources of the systematic uncertainties associated with the calculation of the asymmetry. The dilution factor and the radiative correction

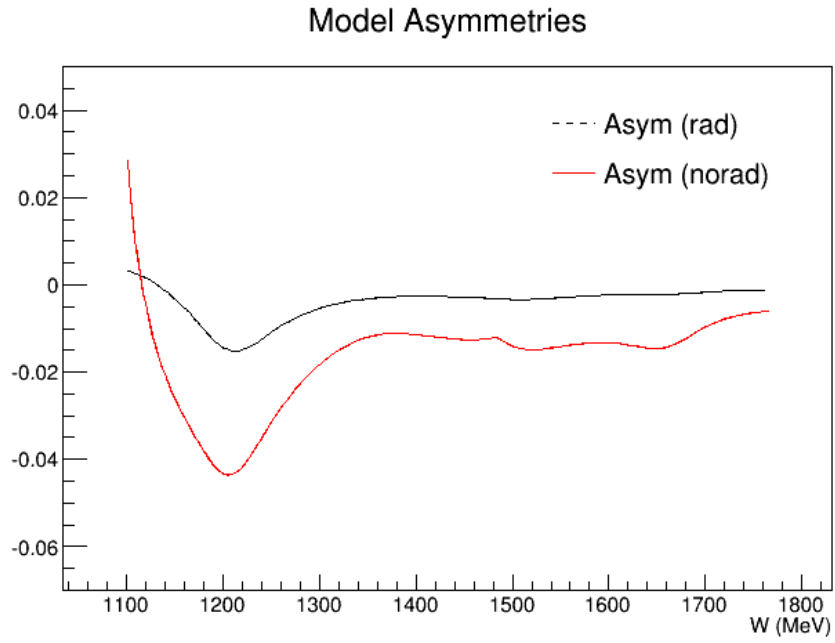


FIGURE 6.5: Radiated asymmetry compared with asymmetry from models.

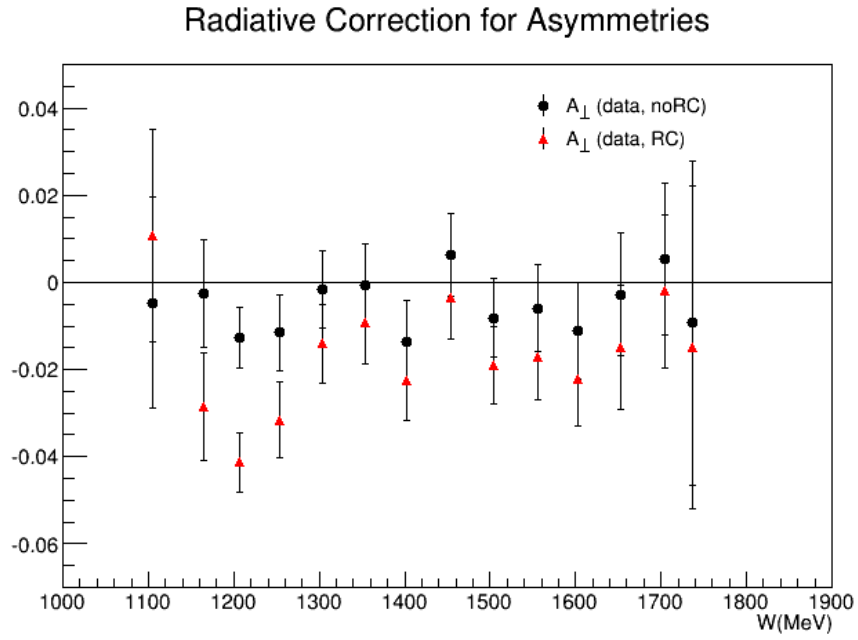


FIGURE 6.6: Asymmetries before and after the radiative correction.

Table 6.1: Summary of the systematic uncertainties.

Source	Analysis type	Uncertainty	Relative/Absolute
Target polarization	Entire run	1.4% or 0.9%	Relative to $P_t$
Beam polarization	Entire run	1.7%	Relative to $P_b$
Dilution factor	Entire run	16%	Relative to f
False asymmetry	Entire run	$1.9 \times 10^{-4}$	Absolute
Radiative correction	Three segments	15%, 100% or 50%	Relative to $\Delta RC$

are the leading errors, which both come from the model predictions. Other sources are the target and beam polarizations, and the false asymmetry, which are one order smaller. Improvements can be made by using the unpolarized cross section from data of this experiment.

Combining the radiative correction and the systematic uncertainties, the asymmetry results are shown in Fig. 6.7 for the setting of 1.7 GeV, 2.5 T transverse target field. The statistical uncertainties of the data points are larger than the systematic uncertainties, which indicates that the statistics is the impeding factor for proposed precise measurements at the level of 10%, and more data are desired for this particular setting.

## 6.6 Results for $g_2^p$

As introduced in chapter 1,  $g_2$  can be expressed as linear combinations of  $\Delta\sigma_{\parallel}$  and  $\Delta\sigma_{\perp}$  from Eq. 1.26 and 1.27. In the analysis of this thesis,  $\Delta\sigma_{\perp}$  is obtained as the product of transverse asymmetry  $A_{\perp}$  and unpolarized cross section  $\sigma_{unpol}$  as expressed in Eq. 5.2.  $A_{\perp}$  is extracted from data as discussed in Sec. 6.1, and  $\sigma_{unpol}$  is from Bosted model as shown in Fig. 6.8. The combined  $\Delta\sigma_{\perp}$  results are shown in Fig. 6.9.  $\Delta\sigma_{\parallel}$  is from MAID2007 model as shown in Fig. 6.10. The  $g_2^p$  results are shown in Fig. 6.11. The statistical uncertainties are propagated from asymmetries discussed in Sec. 6.2. The systematic uncertainties come from three parts: asymmetries from

## Physics Asymmetries

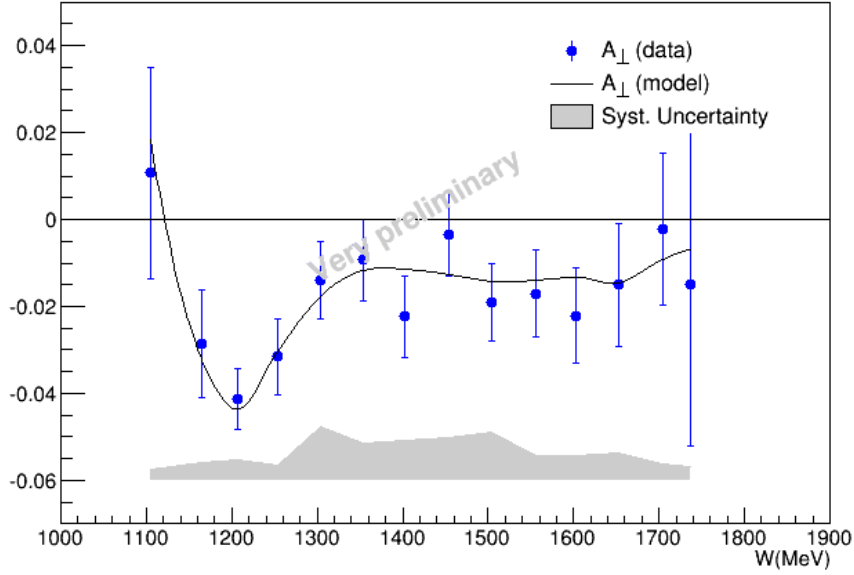


FIGURE 6.7: Asymmetries for the setting of 1.7 GeV, 2.5T transverse target field.

data, unpolarized cross section from the Bosted model, and parallel cross section difference from the MAID2007 model. The  $Q^2$  values of this set of data cover the range of 0.02 to 0.03 GeV<sup>2</sup>.

## 6.7 Discussion

The very preliminary results of the transverse asymmetries show a clear  $\Delta(1232)$  resonance peak, which means  $\Delta(1232)$  resonance has a large contribution in the kinematic region of the g2p experiment. This peak matches the model prediction well. Higher energy resonances are not distinct. More statistics of the data and improved systematic uncertainties are needed to possibly distinguish them. The results also provide constraints to the models.

For the results of  $g_2$ , one thing worth clarifying is that in Fig. 6.11,  $g_2$  results follow the curve of the models closely. This is because although the asymmetry part of the transverse cross section difference  $\Delta\sigma_{\perp}$ , which is the dominant contribution to

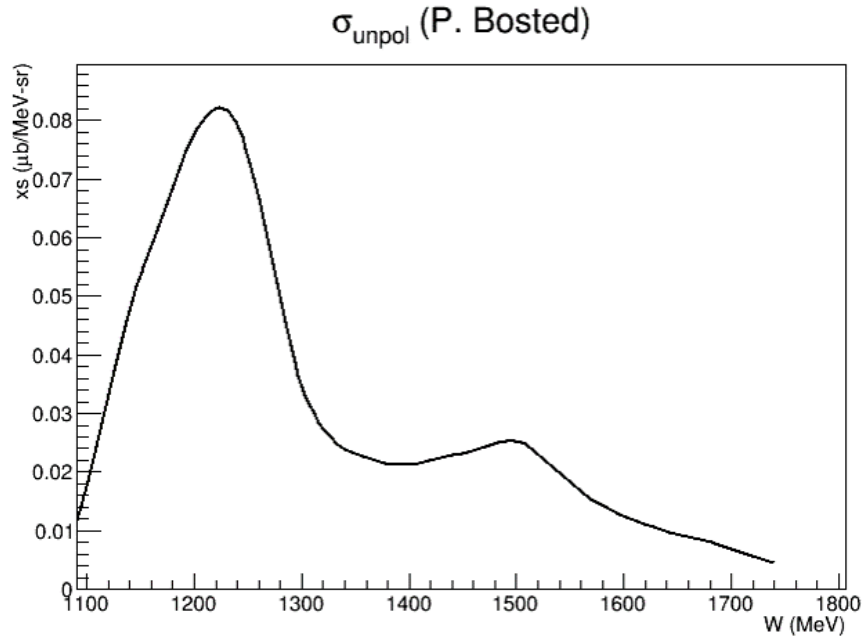


FIGURE 6.8: The unpolarized cross sections predicted from the Bosted model.

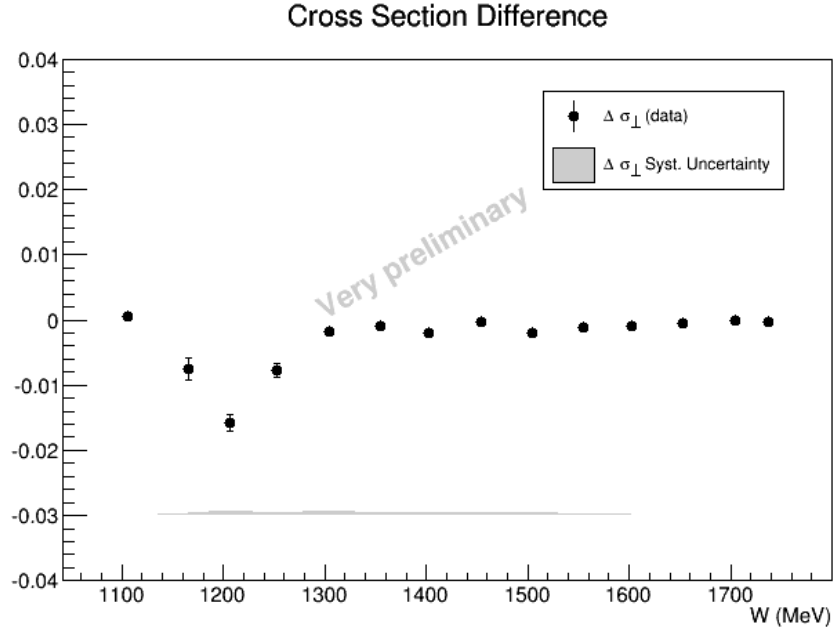


FIGURE 6.9: The transverse cross section difference  $\Delta\sigma_{\perp}$  results from the transverse asymmetries  $A_{\perp}$  and unpolarized cross sections  $\sigma_{unpol}$ .

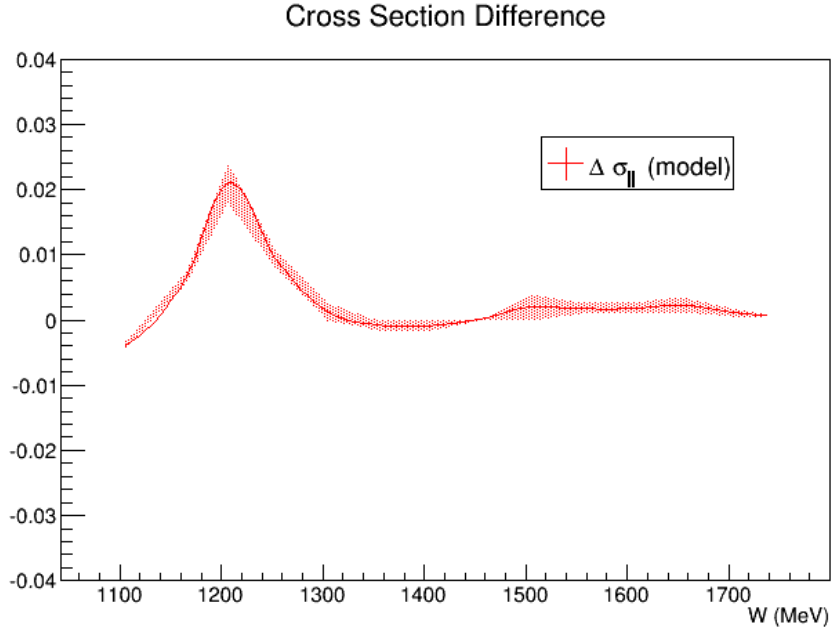


FIGURE 6.10: The longitudinal cross section differences  $\Delta\sigma_{||}$  from the MAID model.

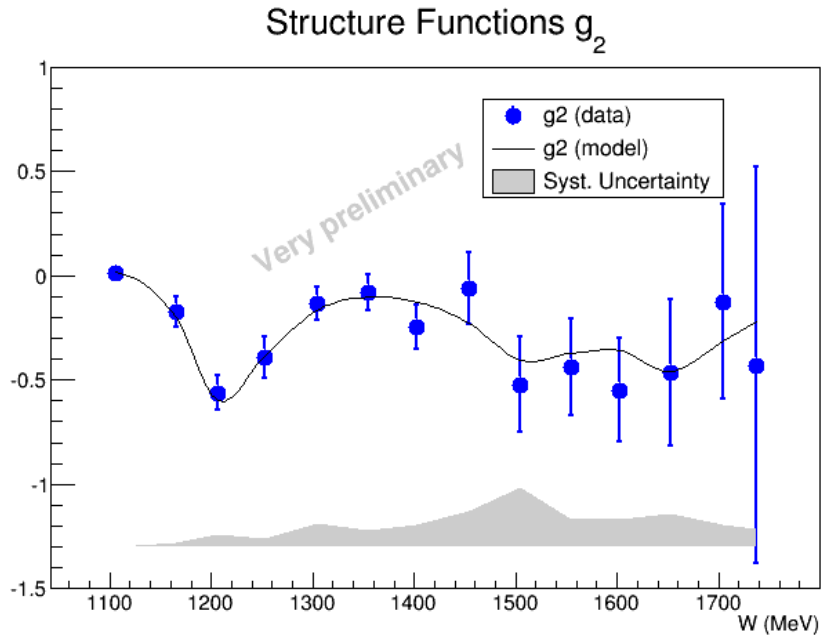


FIGURE 6.11: Results of the spin-dependent structure function  $g_2^p$ .



$g_2$ , is from the data, the unpolarized cross section part is from the Bosted model. In addition, the polarized radiative correction to the asymmetry is from the MAID2007 model without tuning according to the actual cross section from the data. This might imply that the model drives the asymmetry to follow itself.

## 6.8 Summary and Outlook

The experiment E08-027 successfully measured the transverse asymmetries and cross sections at several kinematic settings in the  $Q^2$  range of 0.02–0.2 GeV<sup>2</sup>. In this thesis, the very preliminary results of the first measurement of the transverse asymmetry of the 1.7 GeV configuration are presented. The proton spin structure function  $g_2^p$  of this configuration is obtained and presented with inputs from models and world data.

The cross section analysis is ongoing, which requires the finalized optics and acceptance study and dilution factor analysis. Once the results are obtained, the transverse cross section difference  $\Delta\sigma_\perp$  can be extracted from the data, and the radiative correction study can be improved with the input of cross section from the data instead of models. These studies will improve the systematic uncertainties. More statistics from the data of the 1.7 GeV configuration are also desired to reach the goal of precise measurements at the level of 10%.

The spin structure function  $g_2$ , which is dominated by the transverse contribution, can be calculated with the transverse  $\Delta\sigma_\perp$  from the data of the g2p experiment. The experiment also measured the longitudinal data at one beam energy setting for cross check. The rest of the parallel contribution  $\Delta\sigma_\parallel$  can be obtained from the results of the EG4 experiment at Jefferson Lab Hall B, the analysis of which is underway. Furthermore, the contribution to BC sum rule in the resonance region can be calculated, and together with the extensions to the unmeasured  $x$  region, the results provide input for the test of this sum rule. The generalized spin polarizabilities

can also be formed to provide test of the calculations of  $\chi$ PT theory. The E08-027 collaboration will continue the work on extracting these important quantities.

# Appendix A

## Statistical Uncertainty of Prescaled Events

In g2p experiment, the single triggers were taken with prescale factors due to the high electron rates. This results in a correction to the statistical uncertainty of asymmetry. In this appendix, the correction will be discussed.

The primary inputs for this correction consist of:

- Total number of scalers:  $T$
- Prescale factor:  $ps$
- Acceptance for useful events:  $R$
- Live time:  $LT$
- Total number of recorded events:  $D = T \cdot LT/ps$
- Total number of useful events:  $N = R \cdot D = T \cdot LT \cdot R/ps$

The statistical uncertainty can be separated into two parts. The first part comes from the total number of events  $T$ :

$$\sigma_T = \sqrt{T}, \quad (\text{A.1})$$

$$\Delta\sigma_T = \frac{1}{\sqrt{T}}. \quad (\text{A.2})$$

The second part comes from the acceptance factor  $LT \cdot R$ . This is the effective possibility of the Bi-nominal distribution.  $ps$  is a fixed number here, so it will not introduce any fluctuation. Assume  $T$  is fixed, the statistical uncertainty of  $N$  is:

$$\sigma_N^* = \sqrt{\frac{T}{ps} LT \cdot R(1 - LT \cdot R)} = \sqrt{N(1 - LT \cdot R)}, \quad (\text{A.3})$$

$$\Delta\sigma_N^* = \frac{\sigma_N^*}{N} = \sqrt{\frac{ps(1 - LT \cdot R)}{T \cdot LT \cdot R}} = \sqrt{\frac{1 - LT \cdot R}{N}}. \quad (\text{A.4})$$

Combining  $\Delta\sigma_T$  and  $\Delta\sigma_N^*$  gives the total uncertainty of  $N$ :

$$\Delta\sigma_N = \sqrt{(\Delta\sigma_T)^2 + (\Delta\sigma_N^*)^2} = \sqrt{\frac{1}{N}(1 - LT \cdot R(1 - \frac{1}{ps}))}, \quad (\text{A.5})$$

$$\sigma_N = \Delta\sigma_N \cdot N = \sqrt{N(1 - LT \cdot R(1 - \frac{1}{ps}))}. \quad (\text{A.6})$$

This gives the correction as:

$$S = \sqrt{1 - LT \cdot R(1 - \frac{1}{ps})}. \quad (\text{A.7})$$

Here,  $R$  can be obtained as the ratio of the number of accepted event to the number of recorded events  $\frac{N_{acc}}{N_{rec}}$ .

# Appendix B

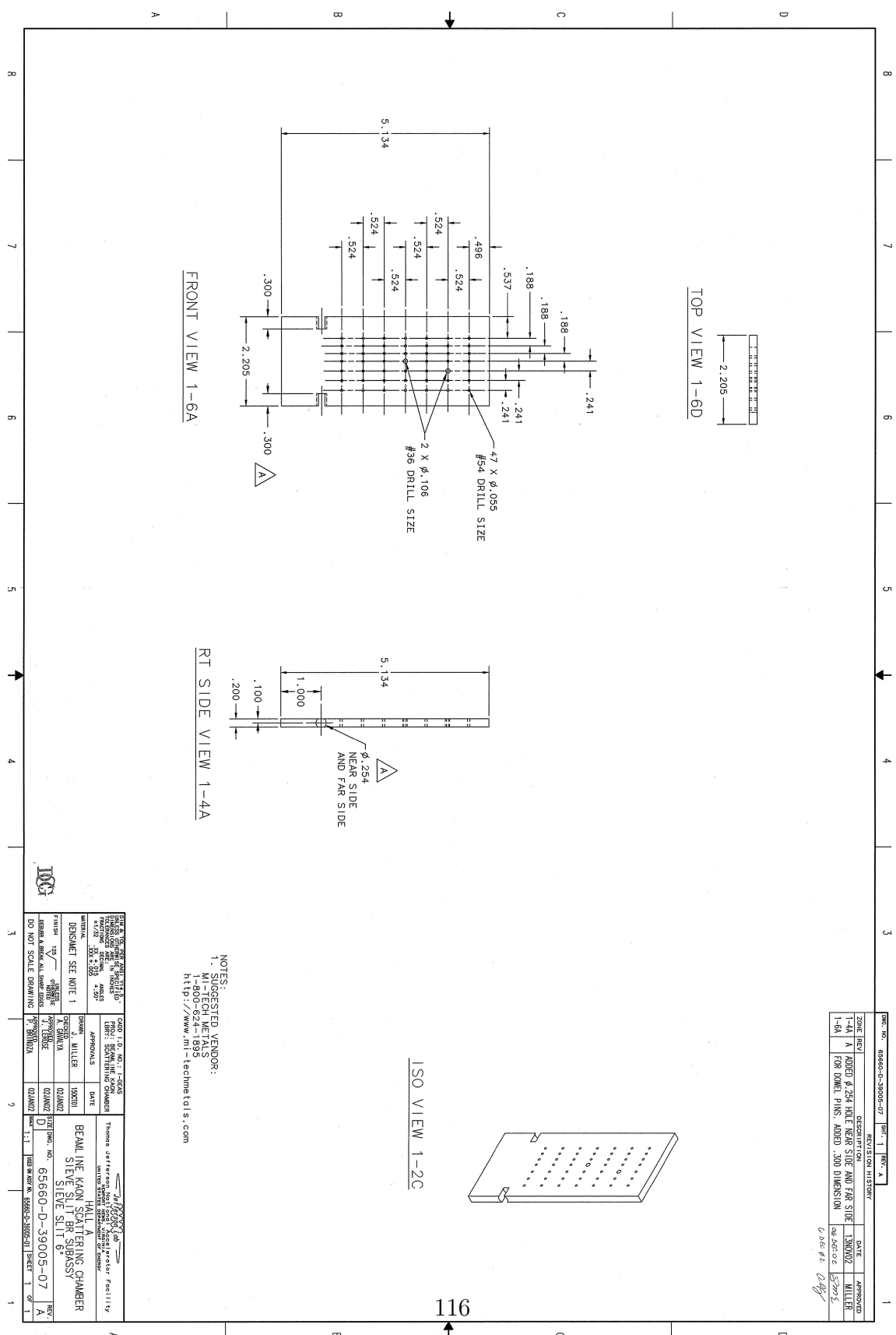
## Experimental Records


### B.1 Sieve Slit

A removable sieve slit was used for optics calibration. The design of the slit are shown in Fig. B.1.

### B.2 Survey Report

The survey reports of target and sieve positions are shown in Fig B.2 and B.3 [79].





## Jefferson Lab Alignment Group

### Data Transmittal

<b>TO:</b> Y. Roblin, T. Michalski, J.P. Chen, M. Poelker, J. LeRose		<b>DATE:</b> 14 Dec 2011	
<b>FROM:</b> J. Dahlberg		<b>Checked:</b>	<b># :</b> A1423

**DETAILS:** Data: Fiducial\halla\g2p\110906, 111130 ; Step2b\halla\g2p\111206, 111214

Below are the results from the recent survey carried out on the Hall A G2p beam line components. X and Y values are relative to ideal beam center. Z values are relative to ideal Hall A pivot (traditional target). A +X is to the beam left from ideal, a +Y is above, and a +Z is downstream. Values are in millimeters and degrees. Detailed information on the G2p super harps is listed below.

LOCATION	Z	X	Y	YAW	PITCH	ROLL
UPST Harp	-23563	+0.11	0.00			
FT1H00 tgt.	-19956	-0.06	0.09	0.016	-0.011	-0.068
Q1H01bpm	-18651	0.22	-0.53			
Q1H01	-18297	0.04	-0.11			
G2p harp1	-8902	0.05	0.12			
FZ1	-7036	-0.11	0.00	0.001	0.001	-0.005
YAG viewer	-5297	-0.14	0.14			
FZ2	-3783	0.04	-0.03	0.023	0.180	-0.009
G2p bpm1	-1817	0.23	-1.34			
G2p harp2	-1689	0.26	-1.53			
G2p bpm2	-1572	0.42	-0.85			
US tgt. pipe	-946	1.60	-1.29			
Tgt. center	-896					
DS tgt. pipe	-801	2.94	-0.86			
Septum	686	0.17	-0.05	-0.029	-0.017	-0.004


**SUPER HARP DATA**

Note: The encoder values are recorded when the wires are centered on the upstream and downstream flanges. The average flange offsets from beam line listed above have to be taken into account separately. Due to backlash in the drive, the readings were always taken when extending the wire into beam from the inside home position. Also, it should be noted that both harps were disassembled with wires replaced after installation in the beam line and therefore, the accuracy of the encoder values is uncertain.

Upstream harp1:    Inside vertical wire = F141  
                          Middle 45 deg wire = D52F  
                          Outside 45 deg wire = 728E

Downstream harp2: Inside horizontal wire = FDCE  
                          Middle 45 deg wire = CC4C  
                          Outside vertical wire = A497

FIGURE B.2: Survey report A1423, which includes positions of the target, septum, and other beamline equipments.



## Jefferson Lab Alignment Group

### Data Transmittal

<b>TO:</b> J.P. Chen, J Zhang, J. LeRose		<b>DATE:</b> 10 May 2012	
<b>FROM:</b> James Dahlberg		<b>Checked:</b>	
<b>DETAILS:</b>		<b># :</b> A1453	

Data: Step2B\HALLA\G2P\120223B, Fiducia\HALLA\G2P\120127A

Below are the results from the G2p sieve slit, collimator, and dump survey carried out on Feb 23<sup>rd</sup>, 2012. Values are relative to the ideal target center with a +X to the beam left, a +Y up, and a +Z downstream. Values are in millimeters and degrees. All coordinates are to the upstream face of the components. The sieve coordinates are to the center hole.

LOCATION	Z	X	Y	YAW	PITCH	ROLL
Dump	639.21	-0.98	4.90	0.103	0.255	0.313
L. Collimator	639.11	66.33	1.50	0.103	0.255	0.073
R. Collimator	639.35	-66.66	-0.04	0.103	0.255	0.180
L. Sieve CL	795.55	80.35	0.31	5.682	0.141	0.257
R. Sieve CL	795.41	-80.39	0.21	-5.647	-0.183	0.305

FIGURE B.3: Survey report A1453, which includes positions of the sieve slits.



# Appendix C

## Summary of non-thesis work

In addition to the project of this thesis on the g2p experiment at Jefferson Lab Hall A, I also worked on the simulation of semi-inclusive deep inelastic scattering at an Electron Ion Collider (EIC) to study the transverse single spin asymmetry.

### C.1 Introduction

Electron-Ion Collider (EIC) is a future facility, where an intense beam of polarized electrons and an intense beam of polarized nucleons or nuclei of element from deuterium to uranium collide. This collider is proposed to understand how the ordinary matter is made up in terms of quarks and gluons, which are the fundamental degrees of freedom of the strong interaction. Active studies have been performed on the EIC by a number of scientists and laboratories around the world. In US, interests have been focused on two designs at Jefferson Lab (JLab) and Brookhaven National Laboratory (BNL). Fig. C.1 demonstrates the schematic of an EIC design at JLab, where the electron beam after the 12-GeV energy upgrade will be used, and the green field of an ion beam complex is under design. Two beams will collide in the eight-figure

to help preserve the beam spins.

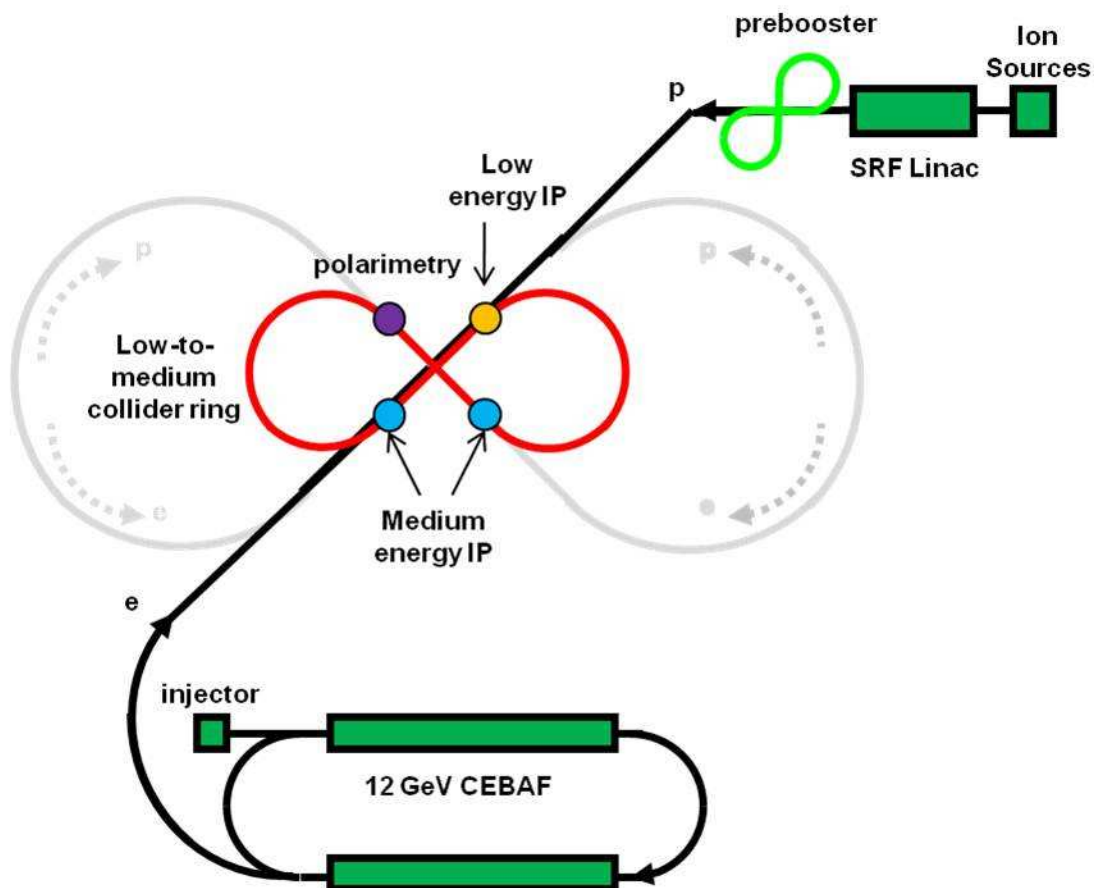


FIGURE C.1: Schematic of the EIC at JLab

This project studies the semi-inclusive deep inelastic scattering at EIC. Deep inelastic scattering (DIS) is a high energy lepton-nucleon (nucleus) scattering, in which the lepton has high enough energy to break into the nucleon, and strikes a quark (gluon) inside the nucleon. The scattered lepton in the final state is detected. Observables in DIS process convey information about the nucleon structure. Thus, DIS is a powerful tool to probe the nucleon structure as illustrated in Fig. C.2. In Fig. C.2, the black circle represents the nucleon structure, and a bunch of hadrons is produced in the scattering. One type of DIS is the semi-inclusive DIS (SIDIS),

which involves detection of the scattered lepton and one of the final-state hadrons<sup>1</sup>. Usually, the hadron which takes most of the momentum from the initial nucleon will be selected, since it tags the information of the struck quark. Thus, SIDIS conveys unique information about nucleon structure.

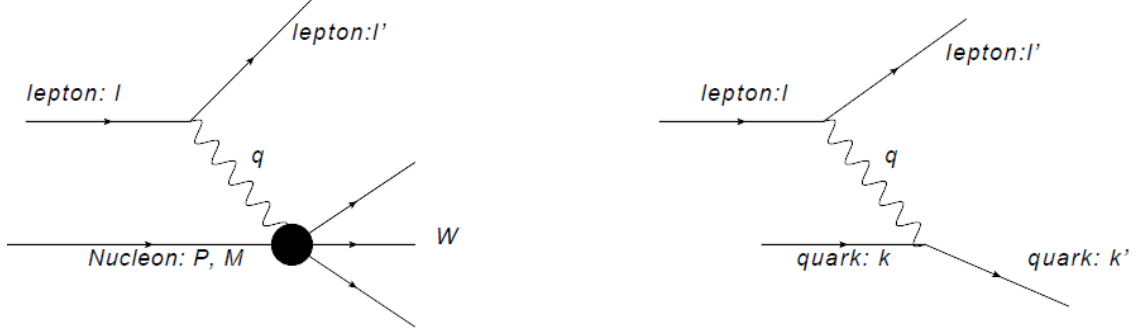


FIGURE C.2: Kinematic variables of the DIS are shown in the left panel.  $l$  and  $l'$  are the 4-momentum of the incoming and outgoing leptons, respectively.  $P$  is the 4-momentum of the nucleon with mass  $M$ , and  $W$  is the invariant mass of the recoiling system  $X$ . The exchange is a virtual photon, whose 4-momentum is  $q = l - l'$ . The right panel shows the fundamental process, where the lepton is interacting with a quark inside the nucleon. The quark's original 4-momentum is  $k = x_{bj} \cdot P$  in the infinite momentum frame.

## C.2 Theoretical Background

The strong interaction, as one of the four fundamental interactions of nature, binds protons and neutrons together to form atomic nuclei and also binds quarks and gluons together to form proton, neutron and other hadrons. Quantum chromodynamics (QCD) with quark and gluon degrees of freedom is believed to be the theory of strong interaction. One unique feature of QCD (strong interaction) is the color confinement, which describes the phenomenon that partons, carrying color charges, are bound into colorless hadrons, and cannot be observed directly. Thus, understanding the nucleon structure provides a powerful tool to understand QCD in the confinement

<sup>1</sup> In comparison to the inclusive DIS which involves only the scattered lepton, and the exclusive DIS which involves all the final-state particles.

region. Additionally, nucleons (protons/neutrons) are the composite particles of nuclear matter, which dominate the mass of most of the visible matter in the universe. Thus, understanding nucleon structure is a central topic by itself in the subatomic physics.

Scientists have been using parton distribution functions (PDF) to quantitatively describe the nucleon structure. PDFs can be interpreted as the probability of finding a parton inside a hadron carrying a fraction of the hadron's momentum. In history, at first PDFs only described the unpolarized and longitudinally polarized situations<sup>2</sup>. Later, scientists found that a very small part of the nucleon's spin is from the intrinsic spins of partons ("spin crisis"). Then, theories were proposed to consider the orbital angular momentum as an important contribution to the nucleon spin. Thus, the transverse dimension became important in the understanding of nucleon structure, which leads to the investigation of the parton's motion transverse to the parent hadron's momentum. This investigation results in the studies and extractions of a new type of parton distribution: the transverse momentum dependent parton distribution (TMD)[99, 100, 101, 102]. There are eight TMDs, three of which, the unpolarized  $f_1$ , the longitudinal polarized parton distribution  $g_{1L}$ , and the quark transversity distribution  $h_{1T}$ , survive upon the integration over the quark's transverse momentum. In the non-relativistic limit, the transversity distribution function  $h_{1T}$  is the same as the longitudinal polarized parton distribution  $g_{1L}$ . Besides these three distributions, the other five TMDs, which vanish over the integration, are the Sivers function ( $f_{1T}^\perp$ ), the Boer-Mulders function ( $h_1^\perp$ ), the pretzelosity function ( $h_{1T}^\perp$ ), and the so-called worm-gear 1 ( $h_{1L}^\perp$ ) and worm-gear 2 functions ( $g_{1T}$ ). They are categorized by the nucleon and quark spin, as illustrated in Fig. C.3. The subscript  $T$  and  $L$  denote the nucleon transverse and longitudinal polarizations, respectively. TMDs depend not only on the longitudinal momentum fraction  $x$ , but also the parton trans-

---

<sup>2</sup> Longitudinal direction is defined by the virtual photon direction in Fig. C.2

verse momentum  $\vec{k}_T$ . Thus, the transversity distribution  $h_1$  can be interpreted as the probability of finding a transversely polarized parton in a transversely polarized nucleon carrying transverse momentum  $\vec{k}_T$  and a fraction  $x$  of the nucleon's longitudinal momentum.

Nucleon Quark			
	Unpol.	Long.	Trans.
Unpol.	$f_1 = \text{[unpolarized nucleon with unpolarized quark]}$		$f_{1T}^\perp = \text{[unpolarized nucleon with transversely polarized quark]}$
Long.		$g_{1L} = \text{[longitudinally polarized nucleon with longitudinally polarized quark]}$	$g_{1T} = \text{[longitudinally polarized nucleon with transversely polarized quark]}$
Trans.	$h_1^\perp = \text{[transversely polarized nucleon with unpolarized quark]}$	$h_{1L}^\perp = \text{[transversely polarized nucleon with longitudinally polarized quark]}$	$h_{1T}^\perp = \text{[transversely polarized nucleon with transversely polarized quark]}$

FIGURE C.3: All eight TMDs at leading twist are categorized by their nucleon and parton spin.

The factorization theorem offers the strategy to access these distribution functions. According to this kind of theory, observables of DIS are expressed in terms of the products of PDFs or TMDs and pQCD elements (hard scattering parts), which means these distribution functions can be extracted from experimental measurements. Especially for TMDs, SIDIS is regarded as a golden process to access all the eight TMDs from experiments with different combinations of unpolarized or polarized initial lepton and nucleon spins, respectively. In this project, the unpolarized electron and transversely polarized nucleon case will be studied to access the Sivers, transversity and pretzelosity functions.

The SIDIS process can be expressed as:

$$\ell(P_e^i) + N(P) \rightarrow \ell'(P_e) + h(P_h) + X, \quad (\text{C.1})$$

where  $\ell$  denotes the initial lepton,  $N$  the initial nucleon, and  $\ell'$  the scattered lepton,  $h$  the produced hadron in the final state, and all the four-momenta are given in parentheses. Under the one-photon exchange approximation, the four-momentum of the virtual photon is expressed as  $q = P_e^i - P_e$  and the four momentum transfer square is  $q^2 = -Q^2$ . The major Lorentz invariant variables are defined as:

$$x = \frac{Q^2}{2P \cdot q}, y = \frac{P \cdot q}{P \cdot P_e^i}, z = \frac{P \cdot P_h}{P \cdot q}, s = (P_e^i + P)^2, \quad (\text{C.2})$$

where  $x$  is the aforementioned longitudinal momentum fraction, and also referred as Bjorken  $x_{bj}$ , and  $s$  is the center-of-mass energy squared of the initial electron-nucleon system. In addition, there are a few frame-dependent kinematic variables,  $\phi_S$ ,  $\phi_h$ , and  $P_T$  (the nucleon spin angle, the azimuthal angle and the transverse momentum of the leading hadron), which are also essential to SIDIS process. They are defined according to the Trento convention as illustrated in Fig. C.4 in the nucleon-at-rest frame.

The differential cross section in a SIDIS ( $e, e'h$ ) process, with unpolarized electron beam and transversely polarized target, can be expressed as the sum of target spin-independent and target spin-dependent terms at leading twist[103]:

$$\begin{aligned} \frac{d\sigma^h}{dx_B dy d\phi_S dz_h d\phi_h dP_T^2} &\equiv d\sigma^h = d\sigma_{UU} + d\sigma_{UT}, \\ &= d\sigma_{UU} + d\sigma_{UT}^{Collins} + d\sigma_{UT}^{Sivers} + d\sigma_{UT}^{Pretzelosity}. \end{aligned} \quad (\text{C.3})$$

The transverse single spin asymmetry (SSA) is defined as:

$$A_{UT} \equiv \frac{1}{|S_T|} \frac{d\sigma_{UT}}{d\sigma_{UU}} \quad (\text{C.4})$$

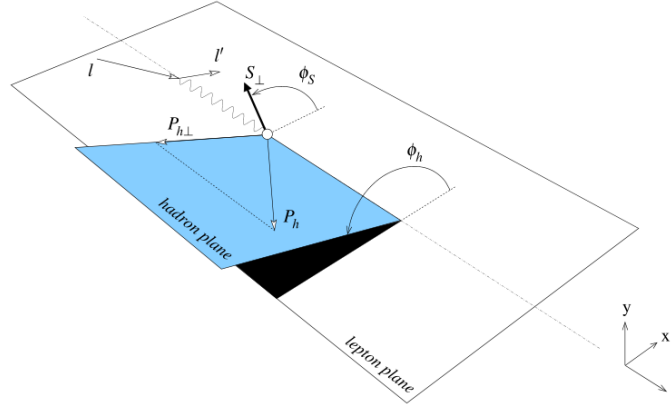


FIGURE C.4: Definitions of azimuthal angles  $\phi_h$  and  $\phi_S$ , and the hadron transverse momentum for SIDIS in the ion-at-rest frame.

where  $U$  and  $T$  represent unpolarized initial leptons and transverse polarized initial hadrons, and  $S_T$  is the polarization. This SSA can be expressed as sum of different azimuthal asymmetries (Collins, Sivers and Pretzelosity) with their angular dependences:

$$\begin{aligned}
A_{UT}(\phi_h, \phi_S) &\equiv \frac{1}{|S_T|} \frac{d\sigma(\phi_h, \phi_S) - d\sigma(\phi_h, \phi_S + \pi)}{d\sigma(\phi_h, \phi_S) + d\sigma(\phi_h, \phi_S + \pi)}, \\
&= A_{UT}^{Collins} \sin(\phi_h + \phi_S) + A_{UT}^{Sivers} \sin(\phi_h - \phi_S) \\
&+ A_{UT}^{pretzelosity} \sin(3\phi_h - \phi_S).
\end{aligned} \tag{C.5}$$

The Collins asymmetry  $A_{UT}^{Collins}$  contains transversity distribution  $h_1$ , while Sivers and pretzelosity asymmetry are associated with the Sivers function and pretzelosity function. Therefore, these three TMDs can be extracted from the measurements of these azimuthal SSAs in SIDIS process.

### C.3 Motivation

A recent experiment using SIDIS is the JLab E06-010 transversity[103], which measured the transverse target SSA from the  $\vec{n}(e, e'\pi^{+,-})X$  reaction with a transversely

polarized  $^3\text{He}$  (effective polarized neutron) target at JLab Hall A and a 6 GeV incident electron beam. The main objective of this 6 GeV transversity experiment is to measure the Collins, Sivers and pretzelosity asymmetries and extract the corresponding functions. I did a small project in the data analysis of this experiment in the summer of my first year to check and calculate the charge and live time from the scalers. This work was led by Dr. Xin Qian (a previous member of Duke MEP group) under the supervision of Prof. Haiyan Gao, and an analysis note was published inside the collaboration.

Furthermore, a new transversity experiment has been approved at Jefferson Lab using 8-GeV and 11-GeV electron beams after the 12-GeV energy upgrade at JLab to extend the study to 4-D manner ( $x$ ,  $Q^2$ ,  $z$ , and  $P_T$ ), which means the distributions will be precisely mapped in four dimensions[104]. I participated in the preparation of this proposal in the first half of my second year. Under the help of Dr. Xin Qian, I studied the kinematic coverage of the solenoid detector for the SIDIS process, statistical uncertainties estimation for separating various leading twist TMD terms using the simulated SIDIS azimuthal angular asymmetries, and projections for the expected two-month running. Ref. [105] about this future experiment has been published recently, in which I am a co-author.

Despite of all these experiments, we are still at the beginning to understand the full picture of the partonic structure of nucleons. A collider with intense and polarized beams will be a natural extension to the next generation study of nucleon structure, and furthermore the QCD. In the 2007 Nuclear Science Advisory Committee (NSAC) Long Range Plan, “An Electron-Ion Collider (EIC) with polarized beams has been embraced by the U.S. nuclear science community as embodying the vision for reaching the next QCD frontier.” In the following sections, the study of the SSA measurements from SIDIS at the EIC will be presented, and the advantages and importance of the EIC will be demonstrated.



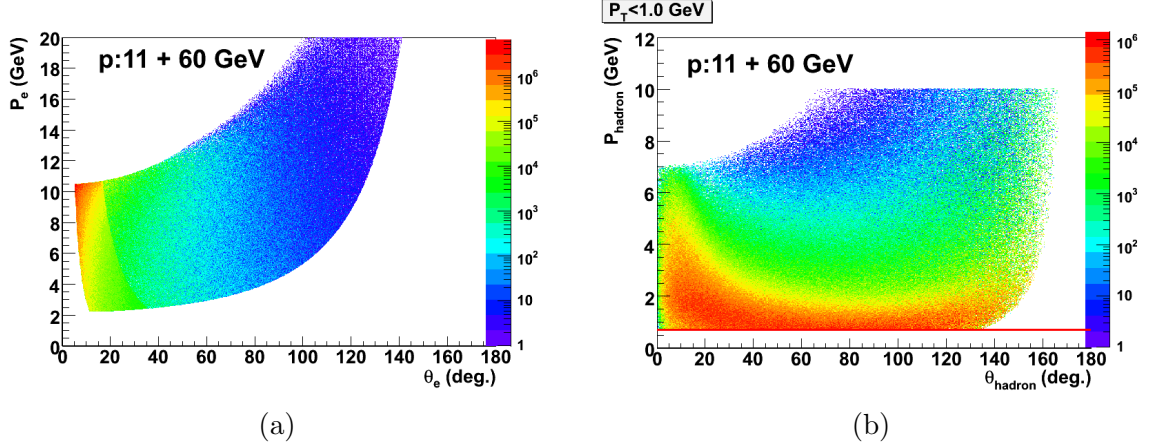


FIGURE C.5: Mometum vs. polar angle in the lab frame for the scattered electrons (a) and detected hadrons (b).

## C.4 SIDIS at EIC

### C.4.1 Phase Space Coverage

In an EIC, a beam of electrons and a beam of ions collide. Following Eqn. C.2, the important relations can be obtained:

$$s = (P_e^i + P)^2 \approx 2P_e^i \cdot P \approx 4E_e^i E_P, Q^2 = x \cdot y \cdot s. \quad (\text{C.6})$$

The latter one demonstrates that at a fixed value of  $s$ ,  $y$  range determines the phase space coverage of  $Q^2$  with  $x$ .

In this section, the SIDIS phase space coverage will be mainly discussed for the 11+60 GeV configuration, which represents a 11 GeV electron beam colliding with a 60 GeV proton beam. In the simulation, the scattered electrons are generated in momentum  $P_e > 0.7$  GeV/c, polar angle  $2.5^\circ < \theta_e < 150^\circ$ <sup>3</sup> and full azimuthal angle. Since we are mainly interested in the DIS region, the following cuts,  $Q^2 > 1$  GeV<sup>2</sup> and  $W > 2.3$  GeV, are applied.  $W$  is the mass of the hadron system recoiling against

<sup>3</sup> Here,  $0^\circ$  represents the momentum direction of the initial electron beam.

the scattered lepton, and this cut is to discard the resonance region. In addition, the  $0.05 < y < 0.8$  cut is also applied considering the limits of the detector resolution and acceptance. With the above cuts, Fig. C.5a shows the distribution of momenta vs. polar angles of the scattered electrons in the lab frame. This distribution reflects the needs in the detector design. First, most of the scattered electron are concentrated in the high-momentum region (closer to the initial electron momentum). Additionally, no electrons are distributed at very forward angles ( $\leq 5^\circ$ ) due to the  $Q^2 > 1 \text{ GeV}^2$  cut. Thus, it is not necessary to detect the very forward angle.

For SIDIS process, more cuts are applied on the hadron side. They are  $0.2 < z < 0.8$  and  $M_X > 1.6 \text{ GeV}$  cut, where  $M_X$  is the missing mass of the  $X$  system in Eq. C.1. The  $z$  range is chosen to ensure the scattering in the SIDIS current fragmentation region. In addition, a low  $P_T$  cut ( $P_T < 1 \text{ GeV}/c$ ) is also applied for the TMD physics, and a  $P_T > 1 \text{ GeV}/c$  cut for the large  $P_T$  physics. Fig. C.5b shows the momenta of detected hadrons vs. polar angles in the lab frame. In this simulation, the hadrons are generated in  $0.7 \text{ GeV}/c < P_h < 10 \text{ GeV}/c$  with full polar and azimuthal angular coverages. The  $P_T < 1 \text{ GeV}/c$  cut is applied. This distribution again reflects the needs in the detector design. First, the hadron events are concentrated in the momentum region of  $0.7\text{-}7 \text{ GeV}/c$ , thus there is no essential need to cover very high momentum region. Additionally, hadrons have a wide distribution of the polar angle in the lab frame, but there is no essential need to cover the very backward angle for the hadron lab polar angle <sup>4</sup>.

Fig. C.6a illustrates the  $Q^2$  vs.  $x$  phase space coverage evolution at different  $s$ . Black region shows the phase space of the aforementioned approved 12-GeV SIDIS experiment at JLab. Overlap exists between this fixed target experiment and the low energy EIC configuration. In addition, a higher-energy configuration would extend the study of SIDIS process to even lower  $x$  and higher  $Q^2$  regions. Moreover,

---

<sup>4</sup> The  $180^\circ$  represents the initial momentum direction of the ion beam.

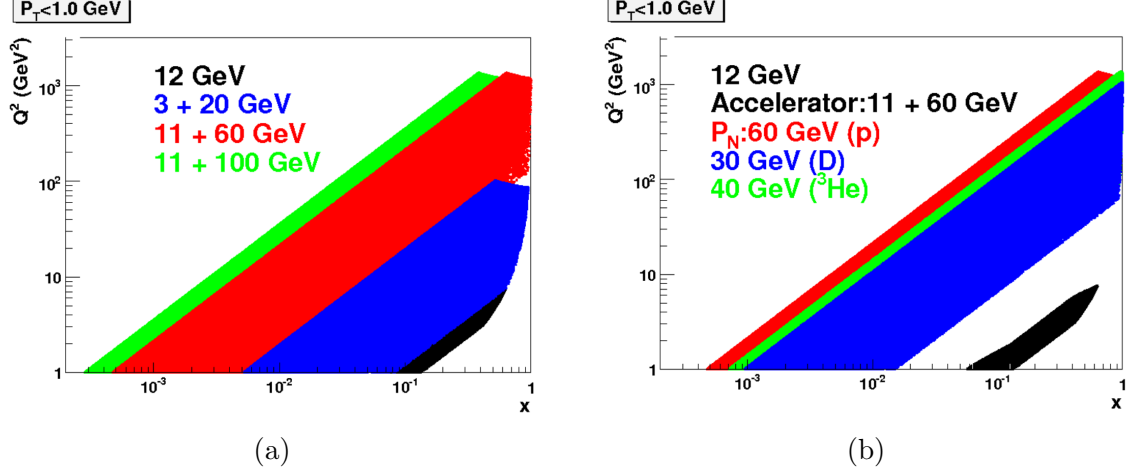


FIGURE C.6: SIDIS phase space of different energy configurations with proton beam (a) and different ion beams, given the fixed accelerator configuration (b).

Fig. C.6b illustrates different mapping of three ion beams (accelerator: 11+60 GeV configuration <sup>5</sup>). Polarized deuteron and <sup>3</sup>He are used as effective neutron targets to achieve the quark flavor separation from the SIDIS data. The mapping shows that the lowest achievable  $x$  and highest achievable  $Q^2$  value for quark flavor separation are limited by the light ion beam.

At high  $P_T$  region ( $P_T > 1$  GeV/c), the requirements on the hadron detection are shown in Fig. C.7. The momenta of the hadron (left) and the lab polar angles of the hadron (right) are plotted vs.  $P_T$ . These distributions show that the hadron momentum range will increase with the increment of  $P_T$ , and the hadron lab angles distribute widely over the entire phase space, but it is not essential to cover the very backward angular range for the hadron lab polar angle.

<sup>5</sup> 60 GeV represents the momentum for proton.

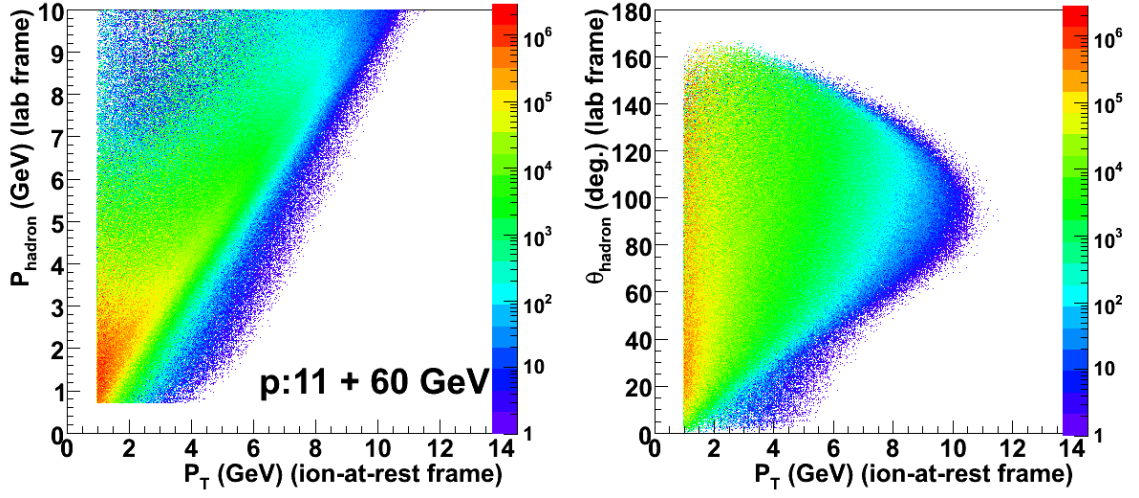


FIGURE C.7: The detected momenta of hadrons vs.  $P_T$  (left) and polar angles vs.  $P_T$  (right) at  $P_T > 1$  GeV/c.

#### C.4.2 Transverse SSA measurements from SIDIS at EIC

##### Monte-Carlo Method

Since most of the transverse SSAs are relatively small, the projected uncertainty of the measured asymmetries can be approximated as:

$$\begin{aligned} \delta A &= \frac{1}{P_e P_I P_N f_D} \cdot \frac{1}{\sqrt{N_{\text{raw}}}} \cdot \sqrt{1 - A^2} \\ &\approx \frac{1}{P_e P_I P_N f_D} \cdot \frac{1}{\sqrt{N_{\text{raw}}}} \end{aligned} \quad (\text{C.7})$$

where  $P_e$ ,  $P_I$  and  $P_N$  are the polarizations of the electron, ion beam, and effective polarization of the nucleon, respectively. The  $f_D$  is the effective dilution factor, and  $N_{\text{raw}}$  is the raw measured counts summing over the two spin states. In order to obtain the projections on the separated Collins, Sivers and pretzelosity asymmetries, the scattered electrons and detected pions/kaons are simulated uniformly in both momentum and coordinate space in the lab frame. Cuts are applied as described in Sec. C.4.1. The SIDIS differential cross section for each accepted event is calculated

Table C.1: Integrated luminosities, and the effective polarization of the proton (neutron for D and  $^3\text{He}$ ) in the projections for different ion beams and EIC energy configurations.

Ion	11+60 GeV	3+20 GeV	11+100 GeV	Polarization
p	$9.3 \times 10^{40} \text{ cm}^{-2}$	$3.1 \times 10^{40} \text{ cm}^{-2}$	$3.1 \times 10^{40} \text{ cm}^{-2}$	1
D	$1.9 \times 10^{41} \text{ cm}^{-2}$	$6.2 \times 10^{40} \text{ cm}^{-2}$	$6.2 \times 10^{40} \text{ cm}^{-2}$	88%
$^3\text{He}$	$1.9 \times 10^{41} \text{ cm}^{-2}$	$6.2 \times 10^{40} \text{ cm}^{-2}$	$6.2 \times 10^{40} \text{ cm}^{-2}$	87.5%

(Ref. [100] for low  $P_T$  and Ref. [106] for high  $P_T$ ). Then combining with the expected luminosity, running time, one can calculate the expected raw number of events in each of the 4-D kinematic bin. The projected uncertainties on the raw asymmetry are obtained after including the polarizations and the effective dilution factor. Additional factors are introduced to mimic the increase of uncertainties due to the azimuthal angular separation of Collins, Sivers, and pretzelosity asymmetries. The detailed discussion of these factors can be found in Appendix II of Ref. [104].

### *Projections*

This section presents the projected results of transverse SSA at the EIC. Table C.1 summarizes the used runtime distribution, luminosities, and effective polarizations for different ion beams and energy configurations. In addition, the polarizations of ion beams is assumed to be 70% and an overall detecting efficiency 50%. The simulated data are binned according to different statistical precision for the transverse SSA measurement in different  $Q^2$  regions.

The full 4-D projections for the entire phase space are shown in Fig. C.8 for  $\pi^+$  Sivers asymmetry with a proton beam. The entire  $z$  coverage from 0.3-0.7 are divided into 8 bins. The projection is limited in the low  $P_T$  region ( $P_T < 1 \text{ GeV}/c$ ), where the  $P_T$  coverage from 0 to 1 GeV/c is divided into 5 bins. In Fig. C.8, the central value of  $z$  bins increases from the left to the right. The central value of  $P_T$  bins increases from the top to the bottom. Each pad shows the projections on  $Q^2$  and  $x$

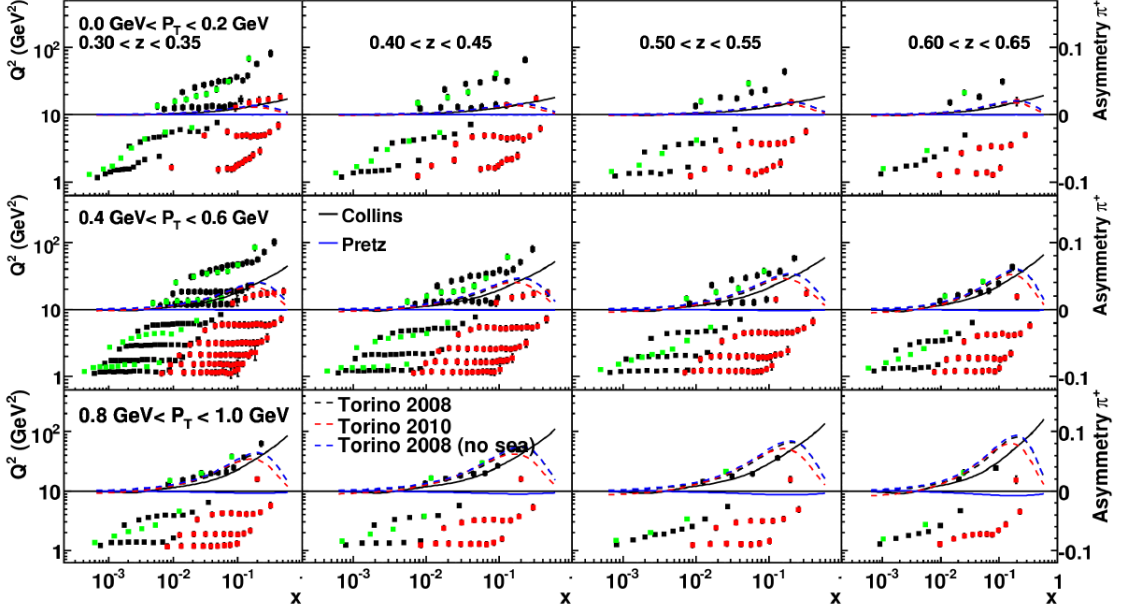


FIGURE C.8: 4-D projections with proton on  $\pi^+$  ( $0.3 < z < 0.7$ ,  $0 \text{ GeV}/c < P_T < 1 \text{ GeV}/c$ ). The black, green, and red dots represent the 11+60 GeV, 11+100 GeV, and 3+20 GeV EIC configuration. The position of the dots are according to the  $Q^2$  axis on the left and the  $x$  axis, while the error bar of each dot is according to the scale of the asymmetry axis on the right. The calculated asymmetries are also according to the asymmetry axis.

dimensions. The position of each point represents the position of the kinematic bin in the  $x$ - $Q^2$  phase space. The error bar of each point follows the right axis of the asymmetry. Together with the projection, several asymmetry calculations are also presented, which also follow the right  $y$ -axis of the plot. Zoomed figure of one  $P_T$  and  $z$  bin can be found in Ref. [107]. In addition to the proton results, the neutron results can be obtained with polarized  $^3\text{He}$  and D beam. Furthermore, with additional kaon particle identification, the kaon SIDIS results can provide additional handle for the flavor separation, since kaon results would also tag the strange quark contribution from the sea. The projected results of  $\pi^+$  on  $^3\text{He}$  and  $K^+$  on proton in full 4-D phase space can be found in Ref. [107].

In addition, the high center-of-mass energy  $s$  at EIC would enable the studies of

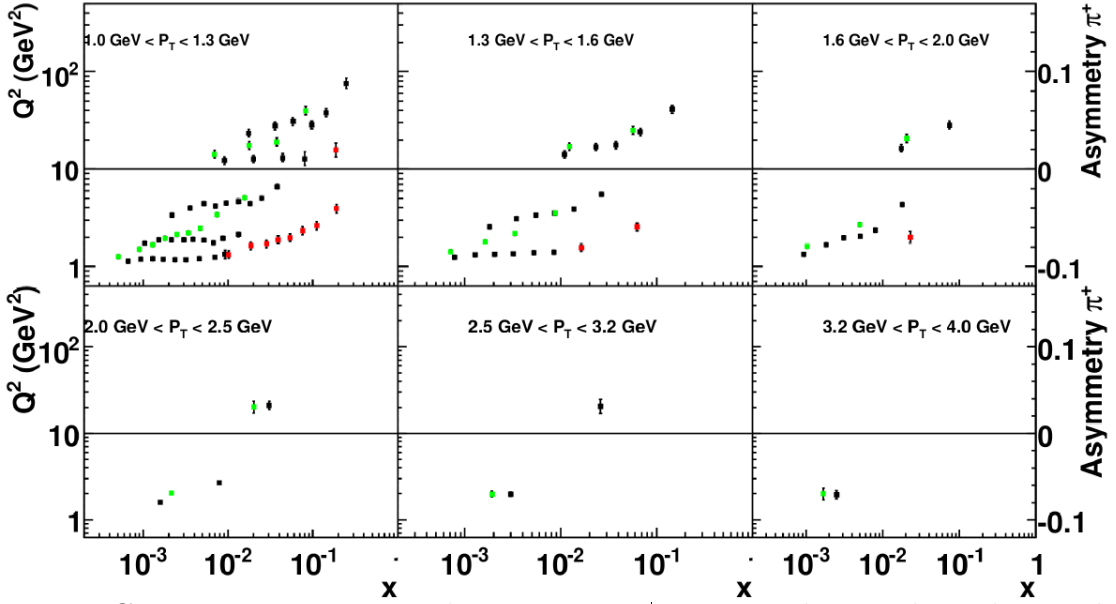


FIGURE C.9: 4-D projection with proton on  $\pi^+$  in one  $z$  bin to show the  $P_T$  dependence ( $0.45 < z < 0.50$ ) in a range of  $1 \text{ GeV}/c < P_T < 10 \text{ GeV}/c$  ( $0 < \lg(P_T) < 1$ ).

transverse SSA in high  $P_T$  region, where the twist-3 contribution is large, and in the intermediate  $P_T$  region, where one expects both the TMD and twist-3 formalism to work. Fig. C.9 shows, as an example, the  $P_T$  dependence of the 4-D projection with proton on  $\pi^+$  in one  $z$  bin. The number of points is limited at high  $P_T$  where the differential cross section decreases.

From these projections, it is clear that the transverse SSA can be precisely mapped in the full  $x$ ,  $Q^2$ ,  $z$  and  $P_T$  4-D phase space with a high luminosity EIC - a complete experiment (Table I) with a luminosity in excess of  $10^{34} \text{ cm}^{-2} \cdot \text{s}^{-1}$  will need 600 days of data taking. In particular, the EIC would facilitate the exploration of high  $Q^2$ , and low  $x$  phase space. Furthermore, the large coverage of  $P_T$  would explore the transverse SSA in the high  $P_T$  region for the first time with SIDIS. The high luminosity is essential to realize the multi-dimensional mapping and extend the TSSA measurements to the extreme conditions (high  $P_T$ , high  $Q^2$  etc.).

## C.5 Conclusion

In this appendix, the simulation studies of the potential to measure TMDs through TSSA of SIDIS with the EIC are presented, and the requirements of the detectors are also discussed. This work shows that an EIC with high energy electron and nuclei beams, high luminosities and polarizations will be an ideal and ultimate machine to probe the three-dimensional structure of nucleons, particularly to advance our understanding of TMDs in the sea quarks and gluons region, as well as the evolution with large phase space coverage.

This study was published in [107] and [108]. Further studies with different configurations and requirements are included in [109] and [110].



# Bibliography

- [1] I. Esterman and O. Stern. “Magnetic Moment of the Deuteron”. *Phys. Rev.* 45 (1934), p. 739.
- [2] Richard P. Feynman. “Very High-Energy Collisions of Hadrons”. *Phys. Rev. Lett.* 23 (24 1969), pp. 1415–1417.
- [3] Jerome I. Friedman and Henry W. Kendall. “Deep inelastic electron scattering”. *Ann. Rev. Nucl. Part. Sci.* 22 (1972), pp. 203–254.
- [4] J. Ashman et al. “An Investigation of the Spin Structure of the Proton in Deep Inelastic Scattering of Polarized Muons on Polarized Protons”. *Nucl. Phys.* B328 (1989), p. 1.
- [5] M. J. Alguard et al. “Deep-Inelastic  $e-p$  Asymmetry Measurements and Comparison with the Bjorken Sum Rule and Models of Proton Spin Structure”. *Phys. Rev. Lett.* 41 (2 1978), pp. 70–73.
- [6] B. W. Filippone and Xiang-Dong Ji. “The Spin structure of the nucleon”. *Adv. Nucl. Phys.* 26 (2001), p. 1. arXiv: [hep-ph/0101224](#) [hep-ph].
- [7] M. N. Rosenbluth. “High Energy Elastic Scattering of Electrons on Protons”. *Phys. Rev.* 79 (4 1950), pp. 615–619.
- [8] Henry W. Kendall. “Deep inelastic scattering: Experiments on the proton and the observation of scaling”. *Rev. Mod. Phys.* 63 (3 1991), pp. 597–614.
- [9] J. D. Bjorken and E. A. Paschos. “Inelastic Electron-Proton and  $\gamma$ -Proton Scattering and the Structure of the Nucleon”. *Phys. Rev.* 185 (5 1969), pp. 1975–1982.
- [10] C. G. Callan and David J. Gross. “High-Energy Electroproduction and the Constitution of the Electric Current”. *Phys. Rev. Lett.* 22 (4 1969), pp. 156–159.
- [11] A. W. Thomas and W. Weise. “The Structure of the Nucleon”. *Wiley-Vch* (2001).
- [12] M. Anselmino, A. Efremov, and E. Leader. “The Theory and phenomenology of polarized deep inelastic scattering”. *Phys.Rept.* 261 (1995), pp. 1–124. arXiv: [hep-ph/9501369](#) [hep-ph].

- [13] Kenneth G. Wilson. “Non-Lagrangian Models of Current Algebra”. *Phys. Rev.* 179 (5 1969), pp. 1499–1512.
- [14] Vronique Bernard. “Chiral perturbation theory and baryon properties”. *Progress in Particle and Nuclear Physics* 60.1 (2008), pp. 82 –160.
- [15] V. Bernard, Norbert Kaiser, and Ulf-G. Meissner. “Chiral dynamics in nucleons and nuclei”. *Int. J. Mod. Phys. E4* (1995), pp. 193–346. arXiv: [hep-ph/9501384](#) [hep-ph].
- [16] Jeffrey Goldstone, Abdus Salam, and Steven Weinberg. “Broken Symmetries”. *Phys. Rev.* 127 (3 1962), pp. 965–970.
- [17] S. Wandzura and Frank Wilczek. “Sum Rules for Spin Dependent Electroproduction: Test of Relativistic Constituent Quarks”. *Phys. Lett.* B72 (1977), p. 195.
- [18] Edward V. Shuryak and A. I. Vainshtein. “Theory of Power Corrections to Deep Inelastic Scattering in Quantum Chromodynamics. 2.  $Q^2$  Effects: Polarized Target”. *Nucl. Phys.* B201 (1982), p. 141.
- [19] Xiangdon Ji. “The nucleon structure functions from deep-inelastic scattering with electroweak currents”. *Nuclear Physics B* 402.12 (1993), pp. 217 –250.
- [20] E. Stein, P. Grnicki, L. Mankiewicz, and A. Schfer. “{QCD} sum rule calculation of twist-4 corrections to Bjorken and Ellis-Jaffe sum rules”. *Physics Letters B* 353.1 (1995), pp. 107 –113.
- [21] D. Drechsel, B. Pasquini, and M. Vanderhaeghen. “Dispersion relations in real and virtual Compton scattering”. *Physics Reports* 378.23 (2003), pp. 99 –205.
- [22] D. Drechsel, S. S. Kamalov, and L. Tiator. “Gerasimov-Drell-Hearn sum rule and related integrals”. *Phys. Rev. D* 63 (11 2001), p. 114010.
- [23] L. N. Hand. “Experimental Investigation of Pion Electroproduction”. *Phys. Rev.* 129 (4 1963), pp. 1834–1846.
- [24] V. Sulkosky. *Ph. D. Thesis, The College of William and Mary* (2007).
- [25] Jian-Ping. Chen, A. Deur, and Zein-Eddine Meziani. “Sum rules and moments of the nucleon spin structure functions”. *Mod.Phys.Lett.* A20 (2005), pp. 2745–2766. arXiv: [nucl-ex/0509007](#) [nucl-ex].
- [26] Hugh Burkhardt and W.N Cottingham. “Sum rules for forward virtual compton scattering”. *Annals of Physics* 56.2 (1970), pp. 453 –463.
- [27] P. L. Anthony et al. “Deep inelastic scattering of polarized electrons by polarized  $^3\text{He}$  and the study of the neutron spin structure”. *Phys. Rev. D* 54 (11 1996), pp. 6620–6650.
- [28] D. Adams et al. “Measurement of the spin-dependent structure function  $g_1(x)$  of the proton”. *Physics Letters B* 329.23 (1994), pp. 399 –406.

- [29] D. Adams et al. “Spin structure of the proton from polarized inclusive deep-inelastic muon-proton scattering”. *Phys. Rev. D* 56 (9 1997), pp. 5330–5358.
- [30] D. Adams et al. “Spin asymmetry in muon-proton deep inelastic scattering on a transversely-polarized target”. *Physics Letters B* 336.1 (1994), pp. 125–130.
- [31] D. Adams et al. “The spin-dependent structure function  $g_1(x)$  of the deuteron from polarized deep-inelastic muon scattering”. *Physics Letters B* 396.14 (1997), pp. 338–348.
- [32] Peter Bosted. “Very preliminary results for the spin structure function  $g_2$  from {SLAC} {E155x}”. *Nuclear Physics A* 663664.0 (2000), pp. 297c–300c.
- [33] P.M. King. “Spin Structure Functions of the Proton and Deuteron from SLAC Experiments E155 and E155X”. *SLAC-PUB-9741* (2002).
- [34] K. Abe et al. “Measurements of the proton and deuteron spin structure functions  $g_1$  and  $g_2$ ”. *Phys. Rev. D* 58 (11 1998), p. 112003.
- [35] P. L. Anthony. “Precision measurement of the proton and deuteron spin structure functions  $g_2$  and asymmetries  $A_2$ ”. *Physics Letters B* 553.1-2 (2003), pp. 18–24.
- [36] M. Stratmann. “Bag model predictions for polarized structure functions and their  $Q^2$ -evolutions”. English. *Zeitschrift fr Physik C Particles and Fields* 60.4 (1993), pp. 763–771.
- [37] X. Song. “Polarized structure function  $g_2$  in the c.m. bag model”. *Phys. Rev. D* 54 (3 1996), pp. 1955–1966.
- [38] Herbert Weigel and Leonard Gamberg. “Hadron structure functions within a chiral quark model”. *Nuclear Physics A* 680.14 (2001). Quark Nuclear Physics 2000, pp. 48–51.
- [39] M. Wakamatsu. “Polarized structure function  $g_2(x)$  in the chiral quark soliton model”. *Physics Letters B* 487.12 (2000), pp. 118–124.
- [40] K. Kramer et al. “ $Q^2$  Dependence of the Neutron Spin Structure Function  $g_2^n$  at Low  $Q^2$ ”. *Phys. Rev. Lett.* 95 (14 2005), p. 142002.
- [41] K. Abe et al. “Measurement of the Proton and Deuteron Spin Structure Function  $g_1$  in the Resonance Region”. *Phys. Rev. Lett.* 78 (5 1997), pp. 815–819.
- [42] M. Amarian et al. “ $Q^2$  Evolution of the Generalized Gerasimov-Drell-Hearn Integral for the Neutron using a  $^3\text{He}$  Target”. *Phys. Rev. Lett.* 89 (24 2002), p. 242301.
- [43] F. Wesselmann et al. “Proton Spin Structure in the Resonance Region”. *Phys. Rev. Lett.* 98 (13 2007), p. 132003.
- [44] M. Amarian et al. “ $Q^2$  Evolution of the Neutron Spin Structure Moments using a  $^3\text{He}$  Target”. *Phys. Rev. Lett.* 92 (2 2004), p. 022301.

- [45] X. Zheng et al. “Precision measurement of the neutron spin asymmetries and spin-dependent structure functions in the valence quark region”. *Phys. Rev. C* 70 (6 2004), p. 065207.
- [46] J.P.Chen, A.Deur, F.Garibaldi, spokesperson. “JLab E97-110 experiment”. *Proposal, Jefferson Lab* (1997).
- [47] P. Solvignon et al. “Quark-Hadron Duality in Neutron ( $^3\text{He}$ ) Spin Structure”. *Phys. Rev. Lett.* 101 (18 2008), p. 182502.
- [48] J.P. Chen. “Moments of Spin Structure Functions: Sum Rules and Polarizabilities”. *Int.J.Mod.Phys.* E19 (2010), pp. 1893–1921. arXiv: 1001.3898 [nucl-ex].
- [49] M. Amarian et al. “Measurement of the Generalized Forward Spin Polarizabilities of the Neutron”. *Phys. Rev. Lett.* 93 (15 2004), p. 152301.
- [50] H. Dutz et al. “First Measurement of the Gerasimov-Drell-Hearn Sum Rule for  $^1\text{H}$  from 0.7 to 1.8 GeV at ELSA”. *Phys. Rev. Lett.* 91 (19 2003), p. 192001.
- [51] Y. Prok et al. “Moments of the spin structure functions and for  $0.05 < Q^2 < 3.0\text{GeV}^2$ ”. *Physics Letters B* 672.1 (2009), pp. 12–16.
- [52] Vadim Lensky, Jose Manuel Alarcón, and Vladimir Pascalutsa. “Moments of nucleon structure functions at next-to-leading order in baryon chiral perturbation theory”. *Phys. Rev. C* 90 (5 2014), p. 055202.
- [53] Véronique Bernard, Evgeny Epelbaum, Hermann Krebs, and Ulf-G. Meißner. “New insights into the spin structure of the nucleon”. *Phys. Rev. D* 87 (5 2013), p. 054032.
- [54] Chung Kao, Thomas Spitzenberg, and Marc Vanderhaeghen. “Burkhardt-Cottingham sum rule and forward spin polarizabilities in heavy baryon chiral perturbation theory”. *Phys. Rev. D* 67 (1 2003), p. 016001.
- [55] Véronique Bernard, Thomas R. Hemmert, and Ulf-G. Meißner. “Spin structure of the nucleon at low energies”. *Phys. Rev. D* 67 (7 2003), p. 076008.
- [56] J. Ahrens et al. “First Measurement of the Gerasimov-Drell-Hearn Integral for  $^1\text{H}$  from 200 to 800 MeV”. *Phys. Rev. Lett.* 87 (2 2001), p. 022003.
- [57] Veronique Bernard, Thomas R. Hemmert, and Ulf-G. Meissner. “Spin structure of the nucleon at low-energies”. *Phys.Rev.* D67 (2003), p. 076008. arXiv: hep-ph/0212033 [hep-ph].
- [58] Chung Wen Kao, Thomas Spitzenberg, and Marc Vanderhaeghen. “Burkhardt-Cottingham sum rule and forward spin polarizabilities in heavy baryon chiral perturbation theory”. *Phys.Rev.* D67 (2003), p. 016001. arXiv: hep-ph/0209241 [hep-ph].
- [59] M. Amarian et al. “Measurement of the generalized forward spin polarizabilities of the neutron”. *Phys.Rev.Lett.* 93 (2004), p. 152301. arXiv: nucl-ex/0406005 [nucl-ex].

- [60] Nikolai Kochelev and Yongseok Oh. “Axial anomaly and the  $\delta_{LT}$  puzzle”. *Phys.Rev.* D85 (2012), p. 016012. arXiv: 1103.4892 [hep-ph].
- [61] Hugh Burkhardt and W.N. Cottingham. “Sum rules for forward virtual Compton scattering”. *Annals Phys.* 56 (1970), pp. 453–463.
- [62] X. Zheng. *Ph. D. Thesis, MIT* (2002).
- [63] Pengjia Zhu et al. “Beam Position Reconstruction for the g2p Experiment in Hall A at Jefferson Lab”. *Nucl. Instrum. Meth.* A808 (2016), pp. 1–10. arXiv: 1509.03510 [physics.ins-det].
- [64] P. Zhu. “Beam charge measurement for  $g_2^p$  experiment”. *g2p Technical Notes* (2015).
- [65] C. Gu. “Helicity decoder for E08-027”. *g2p Technical Notes* (2014).
- [66] J. Alcorn et al. “Basic Instrumentation for Hall A at Jefferson Lab”. *Nucl.Instrum.Meth.* A522 (2004), pp. 294–346.
- [67] “Miller Measurements for E08-027 (g2p) and E08-007” (2012).
- [68] J. Maxwell. “Solid polarized target primer for  $g_2^p$  target operators” (2012).
- [69] T. Badman. “Proton polarization studies and uncertainty analysis for E08-027”. *g2p Technical Notes* (2013).
- [70] K. Slifer. *Ph. D. Thesis, Temple University* (2004).
- [71] Y. Qiang. *Ph. D. Thesis, MIT* (2007).
- [72] C. Grupen and B. Shwartz. *Particle Detectors*. Cambridge University Press, 1996.
- [73] “Experimental Physics and Industrial Control System”. <http://aps.anl.gov/epics/> ().
- [74] N. Liyanage. “Optics Calibration of the Hall A High Resolution Spectrometers using the C Optimizer”. *Hall A Technical Notes* (2002).
- [75] J. Liu. “VDC multi-track efficiency study for E08-027”. *g2p Technical Notes* (2013).
- [76] R. Zielinski. “Determining the trigger efficiency for E08-027: update”. *g2p Technical Notes* (2014).
- [77] M. Cummings. “Efficiency studies and PID cut optimization for E08-027”. *g2p Technical Notes* (2013).
- [78] P. Zhu. *Ph. D. Thesis, University of Science and Technology of China* (2015).
- [79] “Survey reports for E08-027: A1423, A1435, A1453, A1463”. <https://www.jlab.org/accel/survey/> ().
- [80] P. E. Bosted, R. Fersch, G. Adams, et al. “Ratios of  $^{15}\text{N}/^{12}\text{C}$  and  $^4\text{He}/^{12}\text{C}$  inclusive electroproduction cross sections in the nucleon resonance region”. *Phys. Rev. C* 78 (1 2008), p. 015202.

- [81] R. Zielinski. “Unpolarized radiative corrections”. *g2p Technical Note* (2014).
- [82] T. Badman. “Dilution analysis for E08-027”. *Technote* (2015).
- [83] M. Cummings. “Packing fraction analysis for E08-027”. *Technote* (2015).
- [84] Siddharth Venkat, John Arrington, Gerald A. Miller, and Xiaohui Zhan. “Realistic transverse images of the proton charge and magnetization densities”. *Phys. Rev. C* 83 (1 2011), p. 015203.
- [85] D. Drechsel, S. S. Kamalov, and L. Tiator. “Unitary Isobar Model - MAID2007”. *Eur. Phys. J. A* 34 (2007), pp. 69–97. arXiv: 0710.0306 [nucl-th].
- [86] M. E. Christy and Peter E. Bosted. “Empirical fit to precision inclusive electron-proton cross- sections in the resonance region”. *Phys. Rev. C* 81 (2010), p. 055213. arXiv: 0712.3731 [hep-ph].
- [87] Y. Liang et al. “Measurement of  $R = \sigma(L) / \sigma(T)$  and the separated longitudinal and transverse structure functions in the nucleon resonance region” (2004). arXiv: nucl-ex/0410027 [nucl-ex].
- [88] S. P. Malace et al. “Applications of quark-hadron duality in  $F(2)$  structure function”. *Phys. Rev. C* 80 (2009), p. 035207. arXiv: 0905.2374 [nucl-ex].
- [89] M. I. Niculescu C. Keppel. *Preliminary results from JLab E00-002* (2010).
- [90] L. W. Whitlow. *Ph. D. Thesis, The American University* (1990).
- [91] M. MacCormick et al. “Total photoabsorption cross sections for  $^1\text{H}$ ,  $^2\text{H}$ , and  $^3\text{He}$  from 200 to 800 MeV”. *Phys. Rev. C* 53 (1 1996), pp. 41–49.
- [92] P.E. Bosted and V. Mamyan. “Empirical Fit to electron-nucleus scattering” (2012). arXiv: 1203.2262 [nucl-th].
- [93] L. W. MO and Y. S. TSAI. “Radiative Corrections to Elastic and Inelastic ep and up Scattering”. *Rev. Mod. Phys.* 41 (1 1969), pp. 205–235.
- [94] Karl Slifer. “Modifications to the QFS and RADCOR codes”. *Technote, Jefferson Lab* (2003).
- [95] etc S. Stein. “Electron scattering at 4’ with energies of 4.5-20 Gev”. *Physical Review D, V12, No.7* (1975).
- [96] I. Akushevich, A. Ilyichev, and N. Shumeiko. “Radiative effects in scattering of polarized leptons by polarized nucleons and light nuclei”. *Lepton and photon interactions at high energies. Proceedings, 20th International Symposium, LP 2001, Rome, Italy, July 23-28, 2001*. 2001. arXiv: hep-ph/0106180 [hep-ph].
- [97] I. Akushevich et al. “POLARD 2.0 FORTRAN code for the radiative corrections calculation to deep inelastic scattering of polarized particles”. *Comput. Phys. Commun.* 104 (1997), pp. 201–244. arXiv: hep-ph/9706516 [hep-ph].
- [98] Karl Slifer. “Spin Structure of  $^3\text{He}$  and the Neutron at Low  $Q^2$ ; A Measurement of the Extended GDH Integral and the Burkhardt-Cottingham Sum Rule”. PhD thesis. Temple University, 2004.

- [99] P. J. Mulders and R. D. Tangerman. “The complete tree-level result up to order  $1/Q$  for polarized deep-inelastic leptonproduction”. *Nucl. Phys.* B461 (1996), pp. 197–237. eprint: [hep-ph/9510301](#).
- [100] Alessandro Bacchetta et al. “Semi-inclusive deep inelastic scattering at small transverse momentum”. *JHEP* 02 (2007), p. 093. arXiv: [hep-ph/0611265](#).
- [101] Xiang-dong Ji. “Viewing the proton through ‘color’-filters”. *Phys. Rev. Lett.* 91 (2003), p. 062001. arXiv: [hep-ph/0304037](#).
- [102] Andrei V. Belitsky, Xiang-dong Ji, and Feng Yuan. “Quark imaging in the proton via quantum phase-space distributions”. *Phys. Rev.* D69 (2004), p. 074014. arXiv: [hep-ph/0307383](#).
- [103] X. Qian. *thesis, Duke University (unpublished)* (2010).
- [104] J.P. Chen et al. “JLab Experiment E12-10-006”. *Jefferson Lab Proposal* (2010).
- [105] H. Gao et al. “Transverse Spin Structure of the Nucleon through Target Single Spin Asymmetry in Semi-Inclusive Deep-Inelastic ( $e, e'\pi^\pm$ ) Reaction at Jefferson Lab”. *Eur. Phys. J. Plus* 126 (2011), p. 2. arXiv: [1009.3803 \[hep-ph\]](#).
- [106] M. Anselmino, M. Boglione, A. Prokudin, and C. Turk. “Semi-inclusive deep inelastic scattering processes from small to large  $P(T)$ ”. *Eur. Phys. J.* A31 (2007), pp. 373–381. arXiv: [hep-ph/0606286](#).
- [107] M. Anselmino et al. “Transverse Momentum Dependent Parton Distribution/Fragmentation Functions at an Electron-Ion Collider”. *Eur. Phys. J.* A47 (2011), p. 35. arXiv: [1101.4199 \[hep-ex\]](#).
- [108] Haiyan Gao, Jian-Ping Chen, Min Huang, and Xin Qian. “Future (transverse) spin physics at Jefferson Lab”. *J. Phys. Conf. Ser.* 295 (2011), p. 012019.
- [109] Daniel Boer et al. “Gluons and the quark sea at high energies: Distributions, polarization, tomography” (2011). arXiv: [1108.1713 \[nucl-th\]](#).
- [110] A. Accardi et al. “Electron Ion Collider: The Next QCD Frontier - Understanding the glue that binds us all” (2012). Ed. by A. Deshpande, Z. E. Meziani, and J. W. Qiu. arXiv: [1212.1701 \[nucl-ex\]](#).

# Biography

Min Huang was born in Chuzhou, Anhui province, China on May 12th, 1989. She attended University of Science and Technology of China in 2004, and graduated in 2008 with a B.S. in Physics. In the fall of the same year, she began the graduate studies at Duke University. In the summer of 2009, she started working with Professor Haiyan Gao. She has made essential contributions to four papers and published several other papers as a collaborator.

## Awards and Fellowships

- 2011-2012, 2012-2013 JSA/JLab Graduate Fellowship Program
- 2007 Outstanding Undergraduate Research Project Award
- 2004-2007 Outstanding Student Scholarship